UNIVERSITY OF LIVERPOOL

An improved impermeable solid boundary scheme for the MLPG_R method and a two-phase ISPH model for suspended sediment-laden flows

Thesis submitted in accordance with the requirements of the

University of Liverpool for the degree of

Doctor in Philosophy by

Xinglin Pan

May 2022

Abstract

Over the past decades, meshless methods have become an essential numerical tool for simulating a wide range of science and engineering problems. The key idea of the meshless methods is to provide accurate and stable numerical solutions, where the computation domain is discretized using particles instead of using conventional meshes. In this thesis, developments on the Meshless Local Petrov-Galerkin (MLPG) method and incompressible smoothed particle hydrodynamics (ISPH) have been carried out for rigid boundary condition implementation and simulation of dispersed two-phase flows, respectively.

For rigid boundary condition implementation in the MLPG method, an improved boundary scheme is developed through a weak formulation for the boundary particles based on Pressure Poisson Equation (PPE). In this scheme, the wall boundary particles simultaneously satisfy the PPE in the local integration domain by adopting the MLPG method with the Rankine source solution (MLPG_R) integration scheme (Ma, 2005b) and the pressure Neumann boundary condition. The new weak formulation vanishes the derivatives of the unknown pressure at wall particles and is discretized in the truncated support domain without extra artificial treatment. This improved boundary scheme is validated by analytical solutions, numerical benchmarks, and experimental data in the cases of patch tests, lid-driven cavity, flow over a cylinder and monochromic wave generation. The numerical results show higher accuracy in pressure and velocity, especially near the boundary, compared to the existing boundary treatment methods that directly discretize the pressure Neumann boundary condition.

For two-phase meshless model development, the incompressible SPH method is developed for simulating suspended sediment transport problems. The fluid and sediment are treated as two continuous phases described by two sets of Navier-Stokes equations with interactions between two phases achieved by the drag force. The computational domain is discretized into a single set of SPH particles which move with the fluid velocity but carry the local properties of both phases, including sediment velocity and its volume fraction. In addition, large eddy simulation (LES) is employed for representing the turbulent effect, in which the eddy viscosities are defined by the Smagorinsky model. The pressure Neumann boundary condition is imposed on the rigid solid walls and the zero pressure boundary condition on the free water surface. The two-phase model is verified by the analytical solutions for two idealized problems of still water with neutrally buoyant sediment and still water with naturally settling sediment in a two-dimensional water tank. The model is then applied to the study of sand dumping. It is shown that the characteristics of the settling sand cloud, the pressure field, and the flow vortices are in good agreement with experimental results. The proposed two-phase model is proven to be effective for the numerical study of suspended sediment problems.

Acknowledgements

I want to thank my primary supervisor, Dr Yan Zhou, for the help, guidance, and encouragement during my four years of PhD study. I am also very grateful for the advice given to me by Prof. Ping Dong and Dr Huabin Shi.

I would finally like to thank my mother, Zhang, Zhi and my father, Pan, Yongfu, for their selfless love and support.

Contents

List of figures

Chapter 1: Introduction

1.1 Background

In order to meet the requirements of simulating complicated physical phenomena in nature and industrial processes, computer-based numerical modelling methods have been widely used in various fields of research areas and engineering applications. In the field of fluid dynamics and hydrodynamics, computational fluid dynamics (CFD) creates a digital simulation that uses computer-based numerical algorithms and analysis to solve fluid flow problems. Benefiting from the sustained development of computing power, these numerical methods can simulate an extensive range of applications from free-surface flows to complex multiphase sediment transport problems and have had remarkable successes (Vacondio et al., 2021).

The numerical methods can roughly be grouped into mesh-based methods and meshless methods. The traditional mesh-based methods include the Finite Volume Method (FVM, Hirt & Nichols, 1981), the Finite Element Method (FEM, Neuman & Witherspoon, 1970) and the Finite Difference Method (FDM, Harlow & Welch, 1965). Over the past decades, these mesh-based methods have been developed as practical tools and employed in most well-established commercial CFD packages.

The meshless methods were proposed with the objective of bypassing the use of conventional meshes and eliminating difficulties associated with

mesh generation or distortion where boundaries deform. By using a set of discrete particles to represent the whole continuous system, several novel meshless methods have been developed in recent decades, including the smoothed particle hydrodynamics (SPH, Lucy, 1977; Gingold & Monaghan, 1977), the element free Galerkin method (EFG, Belytschko et al. 1994), the reproducing kernel particle method (RKPM, Liu et al., 1995), the meshless local Petrov-Galerkin method (MLPG, Atluri & Zhu, 1998), etc. Sriram & Ma (2021) summarized some significant advantages of meshless methods like better performance in handling problems with large deformation (e.g., breaking free water surface), moving discontinuities (e.g., wave propagation), etc. Despite the massive progress in developing meshless methods since the middle of the 20th century, some subsections still need to be further explored, including the solid boundary implementation and multiphase flow simulation addressed in this thesis.

According to Wang et al. (2016), solid boundary implementation plays a significant role in flow-structure interaction but remains less developed. With this respect, solid boundary implementation can significantly affect the computational accuracy and cost. The solid boundary condition in MLPG was initially implemented by the weak formulation of flow governing equations over the incomplete sub-domains of the boundary particles in Atluri & Zhu (1998). Ma (2005a) further developed the solid boundary scheme by direct discretization of the pressure Neumann boundary condition. It has been proven to be effective in preventing inner fluid particles from penetrating the solid walls. However, such an approach does not have a consistent weak formulation throughout the simulation domain. Additionally, the errors introduced at the boundary can creep into the inner

flow domain as the calculation of the first-order term (i.e., the gradient operator of pressure) is involved.

Suspended sediment transport by flows with a free surface is a classic but not yet fully understood subject of the river, coastal and estuary engineering. Over the past few decades, many two-phase models have been proposed to study the mechanics of sediment motions (Finn et al., 2016; Fonty et al., 2019). Specifically, the most existing two-phase models are based on the mesh-based Eulerian scheme (Dong & Zhang, 2002; Chang & Hsieh, 2003; Jha & Bombardelli, 2009; Chen et al., 2011; Shi & Yu, 2015; Lee & Huang, 2018), which suffers specific drawbacks in tracking the complicated free surface deformation. As the meshless methods have been rapidly popularized in recent years, some attempts have been made through the SPH formulations to solve two-phase fluid flow problems, with some questionable assumptions (Ran et al., 2015; Pahar & Dhar, 2017, Shi et al., 2017; Shi et al., 2019). So far, a general formulation following the incompressible SPH scheme has not been established. Besides, an improved understanding of intergranular stresses and interphase forces with a two-phase model is still required (Shi et al., 2019).

In this work, two numerical developments associated with meshless methods of MLPG_R and ISPH are achieved, including a new scheme for solid boundary conditions implementation for the MLPG_R method and a multiphase ISPH model for simulating suspended sediment motion problems.

1.2 Aims and objectives

The main aim of this thesis is developing the existing meshless methods of MLPG and ISPH to improve boundary condition implementation and achieve two-phase sediment transport simulation, respectively. Four main objectives are identified as below:

1. Develop an improved impermeable solid boundary scheme for the MLPG method based on Rankine source solution (MLPG_R), which can achieve higher accuracy through a weak formulation for the boundary particles based on Pressure Poisson Equation (PPE).

2. Implement the code of the newly developed boundary scheme, and further validate the boundary scheme by analytical solutions, numerical benchmarks, and experimental data.

3. Develop a two-phase ISPH model for simulating suspended sediment motion, in which the fluid and sediment are treated as two continuous phases and described by two sets of governing equations. Besides, this model aims to provide a general ISPH formulation in the two-phase framework.

4. Implement the code of the two-phase ISPH model and further validate the model by idealized problems and the application of sand dumping case.

1.3 Structure of the thesis

The structure of the thesis is organised as follows:

Chapter 2 presents the literature review relative to the current study, including a brief history of CFD and meshless methods, existing boundary treatment methods used in meshless methods, and existing numerical methods in modelling multiphase flows.

Chapter 3 shows the methodology of meshless methods. This chapter starts with the derivation of the governing equations in the Lagrangian frame; a numerical procedure for solving pressure is presented; finally, formulations of the MLPG_R method and general SPH method are provided.

Chapter 4 presents an improved solid boundary scheme based on the MLPG_R method. The new formulation has been validated by the analytical solution of the patch test and numerical benchmarks.

Chapter 5 introduces a newly developed two-phase model based on the SPH method. Validation for idealized cases and application of the proposed model to the sand dumping problem are discussed.

Chapter 6 summarises the numerical results and concluding remarks on the overall research outcomes. Additionally, potential recommendations for future research are also highlighted.

In addition, **Appendices A** & **B** aim to provide the mathematical derivation process of the improved boundary scheme for wall particles and the governing equations of the two-phase ISPH model, respectively.

Chapter 2: Literature review

2.1 Computation Fluid Dynamics

Computational fluid dynamics (CFD) is a branch of fluid mechanics that uses computer-based numerical algorithms and analysis to solve fluid flow problems. It can be described as the mathematical modelling process that can numerically simulate fluid flows using high-speed computers. For example, the Navier-Stokes equations are specified as the mathematical model that can describe the changes in physical properties for fluid flows. Anderson & Wendt (1995) indicated that the basic principles that can determine the motion of any fluid flows are the mass, momentum, and energy conservation laws expressed in partial differential equations. In other words, CFD is the computational tool for replacing the mathematical governing equations with numerical descriptions.

An early example of the application of computational fluid dynamics can be tracked in the work of Kopal (1947), which compiled massive tables of the supersonic flow over different geometries by solving the governing partial differential equations. With the development of high-performance computers, some pioneering applications appeared during the last century of the 60s and 70s, including the boundary layer flow simulation by Fay & Riddell (1958) and Blottner (1964), inviscid flow modelling by Hall et al. (1962), to name but a few. Since then, the CFD has become a powerful tool for a wide range of engineering applications, bridging the gap between classic experimental studies and analytical theories. Moreover, computer power is utilized to solve relatively complicated problems involving high-

velocity, high-temperature, turbulent fluid flows etc. The modern CFD technology was initially applied in wind tunnel studies as the experimental expense increased rapidly; for instance, Chapman (1979) demonstrates its relatively low cost and high accuracy of using CFD as an assistant tool for aeroplane design. More recently, modern CFD packages can deal with complex problems in a wide range of research and industrial areas, including aerodynamics, hydrodynamics, power or industrial systems, chemical process engineering, biological engineering, environmental engineering, coastal and coastal marine engineering, electrical and electronic engineering, etc.

CFD codes are structured around numerical algorithms which can deal with fluid flow problems. The main elements of the methodology in most mesh-based CFD codes include space discretization, equation discretization and solution algorithm (Gosman, 1999). In addition, some CFD codes also cater for mesh generation and setup options along with solution control and results display. Currently, there are three distinct streams of numerical solution techniques: the Finite Volume Method (FVM, Hirt & Nichols, 1981), the Finite Element Method (FEM, Neuman & Witherspoon, 1970) and the Finite Difference Method (FDM, Harlow & Welch, 1965). The finite volume methodology is employed in most well-established commercial CFD packages, e.g., CFX, ANSYS/FLUENT, STAR-CCM+, FLOW3D etc. The key feature of these mesh-based numerical methods is to divide a continuum computational domain into discrete subdomains (i.e., meshes). Then, the governing equations are converted to algebraic equations with field variables based on these properly defined meshes. In particular, it is noted that the accuracy of CFD results is primarily dominated by the quality of meshes (Beall et al., 2004). Taha (2005) further pointed out that over half

of the time spent on CFD simulations is devoted to mesh generation. Thus, one of the major issues of using CFD is to access robust meshing techniques. While the generation of meshes continuously poses challenges to computational scientists, meshless methods applied to CFD have become a relatively new field of research.

Through developments in informatics, the usage of CFD is virtual in almost every sector. Nevertheless, it is still too early to think it has become a mature technology. Moreover, according to Bhatti et al. (2020), specific gaps need to be fulfilled; for instance, there are challenging questions linked with turbulence, heat transfer and combustion modelling, discretization and solution methods, etc. In summary, the research on CFD and relevant disciplines is still ongoing.

2.2 Meshless methods applied to CFD

2.2.1 Motivation for developing meshless methods

According to Zienkiewicz et al. (2000), the simulation of fluid flow problems relies on mesh-based schemes with most existing numerical methods. Over the past decades, mesh-based numerical schemes like FDM, FVM and FEM have achieved great success in simulating a wide range of fluid flow problems. For example, Yan & Ma (2010) developed FEM models to study potential flow problems, showing satisfactory results for 3-dimensional wave interactions with floating bodies and fixed structures. The well-

established open-source FVM fluid package OpenFOAM has been widely used to simulate wave propagation, wave generation, and wave-structure interaction problems (Higuera et al., 2013; Chen et al., 2014). Tran & Kim (2016) used the STAR-CCM+ package to investigate the hydrodynamics of floating structures (e.g., offshore wind turbine platforms). More recently, Gong et al. (2021) developed a hybrid model, which is based on the CFD tool OpenFOAM coupling with the FNPT-based (fully nonlinear potential flow theory) QALE-FEM (quasi arbitrary Lagrangian Euler finite element method) and the viscous flow method, is used to simulate the motion of trimaran in the stern waves. While the mesh-based methods are already widely used to study fluid flow problems, the motivation behind developing meshless methods is worthwhile to be discussed.

Specifically, above mentioned mesh-based methods have certain limitations for treating problems involving free surfaces. According to Agarwal et al. (2021), these mesh-based models require additional numerical treatment and extra computational expense to compute breaking and overturning waves. The meshes need to be of sufficient quality in specific regions to ensure the deformed free surface is well identified and tracked. According to Agarwal et al. (2021), earlier mesh generation techniques, such as the adaptive meshing method, are computationally expensive for ensuring body-conforming meshes at each time step. Moreover, additional complexity can be introduced for modelling problems with moving or complex geometries. Some advanced mesh generation techniques have been developed in recent years, including the overset method (Ma et al., 2018), the Cartesian cut-cell method (Xie & Stoesser, 2020), etc. However, Agarwal et al. (2021) pointed out that implementing

boundary conditions in these techniques and controlling the mesh size around the geometry might still be challenging.

Bypassing the use of meshes, the meshless methods do not require connection between nodes of the computational domain, i.e., the meshes, but are rather based on interactions of each node and its neighbours. Compared with mesh-based methods, meshless methods have become a focus in the past few decades due to the following unique advantages. Firstly, the process of generating meshes is costly and time-consuming in earlier mesh-based methods, while meshless methods have no such consideration. Secondly, using meshless methods can improve accuracy for simulating cases with sophisticated or over-deformed geometry. Liu (2002) indicated that using mesh-based methods is unsuitable for studying the propagating wave with the largely-deformed free water surface. Yan et al. (2020) further indicated that meshless methods are superior to mesh-based methods in dealing with fluid flow problems with large deformation. Thirdly, meshless methods have a distinct advantage when the main concern is about discrete particles rather than continuums (Hockney & Eastwood, 1988). Finally, another distinguishing feature of developing meshless methods is that the implementation of the Lagrangian approach can omit the potential numerical diffusions, which are mainly caused by the mesh skewness (Yan & Ma, 2020; Michalcová & Kotrasová, 2020).

By using a set of particles to represent the whole continuous system, several novel meshless methods have been developed in recent decades; these include the Moving-particle Semi-implicit Method developed by Koshizuka & Oka (1996), the Finite Point Method (Oñate et al. 1996), the Element-free Galerkin Method (Belytschko et al. 1994), the Diffusion

Element Method (Nayroles et al. 1992), to name but a few. Due to the limitation of the scope of this thesis, two meshless methods, i.e., Smoothed Particle Hydrodynamics (SPH) and the Meshless Local Petrov-Galerkin (MLPG) method, are further introduced in the following sections.

2.2.2 Meshless Local Petrov-Galerkin method

Meshless Local Petrov-Galerkin (MLPG), as a Langrangian meshless method, was developed by Atluri & Zhu (1998) and Atluri & Shen (2002). As its name suggests, the MLPG method does not use any mesh to discretize the problem domain, and the local weak form of governing equations is applied over the local subdomains. In addition, the test or trial functions can differ from the same functional domain in the Petrov-Galerkin method, which makes MLPG effective in solving numerous fluid flow problems with high feasibility (Ma, 2005a). Recently, an excellent article by Sriram & Ma (2021) has reviewed the developments and applications of the MLPG method. Herein, some numerical developments in the MLPG method are introduced in the following context.

Since the MLPG method was proposed, a number of studies have shown that the MLPG method is very suitable for the simulation of fluid flow problems without free water surface (Atluri & Zhu, 1998; Lin & Atluri, 2000). Ma (2005a) is reported to be the first to develop the MLPG method for simulating water waves. Ma (2005a) adopted the simple Heaviside step function as the test function to formulate the weak form over local domains, which produced encouraging results in terms of solving pressure gradient.

After that, Ma (2005b) changed the test function from the Heaviside step function to the solution for Rankine sources and formed the new MLPG_R method, which is particularly suitable for simulating nonlinear waves. Remarkably, it is reported that using the MLPG_R method can save half of the CPU time compared with using the MLPG method. In Ma (2008), a new numerical discretization scheme, called the simplified finite-difference interpolation (SFDI), was proposed for the MLPG_R method, which can achieve the same or better results as that of using the classic Moving Least Square (MLS) interpolation scheme but cost less computational time. The MLPG_R method is further applied for simulating 2D breaking waves (Ma & Zhou, 2009; Sriram & Ma, 2010), 3D breaking waves and wave-cylinder interactions (Zhou & Ma, 2010). In Sriram et al. (2014), a hybrid model, which involves different governing equations for the different regions of computational domains, was introduced for modelling breaking and non-breaking waves. More recently, Zhou et al. (2017) firstly attempted to use the MLPG_R method for simulating 2D flows of two immiscible fluids. In Zhou & Dong (2018), the MLPG_R method was extended to be used for wave porous modelling.

Despite massive progress in developing the MLPG method, it can still be improved in terms of turbulence and boundary layer, boundary treatment methods, variable particle resolution, 3D modelling and coupling, computational aspects, particle shifting strategy, and benchmark studies (Sriram & Ma, 2021). In particular, the implementation of solid boundary conditions should be further improved because the commonly used solid boundary scheme, which directly discretizes the pressure Neumann boundary condition, remains inconsistent in the formulations for boundary particles and inner fluid particles. Additionally, numerical errors cannot be

ignored in the calculation of a gradient term. Linked with the research purpose of the present study, a numerical improvement regarding the solid boundary scheme will be proposed for the development of MLPG.

2.2.3 Smoothed Particle Hydrodynamics

Smoothed Particle Hydrodynamics (SPH) was initially developed by Gingold & Monahgan (1977) and Lucy (1977) to study astrophysical computations and later extended to many other fields such as coastal and ocean engineering (Gotoh & Khayyer, 2018; Luo et al., 2021; Lyu et al., 2022), free-surface flows (Gómez-Gesteira et al., 2010; Violeau & Rogers, 2016), multiphase flows (Wang et al., 2016) etc. Lind et al. (2016) summarized the diversification of SPH by focusing on its applications and challenges.

Since the fluid phase is usually considered incompressible (Liu et al., 2013), the incompressible condition was realized by treating the flow as weakly compressible with an appropriate equation of state (Monaghan, 1994) or strictly incompressible through solving the Poisson equation for pressure (Cummins & Rudman, 1999; Shao & Lo, 2003). In the weakly compressible SPH (WCSPH) method, the explicit solution of pressure is conveniently parallelizable (Luo et al., 2021). However, Meringolo et al. (2017) pointed out that early studies using the WCSPH scheme may suffer from the problem of spurious pressure fluctuations due to acoustic perturbations and local approximations. In the incompressible SPH (ISPH) method, the pressure is solved by the pressure Poisson equation derived based on the

projection scheme. According to Luo et al. (2021), a major advantage of ISPH compared with the WCSPH is that the spurious pressure fluctuations can be significantly alleviated by adopting the projection-based scheme.

A recent review article by Vacondio et al. (2021) introduced some challenges of the SPH method, including convergence, consistency, stability, boundary conditions etc. Regarding consistency, Monaghan (1989) pointed out that particle inconsistency may lead to poor accuracy of the SPH solution. Monaghan (1994) thus developed symmetrisation formulations to improve the accuracy through the restoration of consistency, and satisfactory results were reported by using such formulations in Morris (1996). Bonet & Kulasegaram (2002) provided a corrective SPH (i.e., CSPH) method aiming to increase the computational accuracy both in the problem domain and around the solid boundary. It is reported by Liu et al. (2003) that CSPM has better particle consistency performance. Furthermore, Liu et al. (2005) introduced a new technique to approximate field variables using the basis function at particles. This idea was further developed by Fang et al. (2006) to the free surface flow with incomplete support domains. Other notable corrections or modifications of the SPH method include the reproducing kernel particle method (Chen et al., 1996), the moving-least square-particle hydrodynamics (Dilts, 1999), the integration kernel correction (Bonet & Kulasegaram, 2000), stable particle method (Rabczuk et al., 2004), etc. For more details of the challenges of SPH method, readers are referred to Vacondio et al. (2021).

Overall, researchers have made great efforts to develop the SPH method over the past few decades, and it shows promising potential for simulating fluid flow problems. In Section 2.4.3, a further discussion of SPH in the

application of multiphase flows will be presented. In Chapter 5, a newly developed two-phase ISPH model for studying suspended sediment motion problems will be proposed.

2.3 Boundary treatment in meshless methods

2.3.1 Free surface

In most simulation cases, the free surface can be recognised as the interface between the water surface and open air. In hydrodynamics, the capacity to track large-deformed free surfaces is an evident advantage of meshless particle methods (Liu & Liu, 2003). According to Luo et al. (2021), the water surface is governed by the kinematic or dynamic boundary condition. The kinematic boundary condition represents the zero-mass transfer across the interface on a macroscopic scale. The dynamic boundary condition, i.e., the Dirichlet pressure condition, implies continuous pressure at the interface without considering the surface tension.

Golagrossi et al. (2009) pointed out that the kinematic boundary condition is automatically satisfied in some single-phase meshless methods like WCSPH. However, its implementation might have difficulties due to possible numerical errors and perturbative particle motions (Luo et al., 2021). This is because the explicitly solved pressure cannot guarantee the continuity of stress through the continuous free surface. With this respect, Wang et al. (2019) applied a background mesh scheme to enhance the

solution of pressure at the free surface. You et al. (2021) has reported that using the background mesh scheme can improve the satisfaction of kinematic free surface boundary condition in the WCSPH framework.

In incompressible particle methods, the Dirichlet pressure condition (i.e., the zero pressure condition) is generally imposed on the free surface for the single-phase flow problems (Shao & Lo, 2003). As problems associated with numerical errors and perturbative particle motions remain, the dynamic free surface boundary condition can be improved by applying the background mesh scheme. In addition, for projection particle methods, some misjudgements can happen due to the problematic identification of free surface particles as the free surface can deform violently. According to Luo et al. (2021), three approaches for identifying free surface particles are widely employed. The first approach applies a kernel-based interpolated indicator at the target particle and its neighbouring particles. The indicators can be defined by particle density, particle position or summation of coordinates (Lee et al., 2008; Khayyer et al., 2009). The second approach uses the geometrical indicator by analysing the geometrical relationship between particles (Koh et al., 2012; Suchde, 2021). And the third approach is a combination of using the kernel-based interpolated indicator and geometrical indicator (Marrone et al., 2012; Liu et al., 2014; Sun et al., 2017). A more detailed discussion related to the advantages and applications of using kinematic and dynamic boundary conditions is reported in Luo et al. (2021).

2.3.2 Solid wall

Reliable solid boundary treatment methods can significantly impact the performance of meshless particle methods (Lind et al., 2020). Although some commonly used solid boundary treatment methods have been proposed along with the development of particle methods, challenges linked with stability and accuracy still exist. For example, Vacondio et al. (2021) addressed relevant issues caused by kernel truncations, the solid boundary with complex geometries, and boundary conditions under complex flow regimes.

There are two boundary conditions to be considered on the impermeable solid boundaries (Morikawa et al., 2019). The first one is to prevent the fluid particles from penetrating the solid walls, which can be named as the pressure wall boundary condition (i.e., the pressure Neumann boundary condition). The pressure Neumann boundary condition states that the acceleration of the inner fluid particles approaching the solid walls in the direction of the wall should be zero. The second condition is to choose the correct slip condition (i.e., velocity wall boundary condition). In general, the velocity wall boundary condition contains the free slip boundary condition, no-slip boundary condition and partial slip boundary condition. The no-slip means that the fluid velocity in direct contact with the solid boundary is identical to the velocity of this solid boundary, and relative movement is not existing between the fluid layer in direct contact and the solid wall. For viscous flows, the fluid particles should adhere to the solid boundaries. Thus the Neumann boundary condition for pressure and the no-slip boundary condition for velocity is usually applied. In particular, Rijas et al. (2019) pointed out that problems involving wave-structure interactions

should employ the no-slip condition for higher accuracy. In general, the free-slip boundary condition can be used in most engineering simulations because of lower computational expense without resolving the rapid change of tangential velocities on the solid walls (Luo et al., 2021). However, it is noted that the free-slip boundary condition should not be imposed for modelling fluid flow problems involving the boundary layer effects (Sriram & Ma, 2021).

So far, several boundary treatment approaches have been developed for the SPH method. According to Chen (2020), boundary treatment methods in SPH can be categorized into the particle representation type and the geometrical representation type. For the particle representation type, the fixed boundary particles are assigned additional forces to prevent fluid particles from penetrating and thus producing specific boundary conditions. The typical particle representation approaches include the repulsive force approach (Monaghan, 1994; Monaghan & Kajtar, 2009; Shadloo & Yildiz, 2011; Monaghan & Mériaux, 2018), the ghost or image particle approach (Morris et al., 1997; Liu et al. 2012; Bierbrauer et al., 2009) and the dynamic particle approach (Liu & Liu, 2003; Gómez-Gesteira & Dalrymple, 2004; Gong et al., 2009). Another type is represented by the semi-analytical approach, which redefines the solid boundary by edge particles (Kulasegaram et al., 2004).

In the repulsive force approach, the wall boundary condition is imposed by applying the repulsive force on fluid particles approaching solid walls to prevent them from penetrating the boundaries. This approach is capable of dealing with complex geometries at the boundary, but errors can be introduced due to the kernel truncation near the boundaries (Fourtakas et

al., 2019). It is also reported that, in the static fluid test, particles near the wall boundaries undergo spurious movement (Ferrand et al., 2013). In the image particle approach, extra particles are generated beyond the wall boundaries with prescribed physical quantities (e.g., pressure and density) the same as fluid particles. The velocities and positions of the image and fluid particles are set to be symmetrical with respect to the tangent of the boundary. The image particle approach can effectively prevent non-physical behaviours (Leroy et al., 2014) and improve the overall accuracy (Hosseini & Feng, 2011). However, challenges still remain in generating and adopting those particles, especially for computational domains with complex geometries. Furthermore, the computational cost for this approach is considerable due to image particle generation and movement (Wang et al., 2016). The dynamic particle approach uses virtual particles fixed beyond the wall boundaries with flow properties obtained from neighbouring fluid particles through linear extrapolation (Chen, 2020). According to Wang et al. (2016), the problem related to boundary deficiency for virtual particles still exists and may lead to inaccurate results in solving the pressure field. The semi-analytical approach is proposed by introducing a renormalization factor for fluid particles close to the wall boundaries (Kulasegaram et al., 2004; Ferrand et al., 2013; Mayrhofer et al., 2015). This approach improves the interpolation accuracy at the wall boundaries, but the difficulties in applications for complex boundary geometries remain (Valizadeh & Monaghan, 2015).

Although MLPG has many similarities with some meshless methods like ISPH or MPS (i.e., moving particle semi-implicit method) regarding gradient estimation, projection scheme or free surface identification etc., Sriram & Ma (2021) indicated that the implementation of solid boundaries is different

in MLPG. Specifically, Zhou et al. (2008) figured out that many solid boundary approaches in SPH mainly ensure the velocities to satisfy the boundary conditions on the solid walls. Nevertheless, the pressure is not guaranteed to satisfy the solid boundary conditions. According to Ma (2005a), solid boundary approaches in MLPG were initially based on the weak formulation of flow governing equations over the incomplete sub-domains of the boundary particles but were only applied to solve the potential flow (Atluri & Zhu, 1998) and inviscid flow with artificial stabilizing term to suppress spurious pressure (Lin & Atluri, 2001). When the MLPG method was extended to simulate non-linear waves (Ma, 2005a), the wall boundary condition was imposed by direct discretization of the pressure Neumann boundary condition. This wall boundary treatment approach excludes artificial stabilizing terms and prevents fluid particles from penetrating the wall with flow viscosity considered. Considering the pressure Neumann boundary condition, a numerical study of three schemes regarding the direct discretizing approach is investigated by Zhou et al. (2008), including two in MPS with single and three layers of boundary particles (Koshizuka & Oka, 1996; Hibi & Yabushta, 2004; Zhang et al., 2006) and one in MLPG based on simplified finite-difference interpolation (SFDI) (Ma, 2008). In Koshizuka & Oka (1996), the solid boundary approach directly discretizes the boundary particles for solving pressure. The formulation and discretized equations for solid boundary particles and inner fluid particles remain the same. It is reported that the approximation of the Laplacian operator of pressure term is not very accurate on the solid boundaries since incomplete influence domain (i.e., truncated influence domain) and irregularly distributed fluid particles (Zhou et al., 2008). Zhou et al. (2008) also addressed that this approach cannot ensure the solved pressure to satisfy the solid boundary condition based on a simple analysis. Hibi & Yabushta (2004) and Zhang et al. (2006) further developed the

discretizing boundary approach by setting additional layers of solid particles in the outer region along the solid walls. In this approach, three layers of solid particles are included for solving the pressure, while only a single layer of solid particles is solved in Koshizuka & Oka (1996). Zhou et al. (2008) figured out that although the accuracy has been improved to a certain degree in this approach and the solid boundary condition can be roughly satisfied, spurious wiggles of solved pressure are observed.

In summary, current solid boundary approaches have their own advantages and disadvantages, and the careful choice of a suitable approach under various flow conditions is essential to accurate simulations. The development of boundary treatment methods is still ongoing and crucial, with increasing attention to a universe approach. An improved boundary scheme for treating solid boundaries will be presented in Chapter 4 with validations on accuracy, convergence and adaptability.

2.4 Multiphase flow

2.4.1 Multiphase flow

Multiphase flow describes a wide range of natural and industrial problems. In the context of fluid mechanics, multiphase flow is usually defined as a system where different phases (i.e., liquids, solids, gases) are flowing simultaneously. The most used categorization of multiphase flows, referring to Yeoh & Tu (2019), depends on the state of different phases.

Nevertheless, according to Prosperetti & Tryggvason (2007), a precise definition of multiphase flow should be formulated based on its specific situation and intrinsic characteristics. For example, fluids can be considered as multiphase flow with the same substance, such as the mixture of liquid and its vapour. Consequently, the classification of the multiphase phase should not be limited to a single set of standards. Herein, four types of multiphase flow are introduced in the following context.

Liquid-gas flow

An example of liquid-gas flow is the motion of bubbles in a flow. The gas phase (i.e., bubbles) features considerable difficulties as bubbles deform freely within the liquid phase and present different geometrical shapes (e.g., spherical, ellipsoidal, distorted, etc.). Bubble interactions like coalescence or break-up can change the interfacial structure and further reflect the ubiquitous challenges. Hibiki et al. (2006) investigated existing liquid-gas two-phase flow systems with particular attention to the interfacial area and further classified general liquid-gas flows as the dispersed type (e.g., gas bubbles in liquid), the mixed or transitional type (e.g., gas pocket in liquid) and the separated type (e.g., the liquid film in gas).

Gas-solid flow

Gas-solid flow (e.g., sandstorms, smoke with fine soot particles etc.) is generally concerned with the motion of solid particles suspended in the gas phase. A key feature of gas-solid flows is that the mass transfer can be

neglected. Yeoh & Tu (2019) demonstrated that the gas-solid flow could be divided into dilute and dense flows. According to the critical value linked with particle density, the motion of solid particles is dominated by the gas phase in dilute flows. In contrast, the particle-particle interactions can significantly affect the flow regime of the dense flows (Li et al., 1998).

Liquid-solid flow

Common natural phenomena related to liquid-solid flow include sediment transport, mudslides, soil erosion in rivers, estuaries, or other coastal areas. Many industrial applications, such as fluidised and slurry transportation flotation, are also involved. Many studies of liquid-solid flow problems fundamentally solve the motion of individual solid particles. According to Yeoh & Tu (2019), both phases in the liquid-solid flows are driven by the pressure gradient due to their relatively low ratio of density. Furthermore, Prosperetti & Tryggvason (2007) pointed out that more attention should be paid to the balance of drag and lift forces, which can significantly affect the motion of particles.

Liquid-liquid flow

Liquid-liquid flows are generally considered as immiscible flows. Some examples like the fuel-cell system or the extraction system have already been intensively applied in industries. According to Quan et al. (2009), an appropriate liquid-liquid two-phase model should demonstrate the

capability to accurately simulate the interface of liquid-liquid two-phase flows and handle its possible large deformation.

Despite above mentioned multiphase flow classification, Brennen (2014) proposed a more general classification according to two topologies of multiphase flow, namely the disperse flow and the separated flow. In disperse flows, the flow pattern is one phase consisting of discrete elements (e.g., drops, bubbles or particles) distributed in the continuous phase, such as particles in a liquid or droplets in a gas. According to Godino et al. (2020), the disperse flow is characterized by the volume of discrete elements, and the motion of discrete components is affected mainly by the interfacial forces rather than the inertial forces. In contrast, the separated flow, which is recognised as a continuous-continuous system, is characterized by large interfacial length scales. In addition, according to the presence of heat transfer, flow direction or the number of phases, other classifications of multiphase flow can be found in Yadigaroglu & Hetsroni (2018). Some other classifications related to the multiphase flow problems can be found in Prosperetti & Tryggvason (2007) and Yeoh & Tu (2019).

It is clear that above mentioned physical phenomena involving multiphase flows have little in common. As a result, each multiphase flow system needs to be specifically and solely analysed. According to Ishii & Hibiki (2010), experiments, theoretical analysis, and computational modelling are the essential tools throughout the study of multiphase flows. Herein, these three research approaches are worth to be discussed, as shown in the following context.

Experimental approach

The experimental approach has made significant contributions for understanding the dynamic behaviours of multiphase flows and is commonly used to validate empirical equations or numerical models (Kiger & Pan, 2000; Khalitov & Longmire, 2002; Powell, 2008; and Balachandar & Eaton, 2010). It is evident that obtained experimental data is the fundaments of all research methods. In the past several decades, numerous laboratory experiments have been conducted to explore such complex physical processes like sediment transport under various flow conditions (Dohmen-Janssen & Hanes, 2002; Noguchi & Nezu, 2009; O'Donoghue & Ribberink, 2010), sediment deposition and suspension problems (Nakasuji et al., 1990; McNamee, 2000; Bühler & Papantoniou, 2001), submarine landslide and granular collapse (Lacaze et al., 2008; Rondon, 2011), etc.

Theoretical approach

In general, theoretical studies of multiphase flow aim to use mathematical equations to predict the flow behaviours and explore the flow characteristics based on obtained experimental data (Drew & Segel, 1971; Delhaye, 1978; Drew, 1983; Bouré, 1987; Liu & Zhu, 1988). At the early stage of research on multiphase flows, diverse mechanisms are obtained based on data from laboratory test facilities (Gidaspow, 1994). Drew (1983) presents a good review of mathematical modelling of two-phase fluid flows among numerous theoretical studies.

Computational approach

The computational approach uses the size and power of modern computers to address the complexity of multiphase flows (Brennen, 2014), and it has become an essential tool for solving practical multiphase flow problems (Prosperetti & Tryggvason, 2007). Building full-size experimental models might be available in some applications on the laboratory scale, but it can also be very time-consuming and expensive. Furthermore, the lack of necessary control in many instances is another significant challenge in setting up an experimental model. Compared with the single-phase flow simulation, the complexity of multiphase flows involves immiscible or miscible phases, change of volume fraction of different phases, relative velocities among phases, changing interface, different flow regimes, thermodynamic disequilibrium, heat transfer, turbulence etc., arises as a critical feature. Consequently, these realistic difficulties limit the usage of the pure theoretical or experimental approaches for understanding the mechanism of some multiphase flow problems. With this respect, the development of computational capacities has marked a decisive moment for the applications of computational methods. Thanks to the high-speed computers and improved understanding of multiphase flow mechanics, modelling every detail under various flow conditions has no longer been an unattainable goal by using the computational approach.

2.4.2 Modelling of sediment transport

In the estuaries, ports, and other coastal environments, understanding sediment transport has been a critical focus for many decades. Knowledge

of the process of sediment transport is vital for managing and developing water and land resources (Davidson-Arnott et al., 2019). The erosion, deposition, and movement of sediments in the water column represent the main physical processes of sediment transport (James et al., 2010). By definition, erosion means the sediment particles enter the water column from the sediment bed, whereas deposition is the process of sediment particles back to the sediment bed from the water column (Dronkers, 2005 Yeganeh-Bakhtiary). The movement of sediments involves the process of settling, turbulent dispersion etc. The early study of sediment transport was mainly conducted by field experiments and supporting mechanics (Vanoni, 1946; Einstein,1950; Vanoni, 1975; Van Rijn, 1984; Dyer, 1995; Dibajnia & Watanabe, 1998; Chien & Wan, 1999; Noguchi & Nezu, 2009; O'Donoghue & Ribberink, 2010). In the aspects of extendibility and accuracy, the numerical modelling approach based on modern computers has been developed as an effective tool for studying sediment transport mechanisms (Ishii & Hibiki, 2010).

As the process of sediment transport can be naturally treated as a two-phase flow problem, various two-phase models have been proposed over the past few decades (Dong & Zhang, 2002; Chang & Hsieh, 2003; Jha & Bombardelli, 2009; Chen et al., 2011; Shi & Yu, 2015; Lee & Huang, 2018). Among most existing simulations, the mesh-based Eulerian framework might be the most commonly used numerical method (Fonty et al., 2019). Depending on how they treat the sediment phase, these mesh-based Eulerian methods can be categorized into the Eulerian-Eulerian and Eulerian-Lagrangian type.

In the Eulerian-Eulerian type, each phase is described as a continuum and satisfies the conservation laws for mass, momentum, and energy. Computing the statistical properties of the sediment phase is its main feature. Since the less required computational resources, the Eulerian-Eulerian method has been intensively employed for the sediment transport problems; some examples can be found in Dong & Zhang (1999), Dong & Zhang (2002), Jha & Bombardelli (2009), Chen et al., (2011) etc. Unlike the pure Eulerian type, the Eulerian-Lagrangian method treats the solid phase as a dispersed phase and tracks the motion of the individual solid particle. Emphasizing fluid-particle or interparticle interactions is a crucial feature of the Eulerian-Lagrangian two-phase model. In recent years, applications of the Eulerian-Lagrangian model have received extra attention. In a practical problem, Shi & Yu (2015) developed an Eulerian-Lagrangian model for simulating suspended sediment transport in a steady open channel. An empirical formula is used for computing the fluid velocities for simplicity, and sediment particles are solved based on the equation of motion. The implementations of the Eulerian-Lagrangian model have been an ongoing concern in Drake & Calantoni (2001), Schmeeckle & Nelson (2003), Yeganeh-Bakhtiary et al. (2009), Ji et al. (2013), Shi & Yu, (2015), etc.

In summary, it is undeniable that the mesh-based Eulerian method plays a dominant role in the simulation of sediment transport and other relevant research fields. Although using mesh-based Eulerian methods remains difficult in terms of large deformation or discontinuities, it still offers satisfactory accuracy and efficiency to many researchers under significant efforts devoted.

2.4.3 Multiphase SPH model

As the requirement for accurate modelling increases, the popularization of the meshless method has attracted more attention in recent years. SPH, as a pure meshless Lagrangian method, is naturally extended to the multiphase simulation (Zhang et al., 2017). According to Chen (2020), two-phase SPH modelling provides a more suitable solution for issues like discontinuities and large interfacial deformations. Based on the continuous description, different phases in the multiphase SPH model are followed by the volume fraction representation. With this respect, two models are used to address the phase representation.

The first one is the so-called two-phase or two-fluid model, which treats two phases separately with a distinct interface (Stewart, 1979; Ishii & Mishima, 1984; Gidaspow,1994). According to Ishii & Mishima (1984), each phase should be considered separately, and the two phases, considering liquid-solid two-phase flow as an example, are coupled by interaction terms (i.e., the drag term) which are generally explicitly solved. Monaghan & Kocharyan (1995) generalised the equations for the two-phase model using the SPH method and extended the model to liquid-gas and liquid-liquid simulations in such SPH implementations. The interphase interactions are closed by employing a simplified constant drag law. In Monaghan (2005), such a model based on SPH is extended to the dense multiphase flow problems like the fluidization of granular materials. Similarly, Xiong et al. (2011) proposed a two-phase SPH model to solve fluidization problems, emphasising the critical shear stress and drag force.

In the SPH mixture models, the fluid is seen as a single-fluid flow with only one set of discretized SPH particles. Each SPH particle combines two-phase properties and is governed by one continuity equation and momentum equation. The volume fraction is introduced in this model to define the field variables (e.g., pressure, velocity, etc.). It is naturally possible to evaluate the evolutions of changes in the volume fraction of each SPH particle. Ren et al. (2014) implemented the SPH mixture model to capture various physical phenomena by the closure of drift velocities. The nonuniformly distributed velocity fields lead to the change of volume fraction of each phase. More recently, a mixture model was proposed by Wang et al. (2017) to investigate the submerged granular column collapse. Fonty et al. (2019) extended the two-phase SPH mixture model to high-density ratio problems (i.e., sand dumping in a tank).

The coupling of SPH with other discrete methods or mesh-based methods remains a potential option. Potapov et al. (2001) developed a SPH model coupling with the discrete element method (DEM) for simulating fluid-solid flow problems. Huang & Nydal (2012) presented the SPH-DEM model for simulating the motion of solids in a sedimentation tank. Marrone et al. (2016) demonstrated a SPH model coupling with the finite volume method for simulating free surface flows, and Zhang et al. (2018) coupled SPH with the finite element method for particle sedimentation.

Chapter 3: Methodology

3.1 Governing equations and numerical procedure

The purpose of this section is to introduce the governing equations following the basic physical principles (i.e., the mass and momentum conservation laws). The single-phase governing equations used for solving the incompressible fluid domain are continuity and momentum equations, which are given by,

$$\nabla \cdot \boldsymbol{u} = 0 \tag{3.1}$$

$$\frac{D\boldsymbol{u}}{Dt} = -\frac{1}{\rho}\nabla p + \boldsymbol{g} + v\nabla^2 \boldsymbol{u} \tag{3.2}$$

where $\boldsymbol{u}$ is the fluid velocity vector, ρ is the fluid density, p is the fluid pressure, $\boldsymbol{g}$ is the gravitational acceleration, and v is the kinematic viscosity of the fluid.

The above governing equations Eqs (3.1) and (3.2) are employed in various meshless methods for modelling the single-phase fluid flows. Similar to the two-step projection method proposed by Chorin (1968), the prediction-correction numerical scheme is widely used in the MLPG and SPH methods to solve the Navier-Stokes equations based on the assumption of incompressible fluid. This numerical procedure consists of two steps. The first prediction step is an explicit solution accounting for the gravity and viscous stresses without enforcing the incompressible conditions. Then, the

pressure is implicitly solved based on the pressure Poisson equation (PPE) formulated by combining the continuity and momentum equations. Finally, the particle velocities and positions are updated based on the solved pressure. Herein, the numerical procedure during each time step contains the following steps:

(1) Prediction step (evaluate intermediate velocities and positions)

$$\boldsymbol{u}^{*} = \boldsymbol{u}^{\boldsymbol{n}} + (v\nabla^{2}\boldsymbol{u}^{\boldsymbol{n}} + \boldsymbol{g}\,)\Delta t \tag{3.3}$$

$$\boldsymbol{r}^{*} = \boldsymbol{r}^{\boldsymbol{n}} + \boldsymbol{u}^{*}\,\Delta t \tag{3.4}$$

where $\boldsymbol{r}$ is the position vector; Δt is the time step; the superscripts n represents the physical values at the n^{th} time step; notion * represents the intermediate time step between t_n and t_{n+1}.

(2) Implicitly evaluate pressure p^{n+1} from the pressure Poisson equation

$$\nabla^{2}p^{n+1} = a\frac{\rho^{n+1} - \rho^{*}}{\Delta t^{2}} + (1-a)\frac{\rho}{\Delta t}\nabla\cdot\boldsymbol{u}^{*} \tag{3.5}$$

where a is an artificial coefficient with a value ranging from 0 to 1; ρ^{n+1} and ρ^{*} is the fluid density at $(n+1)^{th}$ time step and intermediate time step, respectively;

(3) Correction step (update particle velocities and position)

$$\boldsymbol{u^{n+1}} = \boldsymbol{u^{*}} - \frac{1}{\rho}\nabla p^{n+1}\Delta t \tag{3.6}$$

$$\boldsymbol{r^{n+1}} = \boldsymbol{r^{n}} + \boldsymbol{u^{n+1}}\Delta t \tag{3.7}$$

In the above modelling procedure, the adaption of Eq. (3.5) needs to be further discussed. In Ma (2005a), a is set to be zero for non-linear wave problems, and Zhou & Ma (2009) suggested a as 0.1 to 0.2 for breaking wave applications. Later, this problem was further investigated by Sriram & Ma (2010), and reported that a is better to be taken as zero. In the subsequent work, the value of a is taken as zero.

Besides, it is worth mentioning that a carefully controlled size of a time step is essential for accurate and stable computations in meshless methods. In general, the following Courant condition needs to be satisfied, and a detailed review can be found in De Moura & Kubrusly (2013).

$$C = \frac{u\Delta t}{\Delta l} \leq C_{max} \tag{3.8}$$

where u is the magnitude of the velocity, Δl is the initial particle spacing and C_{max} is the maximum value of the Courant stability condition, which is typically equal to $C_{max} = 1$.

3.2 Methodology of MLPG_R

3.2.1 MLPG_R formulations

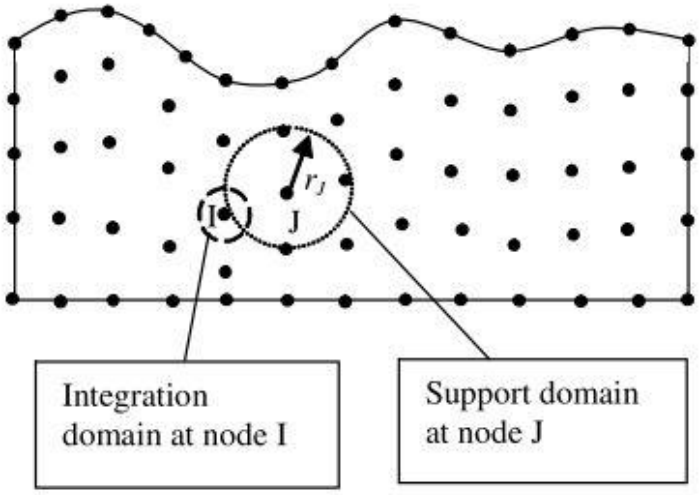

Figure 3.1. Illustration of nodes, integration domain and support domain (Ma, 2005b).

Replacing the test function from the Heaviside step function by the solution for Rankine sources, the original formulations of the MLPG_R method are given by Ma (2005b). As illustrated in Fig. 3.1, the computational domain is discretized by a set of randomly distributed nodes. At each of the inner fluid nodes, Eq. (3.19), i.e., the PPE, is integrated over a circular integration domain after multiplying by the Rankine source test function φ and yields

$$\int_{\Omega_I} \left(\nabla^2 p^{n+1} - \frac{\rho}{\Delta t} \nabla \cdot \boldsymbol{u}^* \right) \varphi \, d\Omega = 0 \tag{3.9}$$

$$\varphi = \frac{1}{2\pi} \ln\left(\frac{r}{R_I}\right) \tag{3.10}$$

where Ω_I is the area of the integration domain, r is the distance between the concerned node and the centre of the integration domain; R_I is the radius of the integration domain. The test function φ is made to satisfy $\nabla^2\varphi = 0$ in Ω_I and $\varphi = 0$ on its boundary $\partial\Omega_I$. More features of the test function (i.e. Rankine source solution) are demonstrated in Chapter 4.

The unknown Laplacian pressure operator, i.e., $\nabla^2 p$ in Eq. (3.23), can be reduced by adding a zero term $p\nabla^2\varphi$ and applying the Gauss's theorem

$$\int_{\Omega_I} \varphi \nabla^2 p \, d\Omega = \int_{\Omega_I} (\varphi \nabla^2 p - p\nabla^2 \varphi) \, d\Omega \tag{3.11}$$

and gives:

$$\int_{\Omega_I} \varphi \nabla^2 p \, d\Omega = \int_{\partial\Omega_I + \partial\Omega_\varepsilon} [\boldsymbol{n} \cdot (\varphi \nabla p) - \boldsymbol{n} \cdot (p \nabla \varphi)] \, dS \tag{3.12}$$

where $\partial\Omega_I$ is the boundary of the integration domain and $\partial\Omega_\varepsilon$ is a small surface surrounding the centre of Ω_I with a radius of R_ε. The reason for adding $\partial\Omega_\varepsilon$ is that the test function φ becomes infinite at $r = 0$, so Gauss's theorem cannot be used otherwise (Ma, 2005b).

Further applying Gauss's theorem to the intermediate velocity term of Eq. (3.23) yields

$$\int_{\Omega_I} \frac{\rho}{\Delta t}\varphi \nabla \cdot \boldsymbol{u}^* d\Omega = \int_{\partial\Omega_I+\partial\Omega_\varepsilon} \frac{\rho}{\Delta t}\boldsymbol{n}\cdot(\varphi \boldsymbol{u}^*)\, dS - \int_{\Omega_I} \frac{\rho}{\Delta t}\boldsymbol{u}^* \nabla\varphi \, d\Omega \qquad (3.13)$$

By eliminating the second-order derivatives in Eq. (3.9), it becomes

$$\begin{aligned} &\int_{\partial\Omega_I+\partial\Omega_\varepsilon} [\boldsymbol{n}\cdot(\varphi\nabla p) - \boldsymbol{n}\cdot(p\nabla\varphi)]\, dS \\ &= \int_{\partial\Omega_I+\partial\Omega_\varepsilon} \frac{\rho}{\Delta t}\boldsymbol{n}\cdot(\varphi \boldsymbol{u}^*)\, dS - \int_{\Omega_I} \frac{\rho}{\Delta t}\boldsymbol{u}^* \nabla\varphi \, d\Omega \end{aligned} \qquad (3.14)$$

as $\varepsilon \to 0$, it can be easily proven that

$\int_{\partial\Omega_I+\partial\Omega_\varepsilon} [\boldsymbol{n}\cdot(\varphi\nabla p)]\, dS = 0$

$\int_{\partial\Omega_\varepsilon} [\boldsymbol{n}\cdot(p\nabla\varphi)]\, dS = -p$

$\int_{\partial\Omega_I+\partial\Omega_\varepsilon} \frac{\rho}{\Delta t}\boldsymbol{n}\cdot(\varphi \boldsymbol{u}^*) dS = 0$

Finally, Eq. (3.9) can be manipulated to the following form

$$\int_{\partial\Omega_I} \boldsymbol{n}\cdot(p\nabla\varphi)\, dS - p = \int_{\Omega_I} \frac{\rho}{\Delta t}\boldsymbol{u}^* \nabla\varphi \, d\Omega \qquad (3.15)$$

It is noted that the above MLPG_R formulations and the corresponding Eq. (3.15) have remarkable features compared with the original MLPG formulations (Atluri & Zhu, 1998; Atluri & Shen, 2002; Ma, 2005a). For example, calculating the pressure gradient and divergence of intermediate velocities is not required in the current formulation, significantly improving overall accuracy. In this section, only inner fluid particles are discussed.

3.2.2 The MLS approximation scheme

According to Atluri & Zhu (1998), the meshless method can use a local interpolation or approximation to construct the original function with known values at randomly distributed particles to preserve the local character of the numerical implementation. The Moving Least Square (MLS) scheme is considered to be such a scheme and is commonly used in meshless methods, including the MLPG. In this section, the main purpose is to illustrate the MLS approximation scheme briefly. More details are given by Lancaster & Salkauskas (1981) and Belytschko et al. (1994).

The MLS approximation scheme can be expressed as

$$p(\boldsymbol{x}) \approx \sum_{j=1}^{N} \Phi_j(\boldsymbol{x}) p_j \tag{3.16}$$

where N is the neighbouring particles which can affect the pressure at position $\boldsymbol{x}$; p_j is the nodal pressure and $\Phi_j(\boldsymbol{x})$ is the interpolation function, i.e., the shape function.

The shape function can be formulated as below, referring to Ma (2005b):

$$\Phi_j(\boldsymbol{x}) = \sum_{m=1}^{M} \Psi_m(\boldsymbol{x})[\boldsymbol{A}^{-1}(\boldsymbol{x})\boldsymbol{B}(\boldsymbol{x})]_{mj} = \Psi^T(\boldsymbol{x})\boldsymbol{A}^{-1}(\boldsymbol{x})\boldsymbol{B}_j(\boldsymbol{x}) \tag{3.17}$$

with the base function $\Psi^T(\boldsymbol{x}) = [1, x, y]$ for 2-dimensional cases, and the matrixes $\boldsymbol{B}$ and $\boldsymbol{A}$ can be defined as

$$B(\boldsymbol{x}) = \Psi^T \boldsymbol{W}(\boldsymbol{x}) \tag{3.18}$$

$$A(\boldsymbol{x}) = \Psi^T \boldsymbol{W}(\boldsymbol{x})\Psi = B(\boldsymbol{x})\Psi \tag{3.19}$$

and the matrix $\boldsymbol{W}(\boldsymbol{x})$ is given by

$$\boldsymbol{W}(\boldsymbol{x}) = \begin{bmatrix} w_1(\boldsymbol{x} - \boldsymbol{x_j}) & \cdots & 0 \\ \vdots & \ddots & \vdots \\ 0 & \cdots & w_N(\boldsymbol{x} - \boldsymbol{x_j}) \end{bmatrix} \tag{3.20}$$

where $w(\boldsymbol{x} - \boldsymbol{x_j})$ is the weight function.

Ψ^T is given by

$$\Psi^T = \begin{bmatrix} 1 & \cdots & 1 \\ x_1 & \cdots & x_N \\ y_1 & \cdots & y_N \end{bmatrix} \tag{3.21}$$

The MLS approximation can also be applied to partial or second-order partial derivatives, see Atluri & Shen (2002). In addition, the choice of the weight function is flexible as long as it is continuous and positive.

3.3 Methodology of SPH

3.3.1 Kernel approximation

The kernel approximation in SPH contains the representation of a function and its derivatives using the smooth function (Liu & Liu, 2010). The integral representation of a function $f(\boldsymbol{x})$ of the position vector $\boldsymbol{x}$ can be expressed as

$$f(\boldsymbol{x}) = \int_{\Omega} \delta(\boldsymbol{x} - \boldsymbol{x}') f(\boldsymbol{x}')\, d\Omega_{x'} \tag{3.22}$$

where the function $f(\boldsymbol{x})$ is defined on the domain Ω that contains $\boldsymbol{x}$; and $\delta(\boldsymbol{x} - \boldsymbol{x}')$ is the Dirac delta function given by

$$\delta(\boldsymbol{x}-\boldsymbol{x}')=\begin{cases}1, & \boldsymbol{x}=\boldsymbol{x}'\\ 0, & \boldsymbol{x}\neq\boldsymbol{x}'\end{cases} \tag{3.23}$$

Eq. (3.22) illustrates that the function f can be represented in an integral form. However, it is noted that the integral representation of function f cannot be used for constructing discrete models by simply introducing the Dirac delta function. This is because the Dirac delta function lacks some required properties like continuity and differentiability. As a result, the smoothing function W is introduced to replace the Dirac delta function, and the kernel approximation of function f becomes

$$\langle f(\boldsymbol{x})\rangle=\int_{\Omega} W(\boldsymbol{x}-\boldsymbol{x}',h)f(\boldsymbol{x}')\,d\Omega_{x'} \tag{3.24}$$

where h denotes the smoothing length that defines the influence area of the smoothing function W.

The smoothing function W should satisfy three basic conditions. The first one is the normalization condition (i.e., unity condition) which states

$$\int_{\Omega} W(\boldsymbol{x}-\boldsymbol{x}',h)f(\boldsymbol{x}')\,d\Omega_{x'}=1 \tag{3.25}$$

The second condition is the Delta function property as

$$\lim_{h\to 0} W(\boldsymbol{x}-\boldsymbol{x}',h)=\delta(\boldsymbol{x}-\boldsymbol{x}') \tag{3.26}$$

The third condition is the compact condition as

$$W(\boldsymbol{x}-\boldsymbol{x}',h)=0\ \forall\ |\boldsymbol{x}-\boldsymbol{x}'|>kh \tag{3.27}$$

where k is a constant related to the smoothing function for point at $\boldsymbol{x}$, and defines the effective (non-zero) area (i.e., the support domain or influence domain) of the smoothing function.

Despite the above three basic conditions, some properties of the smoothing function are also worth to be mentioned. For example, the positivity property states that the smoothing function should be non-negative within the support domain since it is important to ensure a meaningful physical phenomenon; the decay property indicates that a nearer particle should have a more significant influence on the concerning particle based on the physical consideration; the symmetric property means that particles from same distance but different positions should have equal effect on a given particle; the smoothness states that the smoothing function needs to be sufficiently continuous to obtain satisfactory computational results. Choosing a suitable smoothing function is very important in the SPH method since it can determine the pattern to interpolate and further define the computational accuracy and efficiency. A very good review related to

the SPH smoothing functions can be found in Liu & Liu (2010). Here, only two commonly used smoothing functions are given below:

The 2-dimensional cubic spline function used by Monaghan & Lattanzio (1985):

$$W(q,h)=\begin{cases}\frac{2}{3}-q^2+\frac{1}{2}q^3 & 0\le q<1\\ \frac{1}{6}(2-q)^3 & 1\le q<2\\ 0 & q\ge 2\end{cases} \tag{3.28}$$

The 2-dimensional quintic kernel function proposed by Wendland (1995):

$$W(q,h)=\frac{21}{16\pi h^3}\begin{cases}\left(1-\frac{q}{2}\right)^4(2q+1) & 0\le q\le 2\\ 0 & 2<q\end{cases} \tag{3.29}$$

In which $q=\frac{|x-x'|}{h}$.

3.3.2 Particle approximation

The particle approximation uses a set of particles to represent the computational domain and then estimates field variables based on these particles.

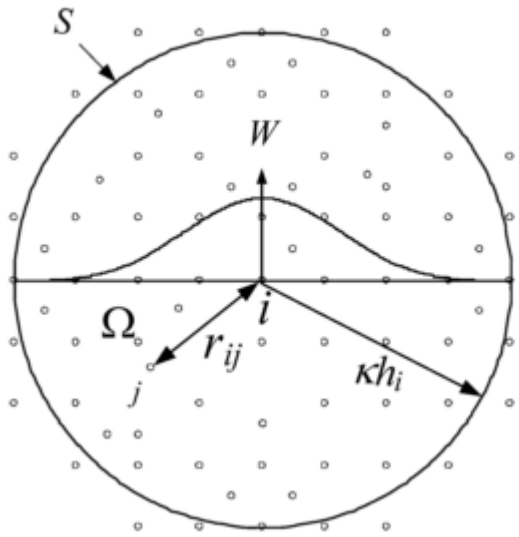

Figure 3.4. Particle approximations in a two-dimensional problem domain Ω with a surface S (Liu & Liu, 2010). W is the smoothing function to approximate the field variables at particle i based on neighbouring particles like particle j with the distance of r_{ij}.

As shown in Fig. 3.4, the discrete form of the integral approximation for the set of particles (e.g., particle j) representing the discretized continuum can be obtained by the particle approximation $\langle f(\boldsymbol{x_i})\rangle$:

$$\langle f(\boldsymbol{x_i})\rangle = \int_{\Omega_i} W(r_{ij}, h)\, f(\boldsymbol{x_j}) d\Omega_{x_j} \cong \sum_{j=1}^{N} f(x_j) W(r_{ij}, h) \frac{m_j}{\rho_j} \qquad (3.30)$$

where W is the smoothing function to approximate the field variables at particle i based on neighbouring particles like particle j with the distance of $r_{ij} = |\boldsymbol{x_i} - \boldsymbol{x_j}|$. The estimation of the function $f(\boldsymbol{x_i})$ is thus carried out as the sum of the values at its neighbouring particles by the smoothing function W.

It is worth to mention that the particle approximation, as shown in Eq. (3.30), converts the integral form of a field function to the discretized form based on the summations over a set of neighbouring particles. This approximation is the key to making the SPH method bypass the use of meshes for numerical integration. In addition, introducing the mass and density in Eq. (3.43) makes the SPH method particularly suitable for fluid dynamic problems since density is a crucial variable.

3.3.3 SPH formulations

Based on the above mentioned integral approximation and particle approximation, the SPH formulations can be obtained by interpolating from a set of neighbouring particles. A function f of an arbitrary particle i can be approximated by the direct summation of the quantities of its neighbouring particles$j$ as follows

$$f_i = \sum_{j=1}^{N} \frac{m_j}{\rho_j} f_j W \tag{3.31}$$

where N is the total number of neighbouring particles within the support domain of particle i; the smoothing function $W = (r_{ij}, h)$ is writing as W.

A straightforward way of deriving the derivative of function f is given by

$$\nabla f_i = -\sum_{j=1}^{N} \frac{m_j}{\rho_j} f_j \nabla W \tag{3.32}$$

where the derivatives of the smoothing function ∇W can be obtained using the chain rule.

The second-order derivative of the weight function gives:

$$\nabla W_{ab} = \frac{\partial W}{\partial r} \frac{\boldsymbol{x}_a - \boldsymbol{x}_b}{|\boldsymbol{x}_a - \boldsymbol{x}_b|} \tag{3.33}$$

where $q = \frac{r}{h}$ with $r = |\boldsymbol{x}_a - \boldsymbol{x}_b|$ being the distance between the interpolating particle b and the concerning particle a.

It should be noted such discretization of derivatives is too crude in practical modelling cases, especially for the second derivatives. Wang et al. (2016) summarized existing discretization techniques used in SPH with good features.

Chapter 4: An improved impermeable solid boundary scheme for meshless Local Petrov-Galerkin method

4.1 Introduction

The way by which the impermeable solid boundary condition is implemented can significantly affect the accuracy of the results and computational cost. The solid boundary treatment method, which plays a significant role in flow-structure interaction, remains less developed compared to that for fluid particles, either requiring artificial terms or having a lower accuracy.

So far, several boundary treatment approaches have been developed for the SPH method, including the repulsive force approach (Monaghan, 1994; Monaghan & Kajtar, 2009; Shadloo & Yildiz, 2011; Monaghan & Mériaux, 2018), the ghost or image particle approach (Morris et al., 1997; Liu et al. 2012; Bierbrauer et al., 2009), the dynamic particle approach (Liu & Liu, 2003; Gómez-Gesteira & Dalrymple, 2004; Gong et al., 2009) and the semi-analytical approach, which redefines the solid boundary by edge particles (Kulasegaram et al., 2004). As an alternative to the SPH method, another type of meshless method based on the Galerkin formulation, i.e., the meshless local Petrov-Galerkin (MLPG) method, has also been developed and widely applied. Unlike the SPH method that directly discretizes the strong form of the PPE, this method integrates over a local subdomain, which reduces the order of the pressure derivative in the PPE (Ma, 2005a). Although MLPG has many similarities with SPH or MPS regarding gradient

estimation, projection scheme or free surface identification etc., the implementation of wall boundary conditions remains different in MLPG, as indicated by Sriram & Ma (2021).

According to Ma (2005a), solid boundary treatment approaches in MLPG were initially based on the weak formulation of flow governing equations over the incomplete sub-domains of the boundary particles but were only applied to solve the potential flow (Atluri & Zhu, 1998) and inviscid flow with artificial stabilizing term to suppress spurious pressure (Lin & Atluri, 2001). When the MLPG method was extended to simulate non-linear waves (Ma, 2005a), the wall boundary condition was imposed by direct discretization of the pressure Neumann boundary condition instead of its weak formulation. This wall boundary treatment approach excludes artificial stabilizing terms and prevents fluid particles from penetrating the wall with flow viscosity considered. Three schemes for directly discretising the Neumann boundary condition were compared in Zhou et al. (2008), including two in MPS with single and three layers of boundary particles (Koshizuka & Oka, 1996; Hibi & Yabushta, 2004; Zhang et al., 2006) and one in MLPG based on simplified finite-difference interpolation (SFDI) (Ma, 2008). It was found that SFDI enabled more stable and accurate simulations. However, such an approach does not have a consistent weak formulation throughout the simulation domain. The flow governing equation near the boundary was not implemented at the particle distance scale. MLPG method was further improved by introducing the Rankine source solution (MLPG_R), instead of the Heaviside step function, as the test function for the fluid particles, in which the pressure derivative was entirely replaced by the pressure itself to be numerically solved (Ma, 2005b). The weak formulation for inner fluid particles in the MLPG_R improves the stability and accuracy in solving the

PPE by entirely omitting Laplacian or gradient operator of the unknown pressure (Ma et al., 2016) and was successfully applied to problems such as 2D breaking waves (Ma & Zhou, 2009) and violent water waves (Zheng et al., 2014). As the treatment of wall boundary condition was unchanged with the gradient operator of the pressure being discretized directly, the errors introduced at the boundary can creep into the inner flow domain, especially in regions close to the solid walls.

In this chapter, using the local integration scheme of the MLPG_R method, a weak formulation for the wall boundary condition is developed, and it has a consistent weak formulation throughout the simulation domain for both fluid and boundary particles. The proposed boundary scheme can satisfy simultaneously the incompressible fluid governing equation in the local integration domain and the pressure Neumann boundary condition. The pressure gradient is eliminated for wall particles, leaving only the unknown pressure itself to be numerically discretized. The new formulation has been validated by the analytical solution of the patch test with particles randomly distributed, numerical benchmarks of lid-driven cavity cases at various Reynolds numbers and monochronic waves. Validation on the curved boundary will also be carried out for flow over a cylinder in which pressure acting on the cylinder and wakes after the cylinder will be discussed.

4.2. Governing equations

The governing equations are the incompressible and viscous Navier–Stokes equations in the Lagrangian form as follows:

$$\nabla \cdot \boldsymbol{u} = 0 \tag{4.1}$$

$$\frac{D\boldsymbol{u}}{Dt} = -\frac{1}{\rho}\nabla p + \boldsymbol{g} + v\nabla^2 \boldsymbol{u} \tag{4.2}$$

where ρ is the density, which is a constant for the incompressible fluid, $\boldsymbol{u}$ is the velocity, $\boldsymbol{g}$ is the gravitational acceleration, p is the pressure, and v is the kinematic viscosity.

At the wall boundary, the impermeability condition is applied by enforcing the normal component of the fluid velocity equal to that of the boundary velocity as

$$\boldsymbol{u} \cdot \boldsymbol{n} = \boldsymbol{U} \cdot \boldsymbol{n} \tag{4.3}$$

By substituting Eq. (4.3) into Eq. (4.2), the pressure at the wall satisfies

$$\boldsymbol{n} \cdot \nabla p = \rho\left(\boldsymbol{n} \cdot \boldsymbol{g} - \boldsymbol{n} \cdot \dot{\boldsymbol{U}} + v\boldsymbol{n} \cdot \nabla^2 \boldsymbol{u}\right) \tag{4.4}$$

where $\boldsymbol{U}$ and $\dot{\boldsymbol{U}}$ are the velocity and the acceleration of the solid wall particles, respectively.

4.3 Numerical method

4.3.1 Modelling procedure

In this work, the projection-based scheme is employed to solve the pressure Poisson equation.

(1) Explicitly find out the intermediate velocity $\boldsymbol{u}^*$ and position $\boldsymbol{r}^*$ using

$$\boldsymbol{u}^* = \boldsymbol{u}^n + (v\nabla^2\boldsymbol{u}^n + \boldsymbol{g})\Delta t \tag{4.5}$$

$$\boldsymbol{r}^* = \boldsymbol{r}^n + \boldsymbol{u}^*\Delta t \tag{4.6}$$

(2) Implicitly evaluate pressure p^{n+1} from the pressure Poisson equation Eq. (4.7) by taking the artificial coefficient to zero

$$\nabla^2 p^{n+1} = \frac{\rho}{\Delta t}\nabla \cdot \boldsymbol{u}^* \tag{4.7}$$

(3) Update velocity $\boldsymbol{u}^{n+1}$ and position $\boldsymbol{r}^{n+1}$ at the next step

$$\boldsymbol{u}^{n+1} = \boldsymbol{u}^* + \left(-\frac{1}{\rho}\nabla p^{n+1}\right)\Delta t \tag{4.8}$$

$$\boldsymbol{r}^{n+1} = \boldsymbol{r}^n + \boldsymbol{u}^{n+1}\Delta t \tag{4.9}$$

where $\boldsymbol{u}$ is the fluid velocity vector, $\boldsymbol{r}$ is the position vector, ρ is the fluid density, p is the fluid pressure, $\boldsymbol{g}$ is the gravitational acceleration, and v is the kinematic viscosity of the fluid, Δt is the time step, the superscripts n represents the n^{th} time step and notion * represents the intermediate time step.

4.3.2 MLPG_R formulation for fluid particles

For fluid particles, such as nodes **I** and **J,** as demonstrated in Fig. 4.1(a), the weak formulation for numerical discretization involves the integration of PPE over local subdomains as

$$\int_{\Omega_I} \left(\nabla^2 p^{n+1} - \frac{\rho}{\Delta t} \nabla \cdot \boldsymbol{u}^* \right) \varphi \, d\Omega = 0 \qquad (4.10)$$

where φ is the test function and Ω_I is the integration sub-domain that can be of any arbitrary shape (Atluri & Shen, 2002). In the developed MLPG_R method (Ma, 2005b), the circular sub-domain with a radius of $R_I = 0.8 \times \Delta l$ is adopted, where Δl is the initial particle distance.

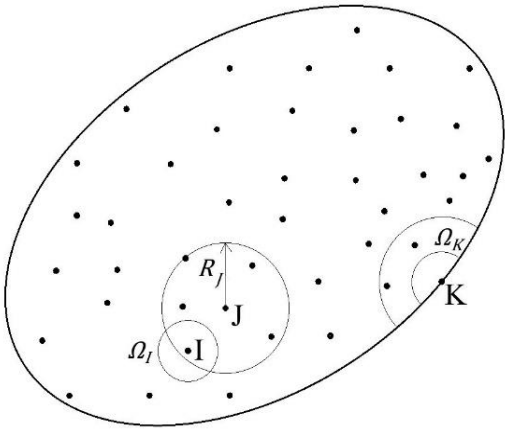

(a)

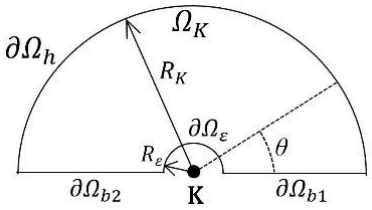

(b) $\partial\Omega_K = \partial\Omega_h \cup \partial\Omega_b \cup \partial\Omega_\varepsilon$

Figure 4.1. (a) Local sub-domain Ω_I for fluid particles I, support domain for fluid particle J with a radius of R_J and two domains for wall boundary particle K. (b) Demonstration of sub-domain for the wall boundary particle K, which is a semi-circle with the centre semi-circle Ω_ε, having the radius of R_ε, being taken out.

The 2D Rankine source solution (i.e., the test function) adopted here is

$$\varphi = \frac{1}{2\pi}\ln\left(\frac{r}{R_I}\right) \tag{4.11}$$

where *r* is the distance away from particle I, since the weak formulation is only applied on fluid particles, the integration sub-domain is entirely located in the fluid domain forming a complete circle. The test function φ satisfies $\nabla^2\varphi = 0$ in Ω_I and $\varphi = 0$ on its circular boundary of $\partial\Omega_I$.

By applying Gauss's theorem to Eq. (4.10), the final weak formulation for fluid particles yields:

$$\int_{\partial\Omega_I} \boldsymbol{n}\cdot(p\nabla\varphi)\,dS - p = \int_{\Omega_I}\frac{\rho}{\Delta t}\boldsymbol{u}^*\cdot\nabla\varphi\,d\Omega \tag{4.12}$$

where $\partial\Omega_I$ is the boundary of Ω_I which is a complete circular curve, and $\boldsymbol{n}$ is the normal vector of the subdomain pointing to the outside.

4.3.3 MLPG_R formulation for wall particles

In this work, instead of direct discretization of the impermeable wall boundary condition involving normal pressure gradient as in the previous MLPG_R method (Ma, 2005b), a new weak formulation will be derived for wall particles based on the PPE with impermeability condition of Eq. (4.3) imposed. As shown in Fig. 4.1(b), the sub-domain for the wall particle, K, is a semi-circle. By adopting the same test function as for the fluid particles, a zero term $p\nabla^2\varphi$ is added to the left-hand side of the PPE and then integrated over the sub-domain Ω_K. To apply Gauss's theory and to avoid the singularity of the test function at the centre of the sub-domain, a semi-circle with a radius being R_ε is extracted from the sub-domain and the integration becomes

$$\int_{\Omega_K} [(\nabla^2 p)\varphi - p\nabla^2\varphi]\, d\Omega = \int_{\partial\Omega_K} [\boldsymbol{n}\cdot(\varphi\nabla p) - \boldsymbol{n}\cdot(p\nabla\varphi)]\, dS \qquad (4.13)$$

where $\partial\Omega_K$ is the boundary of the sub-domain consisting of a semi-circular boundary $\partial\Omega_h$, a flat boundary $\partial\Omega_b = \partial\Omega_{b1} \cup \partial\Omega_{b2}$ representing the wall boundary, and a semi-circular boundary $\partial\Omega_\varepsilon$ for avoiding the singularity at the centre, which will be taken as infinitesimal in the following derivation.

By taking $R_\varepsilon \to 0$, the first term of the right-hand side of Eq. (4.13), can be expressed as

$$\int_{\partial\Omega_h+\partial\Omega_b+\partial\Omega_\varepsilon} [\boldsymbol{n}\cdot(\varphi\nabla p)]\,dS = \int_{\partial\Omega_b} [\boldsymbol{n}\cdot(\varphi\nabla p)]\,dS \qquad (4.14)$$

as it can be easily proven that

$\int_{\partial\Omega_h}[\boldsymbol{n}\cdot(\varphi\nabla p)]\,dS = 0$ as φ vanishes on $\partial\Omega_h$ and

$\int_{\partial\Omega_\varepsilon}(\boldsymbol{n}\cdot\nabla p)\frac{1}{2\pi}\ln\left(\frac{r}{R_K}\right)dS = \int_0^{\boldsymbol{\pi}}(\boldsymbol{n}\cdot\nabla p)\frac{1}{2\pi}\ln\left(\frac{R_\varepsilon}{R_K}\right)R_\varepsilon\,d\theta = 0$

as $\lim_{R_\varepsilon\to 0} ln\left(\frac{R_\varepsilon}{R_K}\right)R_\varepsilon = 0$

The second term can be manipulated to become

$$\int_{\partial\Omega_h+\partial\Omega_b+\partial\Omega_\varepsilon} [\boldsymbol{n}\cdot(p\nabla\varphi)]\,dS = \int_{\partial\Omega_h} [\boldsymbol{n}\cdot(p\nabla\varphi)]\,dS - \frac{p}{2} \qquad (4.15)$$

as $\int_{\partial\Omega_\varepsilon}\boldsymbol{n}\cdot(p\nabla\varphi)\,dS = -\frac{p}{2}$ and $\int_{\partial\Omega_b}[\boldsymbol{n}\cdot(p\nabla\varphi)]\,dS = 0$

Combining Eqs. (4.14) and (4.15) gives the weak formulation of the Laplacian pressure as

$$\int_{\Omega_K}(\nabla^2 p)\varphi\,d\Omega = \int_{\partial\Omega_b}\boldsymbol{n}\cdot(\varphi\nabla p)\,dS + \frac{p}{2} - \int_{\partial\Omega_h}[\boldsymbol{n}\cdot(p\nabla\varphi)]\,dS \qquad (4.16)$$

Gauss theory is also applied to the integration of the term associated with the divergence of the intermediate velocity, and it reads

$$\int_{\Omega_K} \frac{\rho}{\Delta t} \varphi (\nabla \cdot \boldsymbol{u}^*)\, d\Omega = \int_{\Omega_K} \frac{\rho}{\Delta t} \nabla \cdot (\varphi \boldsymbol{u}^*)\, d\Omega - \int_{\Omega_K} \frac{\rho}{\Delta t} \boldsymbol{u}^* \cdot \nabla \varphi \, d\Omega$$
$$= \int_{\partial \Omega_b} \frac{\rho}{\Delta t} \boldsymbol{n} \cdot (\varphi \boldsymbol{u}^*) dS - \int_{\Omega_K} \frac{\rho}{\Delta t} \boldsymbol{u}^* \cdot \nabla \varphi \, d\Omega \qquad (4.17)$$

in which the integration over the subdomain boundary $\partial\Omega_K$ is reduced to $\partial\Omega_b$ as it can be easily proven that $\int_{\partial\Omega_h} \frac{\rho}{\Delta t} \boldsymbol{n} \cdot (\varphi \boldsymbol{u}^*) dS = 0$ and $\int_{\partial\Omega_\varepsilon} \frac{\rho}{\Delta t} \boldsymbol{n} \cdot (\varphi \boldsymbol{u}^*) dS = 0$.

Combining Eqs. (4.16) and (4.17), the final weak formulation for the wall boundary particles is expressed as

$$\int_{\partial \Omega_b} \boldsymbol{n} \cdot (\varphi \nabla p)\, dS + \frac{p}{2} - \int_{\partial \Omega_h} [\boldsymbol{n} \cdot (p \nabla \varphi)]\, dS$$
$$= \int_{\partial \Omega_b} \frac{\rho}{\Delta t} \boldsymbol{n} \cdot (\varphi \boldsymbol{u}^*) dS - \int_{\Omega_K} \frac{\rho}{\Delta t} \boldsymbol{u}^* \cdot \nabla \varphi \, d\Omega \qquad (4.18)$$

In Eq. (4.18), the first terms at the left- and right-hand sides are integrals over the boundary $\partial\Omega_b$, where the pressure Neumann condition satisfies. Thus Eq. (4.4) in the format of $\boldsymbol{n} \cdot \nabla p = \frac{\rho}{\Delta t} \boldsymbol{n} \cdot (\boldsymbol{u}^* - \boldsymbol{U})$ (Ma & Zhou, 2009) is implemented, and the two terms involving pressure gradient and

intermediate velocity vanish. The final formulation for the wall boundary particles yields

$$\int_{\partial\Omega_h} [\boldsymbol{n} \cdot (p\nabla\varphi)]\, dS - \frac{p}{2} = \int_{\Omega_K} \frac{\rho}{\Delta t} \boldsymbol{u}^* \cdot \nabla\varphi \, d\Omega - \int_{\partial\Omega_b} \frac{\rho}{\Delta t} \boldsymbol{n} \cdot (\varphi \boldsymbol{U}) dS \qquad (4.19)$$

For the scenarios that only involve fixed or tangentially moving boundaries, i.e., $\boldsymbol{n} \cdot \boldsymbol{U} = 0$, Eq. (4.19) can be further simplified as

$$\int_{\partial\Omega_h} [\boldsymbol{n} \cdot (p\nabla\varphi)]\, dS - \frac{p}{2} = \int_{\Omega_K} \frac{\rho}{\Delta t} \boldsymbol{u}^* \cdot \nabla\varphi \, d\Omega \qquad (4.20)$$

This new formulation for wall particles satisfies the PPE in the local sub-domain and has the impermeable wall boundary condition implemented for both fixed and moving walls. Furthermore, because all terms involving derivatives of the unknown pressure are removed, the accuracy and efficiency of solving for pressure at the wall boundary can be much improved as it has been approved for fluid particles (Ma, 2005a, b). A complete MLPG_R formulations for wall particles can be found in Appendix A.

It should be noted that the semi-circular sub-domain used in the derivation assumes that the wall boundary truncating the sub-domain is a straight line and is the diameter of the sub-domain. This can be justified by the fact that

the size of the sub-domain is small with the same scale of the particle distance, and the error induced by the assumption, when applied to curved boundaries, can be reduced by increasing the number of particles on the boundary. Simulations of flow over a cylinder will be presented in Section 4.5.3, in which the proposed scheme will be applied on the curved wall boundary with various particle distances tested.

4.3.4 Discretized equations

For both fluid and wall particles governed by the weak formulations of Eqs. (4.12) and (4.19), respectively, the unknown pressure will be approximated by a set of neighbouring particles and discretized as

$$p(\boldsymbol{x_i}) \approx \sum_{j=1}^{N} \Phi_j(\boldsymbol{x})\, \hat{p}_j \tag{4.21}$$

where Φ_j is the interpolation function in terms of neighbour particle j, which is located within the support domain of particle i and will be formulated by the first-order Moving Least Square (MLS) method in this paper, which is detailed in Belytschko et al. (1994) and Atluri et al. (1999), N is the total number of neighbour particles affecting the pressure at $\boldsymbol{x}$, and $\hat{p}_j$ is the pressure of each neighbour particle.

In this work, the size of the supporting domain is chosen to be $1.85 \times \Delta l$ as it was taken in the MLPG_R method (Ma, 2005b), where Δl is the initial particle distance. The linear equation set for pressures of all the particles with the total number of n, $\boldsymbol{P} = [p_1, p_2, \dots p_n]$, is written as

$$\boldsymbol{SK} \cdot \boldsymbol{P} = \boldsymbol{FB} \tag{4.22}$$

where

$$\boldsymbol{SK}_{ij} = \begin{cases} \int_{\partial\Omega_I} \Phi_j(\boldsymbol{x}_i)\boldsymbol{n} \cdot \nabla\varphi \, dS - \Phi_j(\boldsymbol{x}_i) & \text{fluid particles} \\ \int_{\partial\Omega_h} \Phi_j(\boldsymbol{x}_i)\boldsymbol{n} \cdot (\nabla\varphi) \, dS - \dfrac{\Phi_j(\boldsymbol{x}_i)}{2} & \text{wall particles} \end{cases} \tag{4.23}$$

and

$$\boldsymbol{FB}_i = \begin{cases} \int_{\Omega_I} \dfrac{\rho}{\Delta t}\boldsymbol{u}^* \cdot \nabla\varphi \, d\Omega & \text{fluid particles} \\ \int_{\Omega_K} \dfrac{\rho}{\Delta t}\boldsymbol{u}^* \cdot \nabla\varphi \, d\Omega - \int_{\partial\Omega_b} \dfrac{\rho}{\Delta t}\boldsymbol{n} \cdot (\varphi \boldsymbol{U}) dS & \text{wall particles} \end{cases} \tag{4.24}$$

By keeping the same formulation for the fluid particles, the direct discretization of the wall boundary condition, as in Ma & Zhou (2009), is presented in Eqs. (4.25) and (4.26) for comparison, which shows that the newly developed weak formulation removes the gradient approximation for

the unknown pressure. The derivation process also fulfils the mass and momentum conservation and the impermeable wall condition.

$$\boldsymbol{SK}_{ij} = \boldsymbol{n} \cdot \nabla \Phi_j(\boldsymbol{x}_i) \tag{4.25}$$

$$\boldsymbol{FB}_i = \frac{\rho}{\Delta t} \boldsymbol{n} \cdot (\boldsymbol{u}^* - \boldsymbol{U}) \tag{4.26}$$

In Eq. (4.23), for terms involving line integration over $\partial\Omega_I$ and $\partial\Omega_h$ for fluid and boundary particles, respectively, Gaussian quadrature is adopted for each quarter segment of the circular integration surface using two Gaussian points (Ma, 2005b). Domain integration of explicitly calculated intermediate velocity will be carried out for fluid and wall particles. As for the intermediate velocity calculation in Eq. (4.5), the viscous term involving velocity Laplacian is obtained by the second-order MLS method. Alternative Laplacian operators such as QSFDI and CSPM are discussed in Korzilius et al. (2016), Yan et al. (2020) and Zhang et al. (2021).

4.3.5 Numerical approach for domain integration

As can be seen from the discretized equations Eqs. (4.23) and (4.24), the domain integration of intermediate velocity requires to be evaluated for the code implementation. There are several numerical techniques involving the integral evaluation, like the classic Gaussian quadrature method or the semi-analytical method (Atluri et al., 1999; Sellountos & Polyzos, 2003; Ma, 2005b). According to Ma (2005b), the Gaussian quadrature method, which

is usually stated as a summation of function values at specific points within the integration domain, is relatively time-consuming due to the required number of specified Gaussian points. For example, Ma (2005b) figured out that at least 16 Gaussian points are needed for a 2D simulation case to achieve satisfactory results.

In this work, the semi-analytical method, introduced by Ma (2005b), is employed for evaluating the intermediate velocities in the current study with higher computational efficiency. The main features of the semi-analytical method are to divide the domain of integration (e.g., a circular domain for inner fluid particles or a semi-circular domain for wall boundary particles) into several parts (i.e., quarters of subdomains) and assume that the field values (e.g., intermediate velocities) have a linear variation over the integration domain; then, analytically perform the integration over subdomains. It is worth mentioning that a more efficient integration technique was developed for 3D simulation with only 6 points needed and quantified the order of the error (Agarwal et al., 2021, Sriram and Ma, 2021). In this study, the domain integration technique follows that proposed in Ma (2005b), dividing the domain into four divisions and requiring 4 points in total, which is sufficiently efficient for 2D simulations.

As discussed in 4.3.2 and 4.3.3, the domain integration for fluid particles is over a complete circle while it is over a semi-circle for a single layer of the wall particles. Once Eq. (4.22) is solved and the pressure field is obtained, velocity and particle position updates will be explicitly carried out according to Eq. (4.8) and (4.9) with the SFDI scheme (Ma, 2008) adopted for pressure gradient estimation. In this section, the semi-analytical method for

evaluating intermediate velocities for inner fluid particles will be demonstrated, and the same approach can also be applied to wall particles.

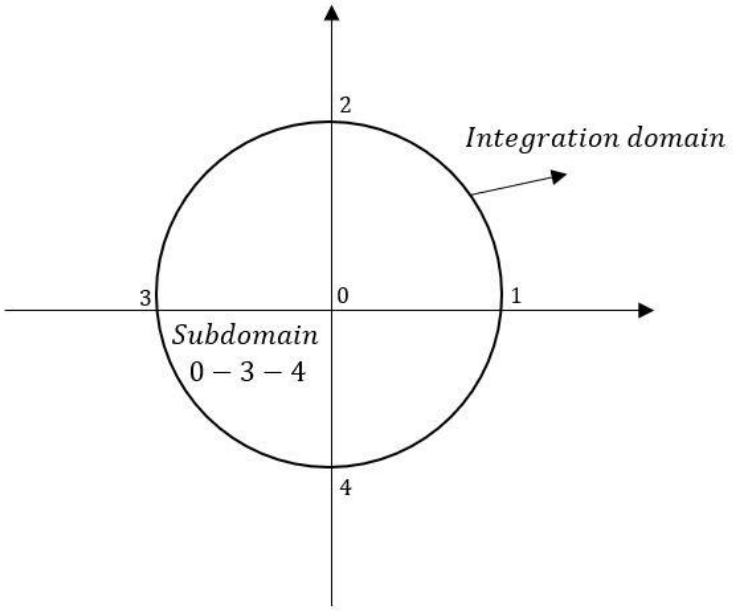

Figure 4.2. Illustration of a circular integration domain with four divisions (i.e., subdomains).

As shown in Fig. 4.2, a circular integration domain for an inner fluid particle is divided into four subdomains, i.e., quarter 0-1-2, 0-2-3, 0-3-4 and 0-4-1. Based on the linear variation assumption, the intermediate velocity components can be expressed as:

$$u = u_0 + c_{ux}\frac{(x - x_0)}{R_I} + c_{uy}\frac{(y - y_0)}{R_I} \tag{4.27}$$

$$v = v_0 + c_{vx}\frac{(x - x_0)}{R_I} + c_{vy}\frac{(y - y_0)}{R_I} \tag{4.28}$$

where R_I is the radius of the circular integration domain; u, v are the intermediate velocity components at a random point with a position vector (x, y) within the integration domain; u_0, v_0 are the intermediate velocity components at the centre of the integration domain with position vector (x_0, y_0); and c_{ux}, c_{vx}, c_{uy}, c_{vy} are coefficient defined by the intermediate velocity components at specific points 1, 2, 3 or 4.

Using x – direction velocity component u within the quarter 0-1-2 as an example gives:

$$c_{ux}(x_1 - x_0) + c_{uy}(y_1 - y_0) = (u_1 - u_0)R_I \tag{4.29}$$

$$c_{ux}(x_2 - x_0) + c_{uy}(y_2 - y_0) = (u_2 - u_0)R_I \tag{4.30}$$

And combining Eqs. (4.29) and (4.30) yields:

$$c_{ux} = \frac{(u_1 - u_0)(y_2 - y_0) - (u_2 - u_0)(y_1 - y_0)}{(x_1 - x_0)(y_1 - y_0) - (x_2 - x_0)(y_2 - y_0)} R_I \tag{4.31}$$

$$c_{uy} = \frac{(u_2 - u_0)(x_1 - x_0) - (u_1 - u_0)(x_2 - x_0)}{(x_1 - x_0)(y_1 - y_0) - (x_2 - x_0)(y_2 - y_0)} R_I \tag{4.32}$$

Another two coefficients c_{vx} and c_{vy} can be obtained in the same way by taking y – direction velocity component v. In brief, the linear relationship at any position within the circular integration domain is estimated based on the velocities at only five specific points (i.e., Point 0, 1, 2, 3 and 4).

In Eq. (4.24), the integral term of intermediate velocity can be written as

$$\int_{\Omega_I} \frac{\rho}{\Delta t} \boldsymbol{u}^* \cdot \nabla \varphi \, d\Omega = \frac{\rho}{2\pi \Delta t} \int_0^{2\pi} \int_0^{R_I} u_r^*(r,\theta) dr d\theta \tag{4.33}$$

According to Eqs. (4.29) to (4.32), the integral term of Eq. (4.33) can be rewritten as:

$$\int_0^{2\pi} \int_0^{R_I} u_r^*(r,\theta) dr d\theta = \sum_i^N \int_{\vartheta_i}^{\vartheta_{i+1}} \int_0^{R_I} u_r^*(r,\theta) dr d\theta \tag{4.34}$$

where N is the number of divisions of integration domains ($N = 4$ for inner fluid particles), and ϑ_i is the identification of specific points which specifies the current integration over a subdomain.

Based on the analytical evaluation using Eqs. (4.27) and (4.28), the intermediate velocity component becomes

$$u = u_0 + c_{ux} r \cos\theta + c_{uy} r \sin\theta \tag{4.35}$$

$$v = v_0 + c_{vx} r \cos\theta + c_{vy} r \sin\theta \tag{4.36}$$

where $(x - x_0)/R_I = r\cos\theta$ and $(y - y_0)/R_I = r\sin\theta$ can be used for the transformation from Cartesian coordinates to polar coordinates.

So

$$u_r^*(r,\theta) = u_0\cos\theta + v_0\sin\theta + c_{ux}r\cos^2\theta + c_{uy}r\cos\theta\sin\theta + c_{vx}r\cos\theta\sin\theta + c_{vy}r\sin^2\theta \quad (4.37)$$

Finally, integrating each term of Eq. (4.37) and the integral term in Eq. (4.24) can be explicitly solved as

$$\int_{\vartheta_1}^{\vartheta_2}\int_0^{R_I} \boldsymbol{u_r^*}(r,\theta)drd\theta = \frac{1}{4}R_I\begin{bmatrix}\left(c_{ux}+c_{vy}\right)(\vartheta_2-\vartheta_1)+\\ \left(c_{ux}-c_{vy}\right)(\sin\vartheta_2\cos\vartheta_2-\sin\vartheta_1\cos\vartheta_1)\\ +\left(c_{uy}+c_{vx}\right)(\sin^2\vartheta_2-\sin^2\vartheta_1)\end{bmatrix} \quad (4.38)$$

It is noted that the results obtained based on four divisions are good enough for 2D simulations (Ma, 2005b), and the requirement of velocities at only five specified points considerably saves the computational time. More recently, Agarwal et al. (2021) figured out that the semi-analytical method used for integral expression is asymmetric and lacks the order of error; therefore, an alternative derivation is provided based on Taylor series expansion with fewer required integration points (i.e., only 6 points for a 3D spherical subdomain) and a leading error term proportional to R_I^4. It is worth to mention that the resultant expression by Agarwal et al. (2021) shows great potential for improving accuracy and extending the current 2D simulations to 3D problems.

4.4 Code implementation of MLPG_R

The code implementation is to convert the numerical procedures into a usable tool for performing various tasks (Liu & Liu, 2003). The current MLPG_R code developed in this work is implemented and tested based on the platform of Microsoft Visual Studio 2015 in the environment of the Intel Fortran compiler for carrying out a series of validating tasks and applications.

Fig. 4.3 shows the main structure of the MLPG_R code, and it is designed to satisfy the basic requirements of executing and validating the proposed boundary scheme following the two-step prediction-correction pressure solving procedure. In general, this code implementation can be divided into three parts. The first one is the initialization sector, which includes subroutines that can input initial values (e.g., density, gravity, viscosity etc.), generate the initial node grid and assign required physical properties to each particle within the computational domain. Then, the main sector within the time loop aims to incorporate basic governing equations into discretized equations and solve the subsequent pressure, velocity, and position of each particle. Finally, the computed results are outputted and stored in external files for analysis and visualization.

This code can be easily extended to other applications by adding or modifying subroutines according to different requirements. Some involved numerical techniques like NNPS (i.e., the nearest neighbouring particle searching scheme) are referred to Fraga Filho et al. (2020).

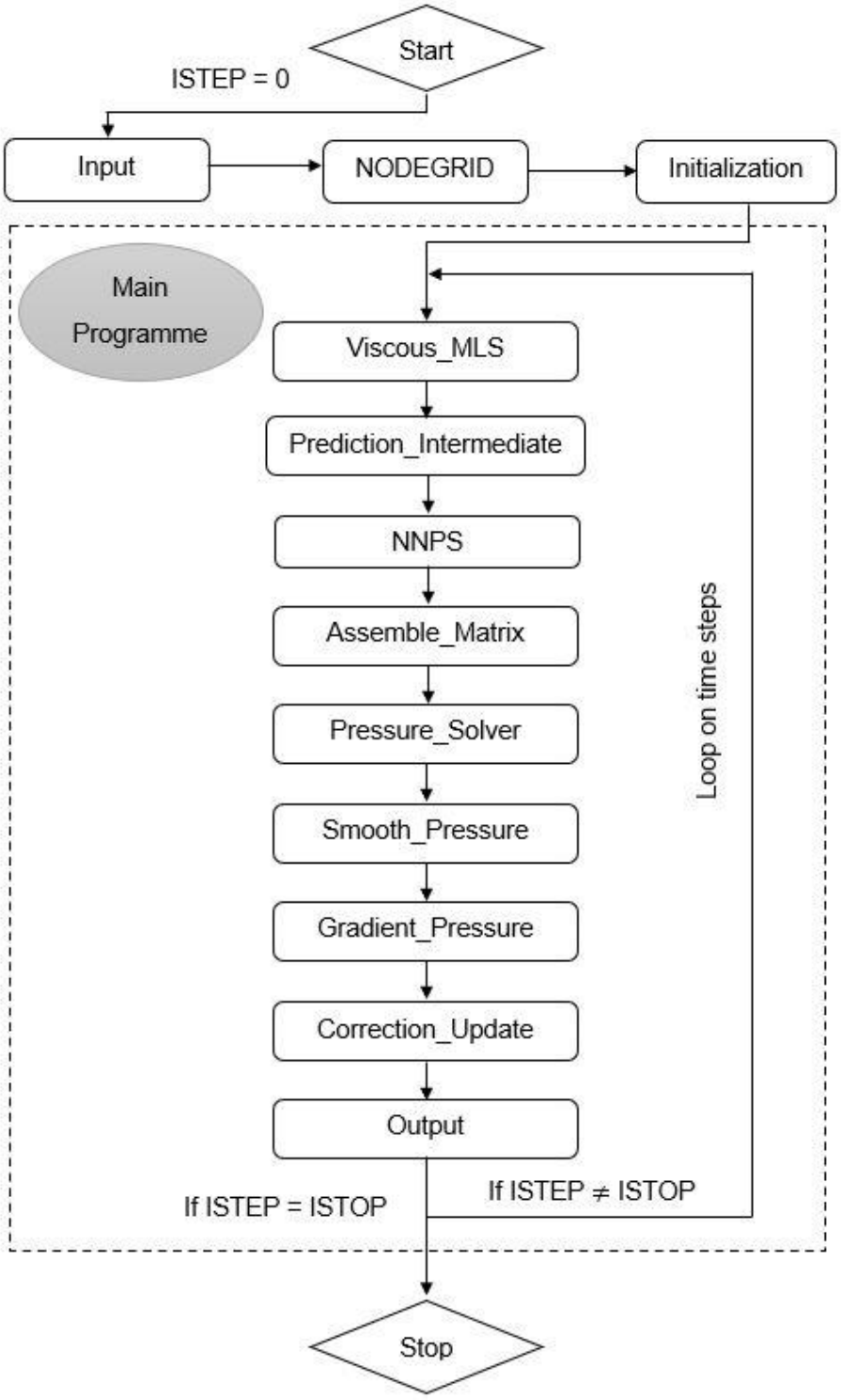

Figure 4.3. Structure of the current MLPG_R code.

4.5 Model validations

In this section, four test cases, namely patch test for solving Poisson's equation, lid-driven cavity, flow over a cylinder and monochromic wave generation, which have analytical solutions, numerical benchmarks and experimental results, are presented to validate the proposed scheme for implementing the boundary condition. The MLPG_R method for modelling fluid particles, without the special boundary treatment approach, is well established in solving linear potential flow problems (Atluri & Zhu, 1998), non-linear water waves (Ma, 2005a), and more recently, contaminant transport problems (Boddula & Eldho, 2017) and wave-vegetation interaction problems (Divya et al., 2020).

4.5.1 Patch tests for solving Poisson's equation

To test the performance of different numerical schemes, patch tests for solving Poisson's equation with comparisons with the analytical solution are widely reported (Schwaiger, 2008; Lind et al., 2012; Zheng et al., 2014). In this study, the equation of $\nabla^2 p = 0$ in the patch of $0 \leq x \leq 1$ and $0 \leq y \leq 1$ will be solved. Four solid boundary conditions are defined as $\frac{\partial p}{\partial x}\Big|_{x=0} = 0$, $\frac{\partial p}{\partial x}\Big|_{x=1} = 0$, $\frac{\partial p}{\partial y}\Big|_{y=0} = 0$ and $\frac{\partial p}{\partial y}\Big|_{y=1} = \pi \sinh(\pi y)\cos(\pi x)$ which leads to the analytical solution of $p(x, y) = \cosh(\pi y)\cos(\pi x)$. The equation is numerically solved by the newly developed boundary condition scheme as well as the existing scheme involving direct discretization of the wall boundary condition (Ma, 2005a) for comparison. A range of particle

distances Δl = 0.007, 0.008, 0.01, 0.0125, 0.01666, 0.025 and 0.05 in both x and y directions are tested, corresponding to total particle numbers of 20736, 15876, 10201, 6561, 3721, 1681 and 441, respectively in the patch. To achieve a particle distribution similar to that in the real flow simulation, controlled randomness is added to regularly distributed particles with the coordinates modified by $\Delta l' = (1 + k(Rn - 0.5))\Delta l$, where Rn is a random number ranging from 0 to 1, and k is a constant for adjusting the disorderliness of the particles. The accuracy is quantified by evaluating the mean error for all particles as $Er = \sqrt{\sum|p_i - p_{i,a}|^2} / \sqrt{\sum|p_{i,a}|^2}$, where p_i is the numerically solved pressure and $p_{i,a}$ is the analytical solution.

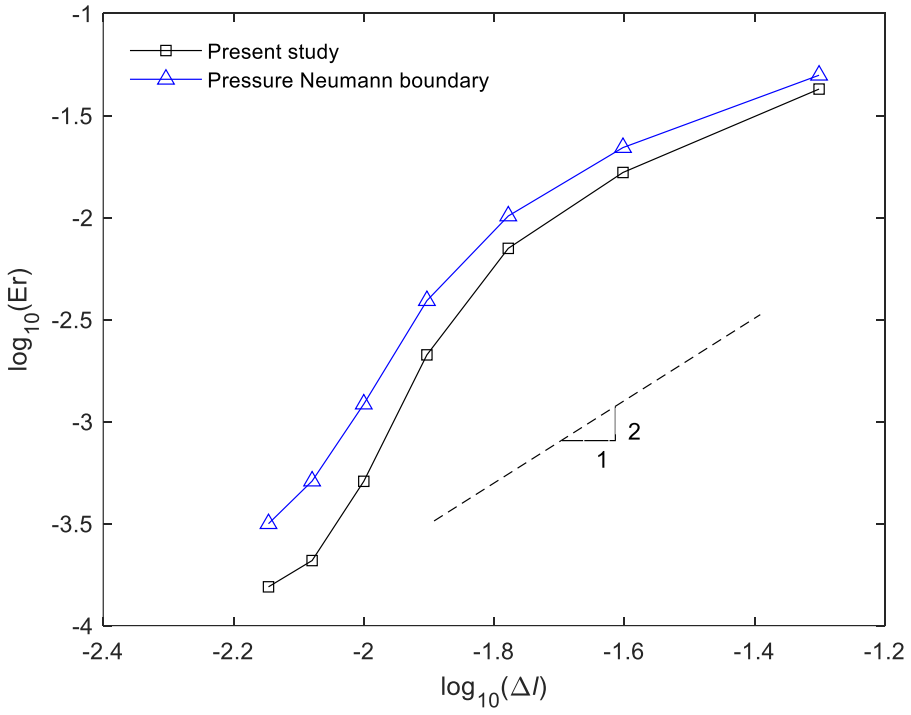

Figure 4.4. Errors of the new boundary scheme and pressure Neumann boundary scheme for different particle distances of Δl =0.007, 0.008, 0.01,

0.0125, 0.01666, 0.025, 0.05 with the randomness of $k = 0.3$. The dashed line is to indicate the 2:1 gradient.

Fig. 4.4 shows the errors of numerical results using the direct discretization of the wall boundary condition by the SFDI scheme (Ma, 2008) and the present weak formulation. It can be seen that with different numbers of particles employed at typical randomness in the simulation $k = 0.3$, the errors of the new boundary scheme are smaller than those with the existing direct discretization scheme. The scheme also achieves overall second-order convergence for particle distance, as shown in Fig. 4.4. When examining wall boundary particles only, the mean error for the particle distance of $\Delta l = 0.01m$ is 6.299×10^{-4} by adopting the new boundary approach, which is lower than 1.729×10^{-3} obtained by the direct discretisation approach. Since the numerical scheme remains the same for all the inner particles, the reduced mean errors, including all the particles as shown in Fig. 4.5, indicate that the improvement on the boundary condition implementation also significantly impacts the equation solving for the inner particles.

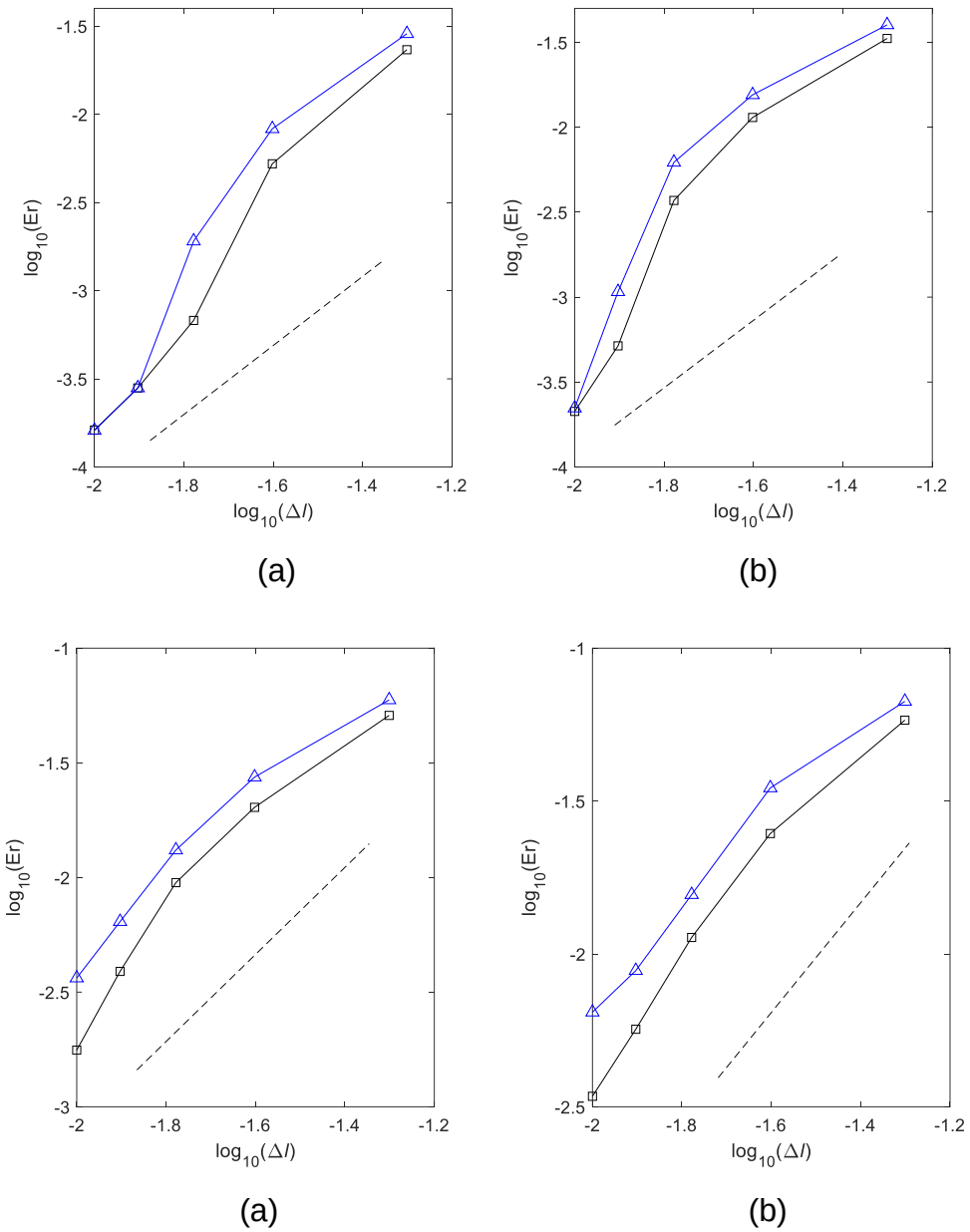

Figure 4.5. Errors of the direct Neumann boundary condition scheme (triangle markers) and the improved weak formulation boundary scheme (square marker) for different particle distances Δl =0.01, 0.0125, 0.01666, 0.025, 0.05 with different randomness in (a) $k = 0.1$, (b) $k = 0.2$, (c) $k = 0.4$ and (d) $k = 0.5$. The dash lines are to indicate the 2:1 gradient.

Further tests for the various particle distributions by ranging randomness k from 0.1 to 0.5 are carried out, and results are compared with the existing scheme as shown in Fig. 4.5. For both schemes, errors slightly increase as the increased disorder is introduced in the distribution of particles, which is consistent with results from other meshless methods (Basic et al., 2018). It also can be seen that the new scheme shows better performance over the full range of randomness and particle distances. For minor disordered particles ($k = 0.1$ and 0.2), the performances of the two schemes are similar, especially when particle distance is sufficiently fine, i.e., $\Delta l = 0.01$, while for higher disordered distribution ($k = 0.4$ and 0.5), the new scheme achieves much higher accuracy.

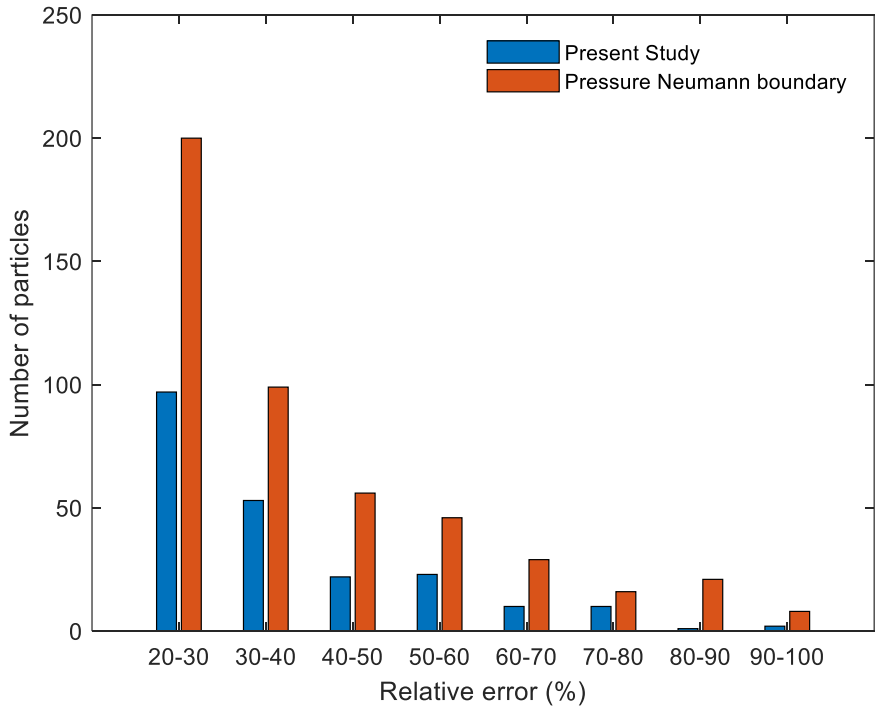

Figure 4.6. The number of particles with an error larger than a certain percentage of maximum error (the blue column for the new scheme and the red column for the existing scheme).

In addition to the mean error, the number of particles having large errors, which may lead to simulation instability, is also investigated. For the case with $\Delta l = 0.01$ and $k = 0.3$, the maximum errors are 1.534×10^{-2} and 2.424×10^{-2} for the new and existing schemes, respectively. Fig. 4.6 shows the number of particles having large errors, which are higher than 20% of the maximum error in the simulation. Those particles are divided into groups with an increment of 10% relative to the maximum error. It can be seen that 97 particles out of 10201 in total have errors between 20% and 30% of the maximum error in the present scheme. While the number is doubled for the existing boundary condition scheme in this error range, and this is the case for all other larger error ranges.

4.5.2 Lid-driven cavity

In this section, the lid-driven cavity flow in a 2D square domain with the length of sides being $L = 1m$ is considered. This case has been used to examine the accuracy and efficiency of other numerical methods, such as the Finite Volume method (Ghia et al., 1982), which will be used as the benchmark. The flow in the rigid wall confined domain is driven by the lid sliding laterally at a constant velocity of $U_{lid} = 1m/s$. The flow regime is classified by the Reynolds number defined as $Re = U_{lid}L/\upsilon$ where ν denotes the kinematic viscosity of the fluid. Re from 100 to 3200 are tested, covering a wide range of the flow regime, which can reach a steady-state (Peng et al., 2003). The convergence test regarding to the particle distance is firstly carried out for Re = 400 with Δl = 0.05m, 0.025m, 0.017m, 0.013m and 0.01m, corresponding to total particle numbers of 21×21, 41×41,

61×61 , 81×81 and 101×101 respectively. Horizontal and vertical velocities at x=L/2 and y=L/2, respectively, are plotted for all the resolutions along with the benchmark results (Ghia et al., 1982), as shown in Fig. 4.7. It can be seen that with the particle number increased, both velocities gradually approach the benchmark with the results from 81×81 well agreed with the benchmark. To ensure the accuracy of the simulations, particle distance $\Delta l = 0.01$ (corresponding to the particle number of 101×101) will be adopted for the following cases unless stated otherwise.

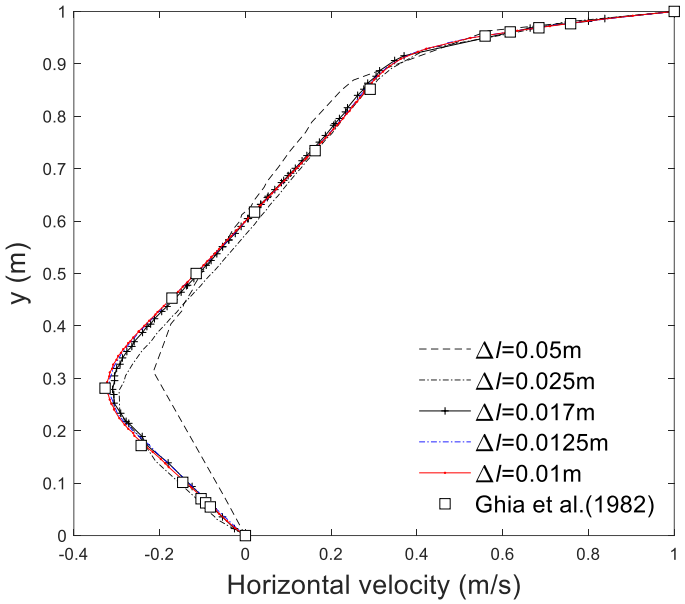

(a)

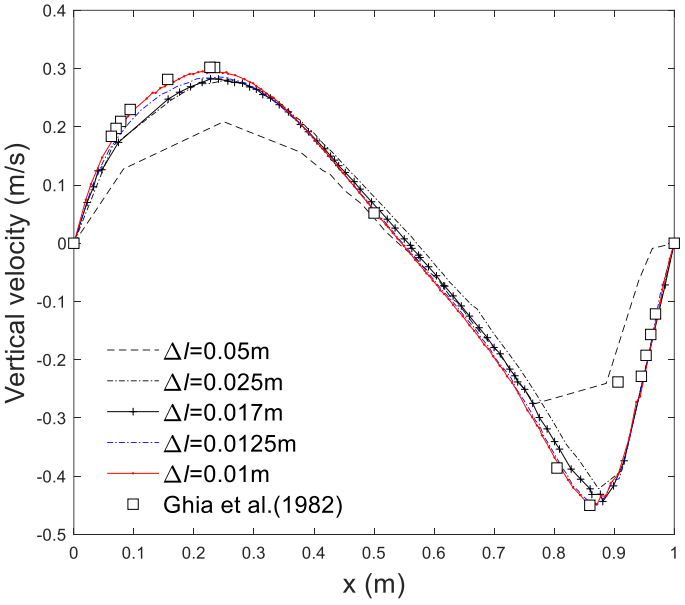

(b)

Figure 4.7. Velocities of lid-driven cavity flow at Re =400 obtained by the MLPG_R method with the new wall boundary scheme using different particle distances and the benchmark. (a) Horizontal velocity at x=L/2 and (b) Vertical velocity at y=L/2.

The velocities for the flows with Re being from 100 to 3200 are plotted and compared with those simulated by the existing boundary condition scheme in Fig. 4.8. The results of the new boundary condition scheme show good agreement with those in Ghia et al. (1982) across the whole range of the Re. Similar performance of both schemes at low $Re = 100$ as demonstrated in Fig. 4.8(a) and (b) is to be expected due to the maximum velocities in flows with lower Re are developed far away from the boundaries, i.e., the magnitude of the horizontal velocity becomes maximum at $y = 0.5m$, and that happens at $x = 0.22m$ and $0.8m$ for the vertical velocity, which is less sensitive to the boundary treatment. When Re is increased, the improvement by the new boundary scheme becomes significant, especially for the maximum velocities which occur closer to the wall boundaries. As for the case of $Re = 1000$, the maximum horizontal velocity occurs at $y = 0.18m$, which is closer to the bottom boundary and that for the vertical velocity occurs at $x = 0.15m$ and 0.9 m which move forward the two sidewalls. One should also note that when the Re is further increased to 3200, although the results are improved from the previous scheme, velocities are slightly underestimated may be caused by the lack of consideration for turbulence which is not the focus of this work.

Figure 4.8. Velocities of the lid-driven cavity flow by adopting the improved wall boundary scheme (black solid line) and the existing wall boundary scheme (dash blue line). (a) to (d) are results of $Re = 100$, 400, 1000 and 3200 with horizontal velocities at $x = L/2$ on the top and vertical velocities at $y = L/2$ on the bottom. The squares are benchmarks from the Finite Volume Method (Ghia et al., 1982).

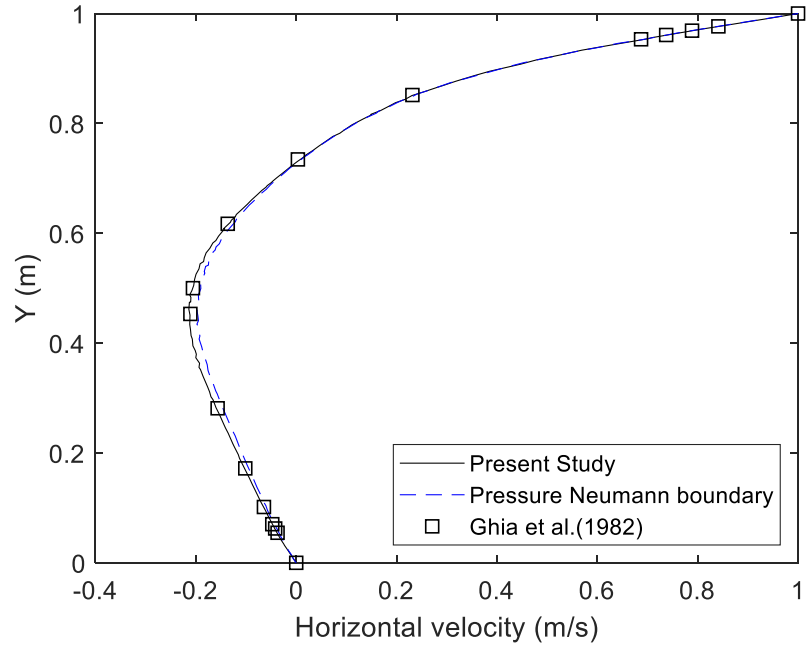

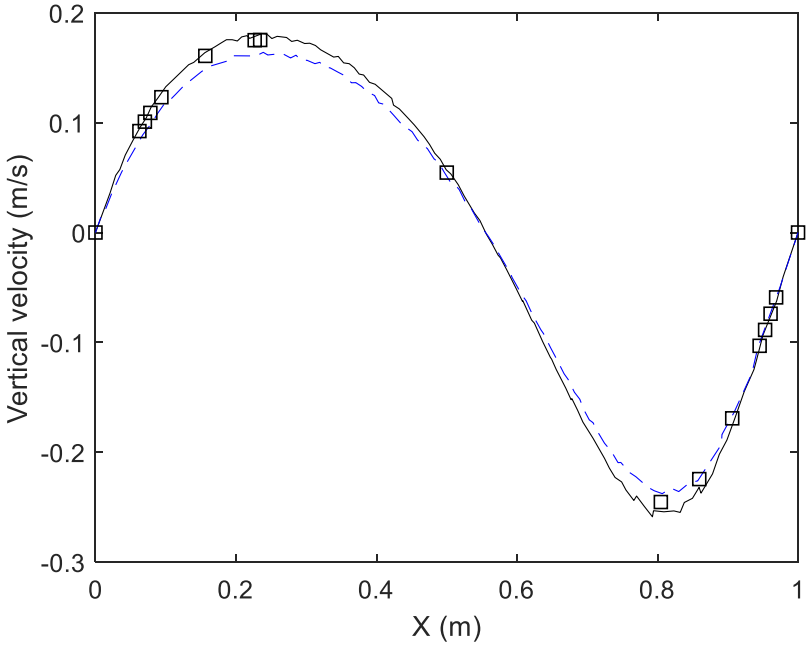

(a) Results of $Re = 100$ with horizontal velocities at $x = L/2$ on the top and vertical velocities at $y = L/2$ on the bottom. The squares are benchmarks from the Finite Volume Method (Ghia et al., 1982).

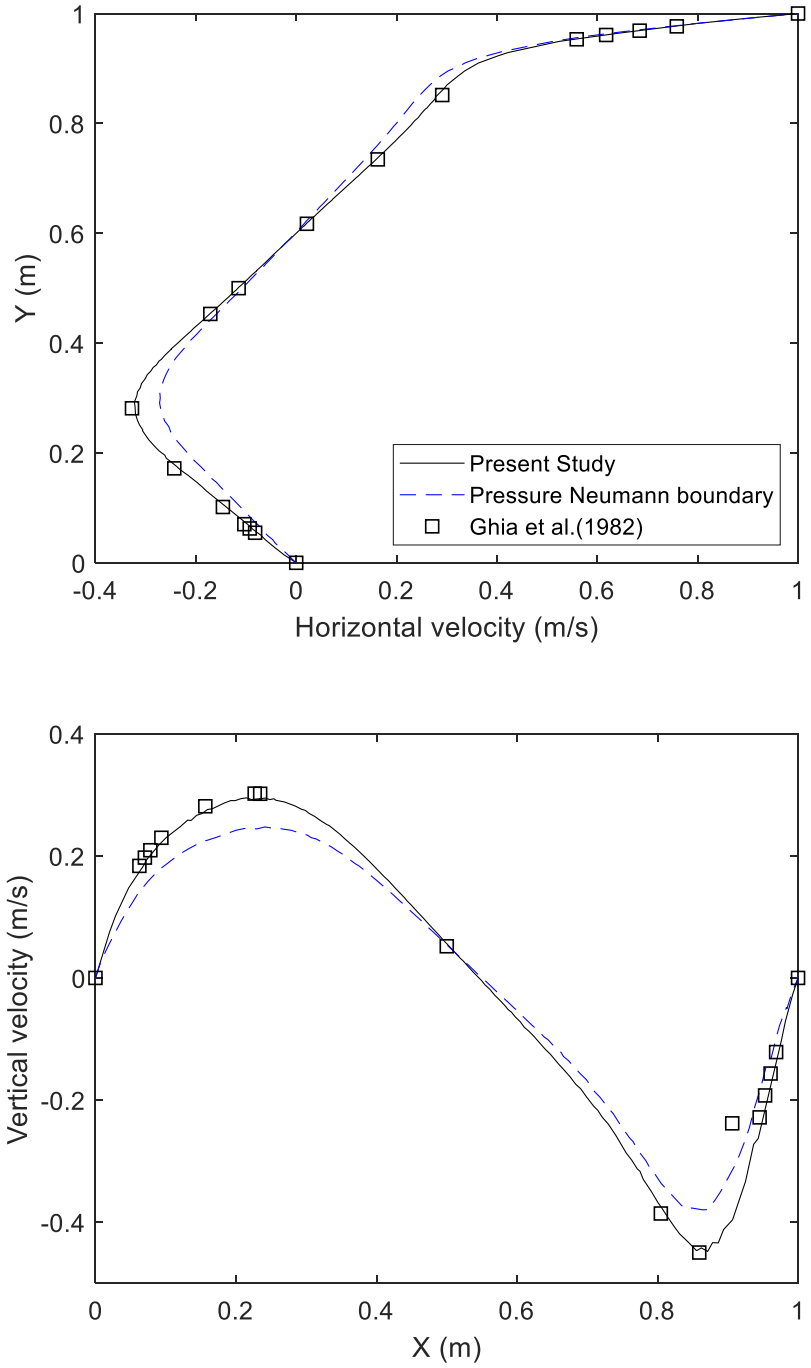

(b) Results of $Re = 400$ with horizontal velocities at $x = L/2$ on the top and vertical velocities at $y = L/2$ on the bottom. The squares are benchmarks from the Finite Volume Method (Ghia et al., 1982).

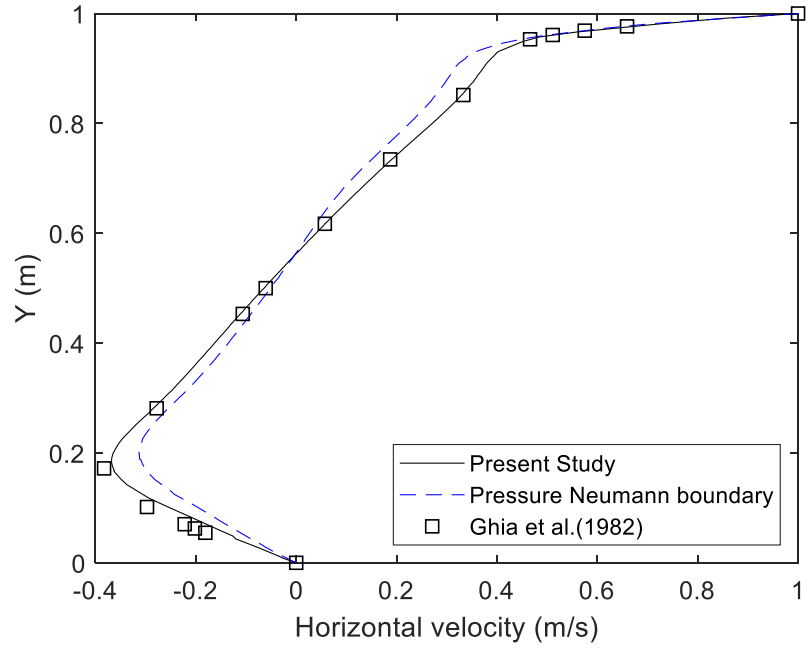

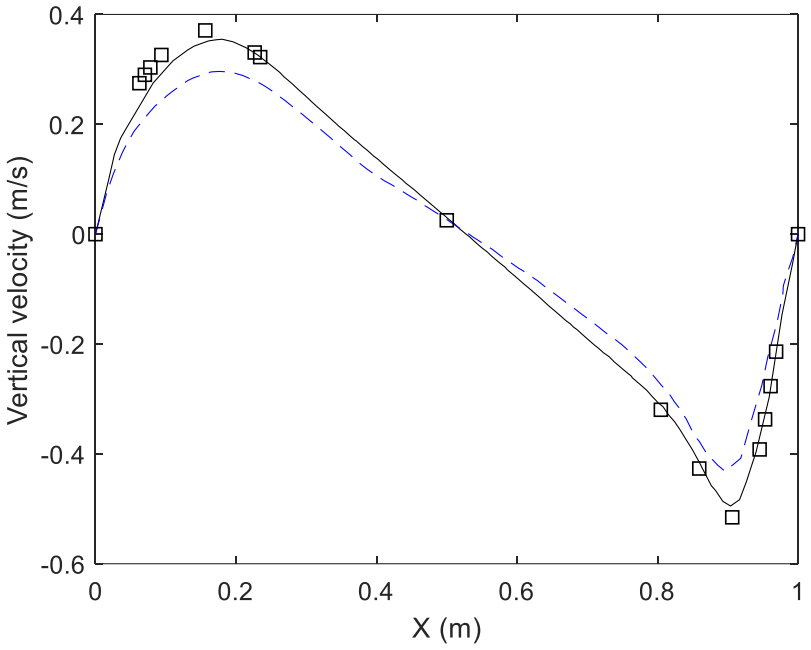

(c) Results of $Re = 1000$ with horizontal velocities at $x = L/2$ on the top and vertical velocities at $y = L/2$ on the bottom. The squares are benchmarks from the Finite Volume Method (Ghia et al., 1982).

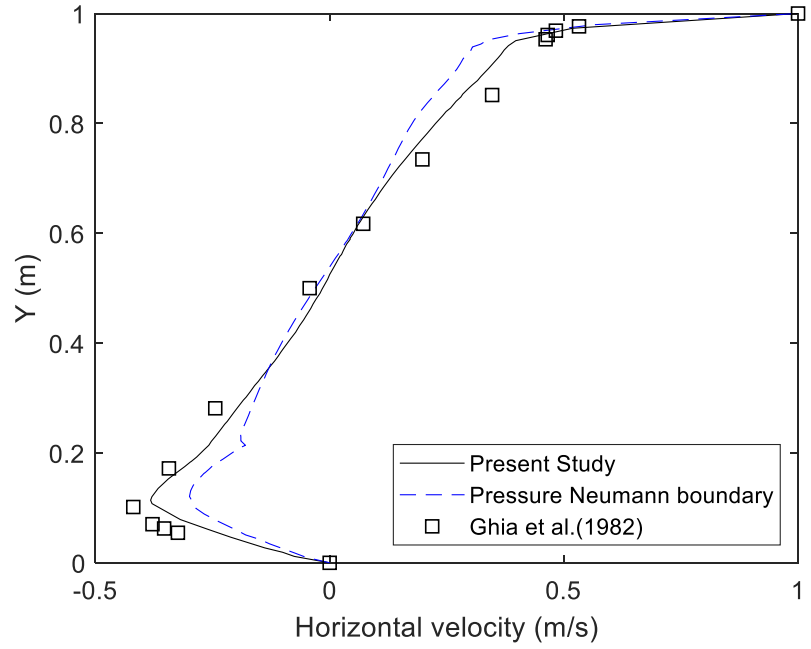

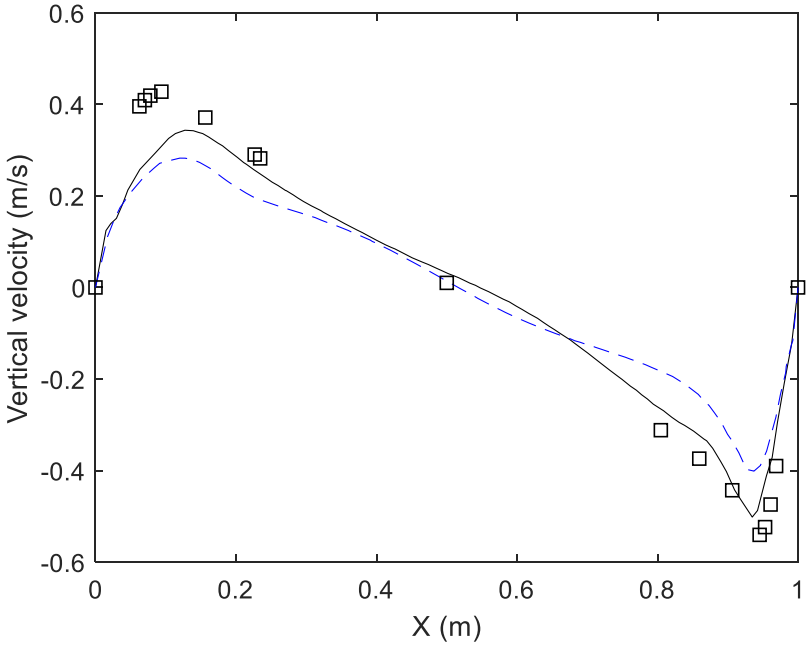

(d) Results of $Re = 3200$ with horizontal velocities at $x = L/2$ on the top and vertical velocities at $y = L/2$ on the bottom. The squares are benchmarks from the Finite Volume Method (Ghia et al., 1982).

4.5.3 Flow over a cylinder

In this section, simulations are carried out for flow over a cylinder to show the capacity of the new boundary scheme for handling curved boundaries. As shown in Fig. 4.9, flow with a constant inlet velocity u_a =0.1m/s interacting with a cylinder is simulated in a rectangular domain with a length of L=0.9m and a height of H=0.6m. The cylinder has a radius of R=0.02m and is located at x=0.5m and y=0.3m. The Reynolds number of the flow is defined by $Re = u_a 2R/v$.

To simulate continuous inflow and outflow at two ends of the channel, the periodic boundary condition is applied by returning the particles to the inlet once it reaches the outlet. It is achieved by setting multiple layers of particles, with the width of $W = 0.1\mathrm{m}$, in the inlet and outlet zone to be mirrored to the outside of the domain by carrying all the flow properties. This treatment also completes the support domains for particles at inlet and outlet boundaries.

The new boundary scheme is applied to all the solid boundaries, including the top wall, bottom wall, and cylinder surface. To use the semi-circular sub-domain on the wall particles at the curved boundary, the diameter goes through the wall particle and tangents to the curved wall, as illustrated in Fig. 4.9. It is worth noting that the wall boundary condition is applied on the diameter of the semi-circle as that for the flat boundary rather than on the actual surface of the cylinder.

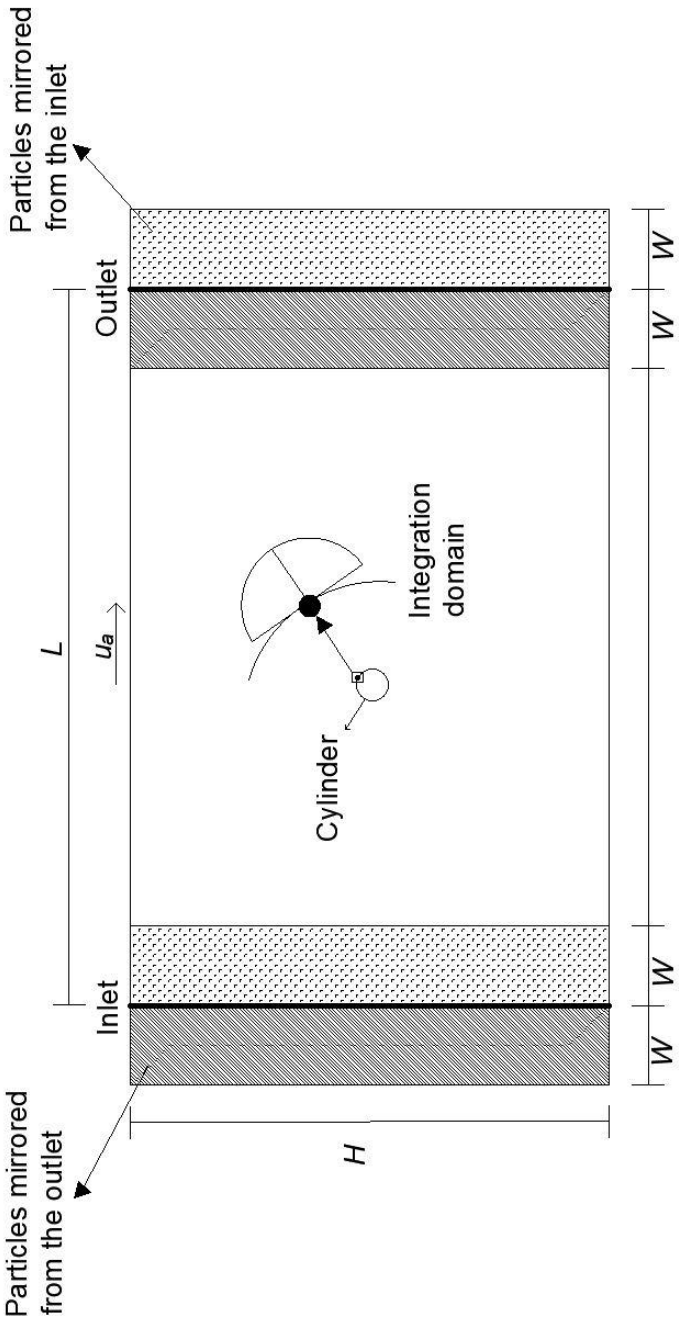

Figure 4.9. Illustration of the simulation domain with mirrored particles to achieve periodic boundaries and integration domain tangent to the curved wall.

The error induced by this procedure can be reduced by increasing the number of particles which has been tested by setting the different particle numbers distributed at the circular wall boundary with $\Delta l = 2\pi R/12, 2\pi R/18$, $2\pi R/24$ and $2\pi R/30$. The flow with $Re = 40$ is simulated, and the pressures relative to the far-field pressure around the cylinder surface are shown in Fig. 4.10. It can be seen that the results converge at $\Delta l = 2\pi R/24 \approx 0.005m$ and show a negligible difference when the particle distance is further decreased to $\Delta l = 2\pi R/30$. Therefore, the particle distance of $\Delta l = 2\pi R/24$ will be adopted for other flow over cylinder tests.

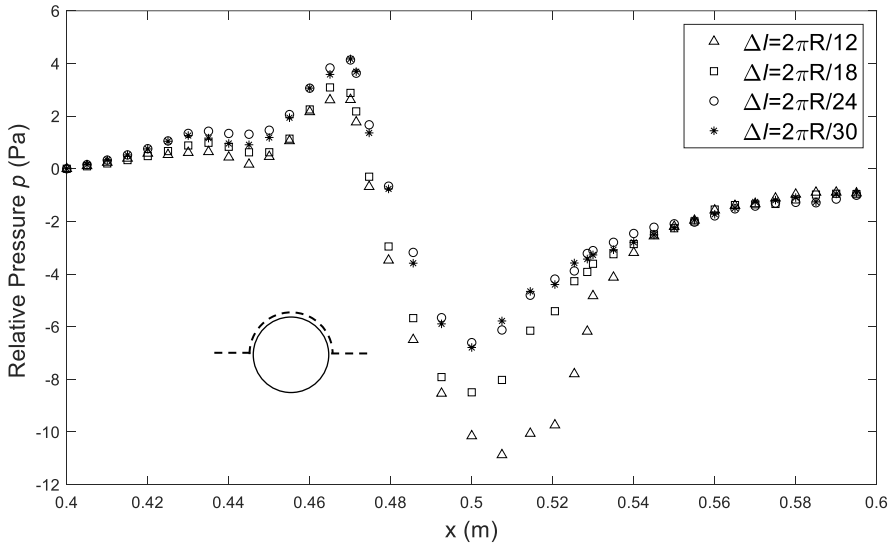

Figure 4.10. Pressure distribution along the upper half surface of the cylinder as shown by dash line for different particle distances in the flow of $Re = 40$.

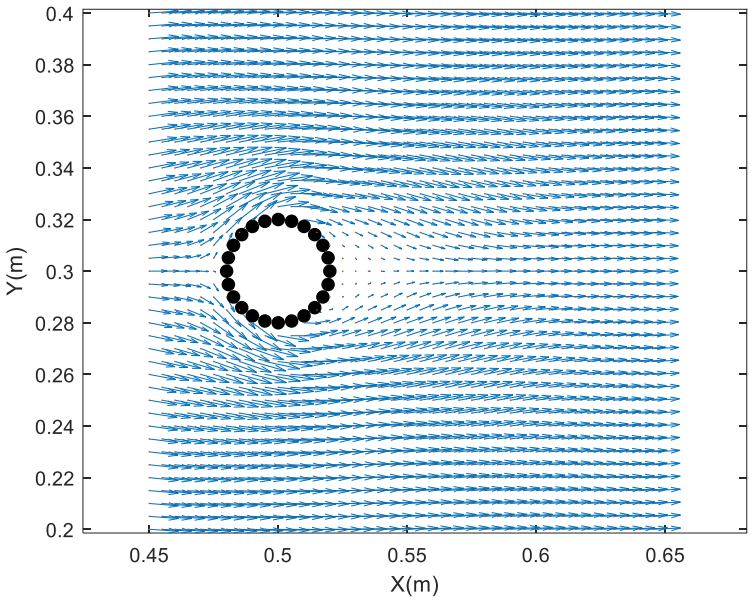
0.4
0.38
0.36
0.34
0.32
0.3
0.28
0.26
0.24
0.22
0.2
Y(m)
0.45
0.5
0.55
0.6
0.65
X(m)

(a) Re =20

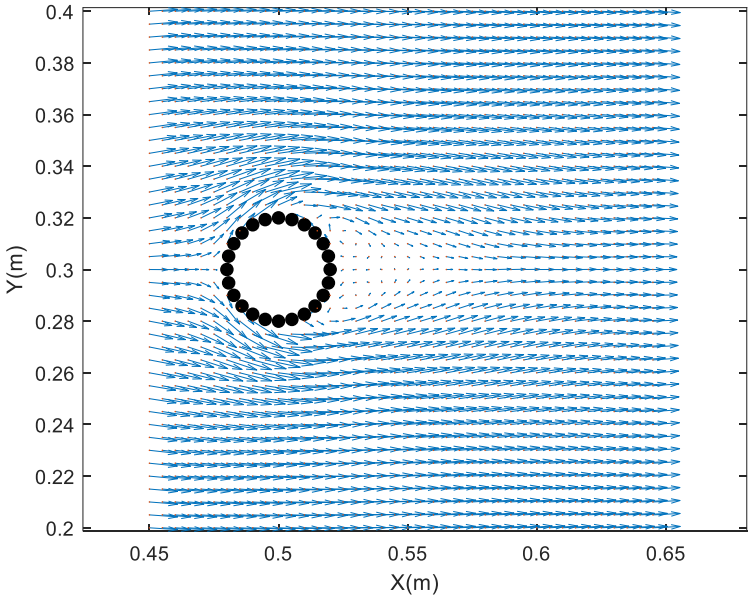
0.4
0.38
0.36
0.34
0.32
0.3
0.28
0.26
0.24
0.22
0.2
Y(m)
0.45
0.5
0.55
0.6
0.65
X(m)

(b) Re =30

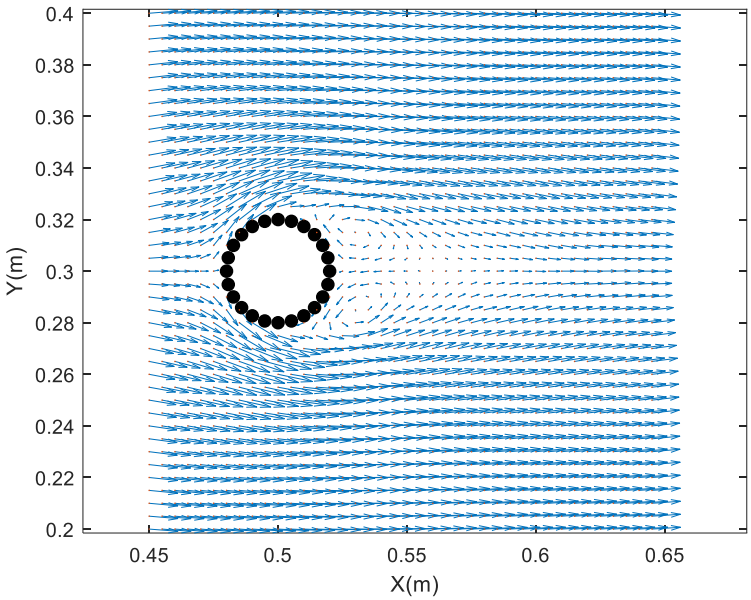
0.4
0.38
0.36
0.34
0.32
0.3
0.28
0.26
0.24
0.22
0.2
Y(m)
0.45
0.5
0.55
0.6
0.65
X(m)

(c) Re =40

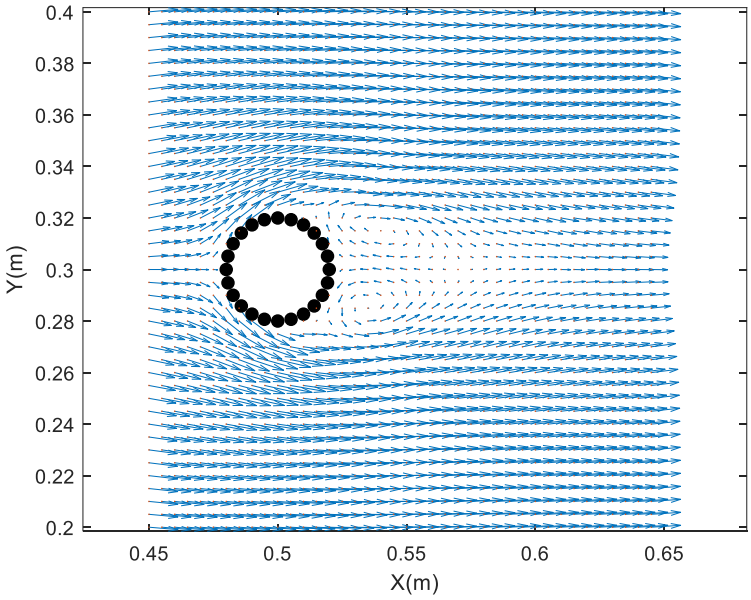
0.4
0.38
0.36
0.34
0.32
0.3
0.28
0.26
0.24
0.22
0.2
Y(m)
0.45
0.5
0.55
0.6
0.65
X(m)

(d) Re =50

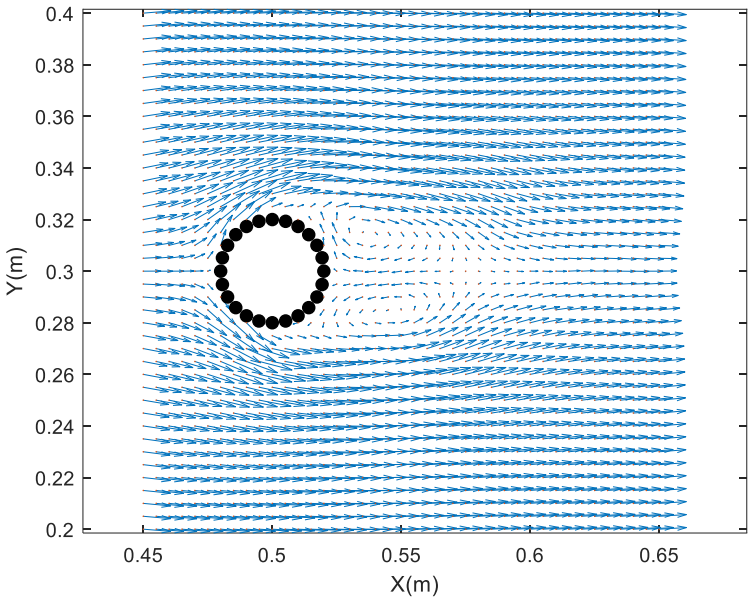

(e) Re =60

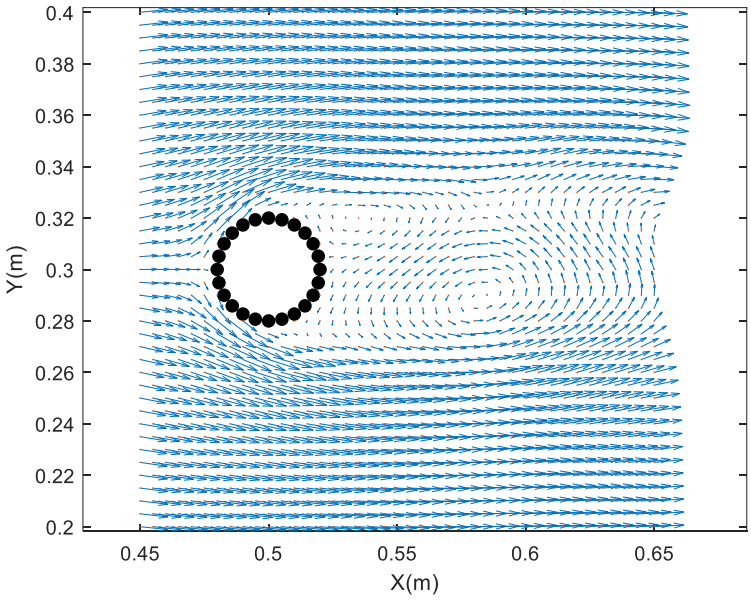

(f) Re =100

Figure 4.11. Velocity field near the cylinder at (a) $Re = 20$; (b) $Re = 30$; (c) $Re = 40$; (d) $Re = 50$; (e) $Re = 60$ and (f) $Re = 100$.

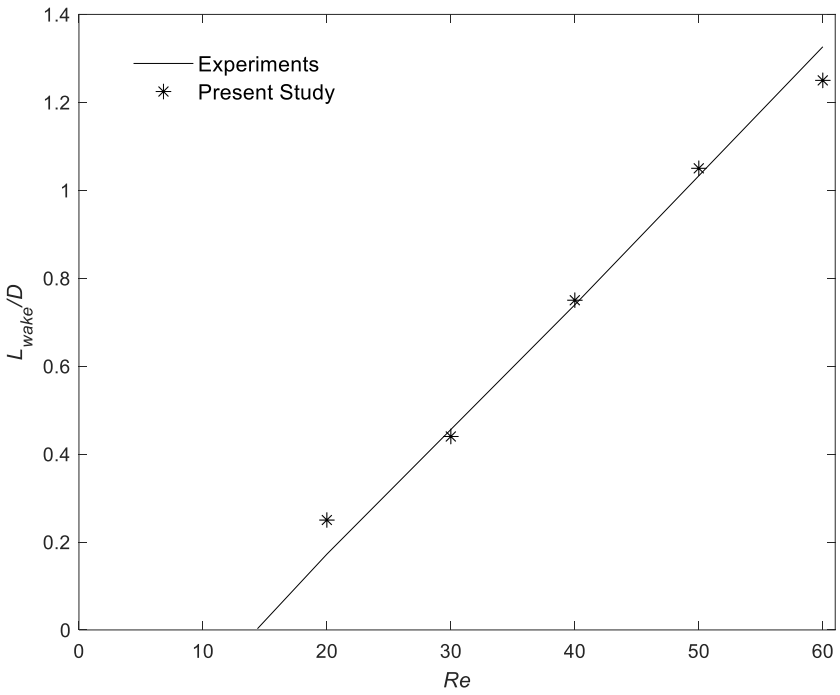

Figure 4.12. Comparison of normalized wake lengths L_{wake}/D with the experimental data (Coutanceau & Bouard, 1977).

The velocity fields are plotted in Fig. 4.11 for Re = 20, 30, 40, 50, 60 and 100. Complex flow phenomena near the cylindrical wall boundary involving wake flow, flow separation and vortex shedding are well captured by the new boundary scheme. It can be seen from Fig. 4.11(a) to (e) that two symmetrical vortexes are generated behind the cylinder for low Re up to 60, with the wake length increased when the Reynolds number gets higher. At a higher $Re = 100$, as shown in Fig. 4.11(f), non-symmetrical wakes are captured, which is consistent with the observation in Ding et al. (2004). Fig. 4.12 demonstrates a good agreement between calculated and measured (Coutanceau & Bouard, 1977) wake lengths for various Re values. Furthermore, the distribution of time-averaged relative pressure coefficient

$C_p = (p - p_\infty)/\frac{1}{2}\rho u_\infty^2$ along the upper half surface of the cylinder at $Re = 100$ is calculated, where p_∞ and u_∞ are the far-field pressure and velocity. Fig. 4.13 shows a good agreement between the results from the present model with the numerical results of Park et al. (1998), which used a high-resolution finite volume method. It should also be noted that the direct discretisation approach for the boundary condition is also tested with the same settings as that in the new boundary approach. Without using any regularization, particle disorder at the wake of the cylinder is significant, which leads to stability issues. But this is much improved for the new boundary scheme as the void in the wake of the cylinder was fairly small (the largest particle distance is about $1.3 \times \Delta l$) and does not expand throughout the simulation until an equilibrium vortex is developed.

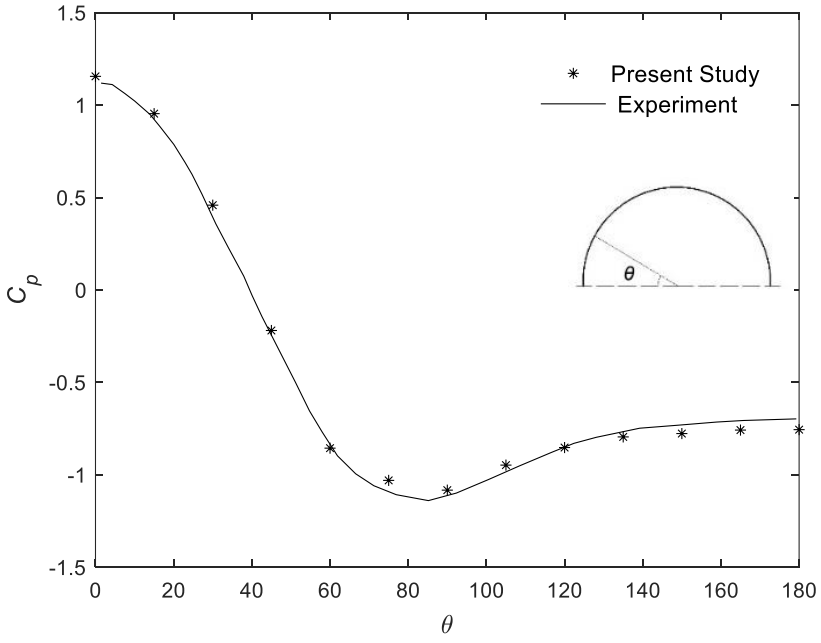

Figure 4.13. Comparison of the time-averaged pressure coefficient C_p along the upper half surface of the cylinder with experimental data (Park et al., 1998) at $Re = 100$.

4.5.4 Monochromic wave generation

In this section, the monochromic wave will be generated by a piston moving wavemaker to examine the performance of the proposed boundary scheme for the moving boundary with accelerations. The monochromic wave is generated in a long rectangular tank with water depth $H = 1m$ and tank length $L = 30m,$ which is sufficiently long to contain several waves without reflection from the far end of the tank. The free-slip boundary condition is imposed on rigid walls, and the motion of the wavemaker (i.e., moving solid boundary particles) is governed by

$$S(t) = a(1 - \cos \omega t) \tag{4.39}$$

$$U_x(t) = a\omega \sin \omega t \tag{4.40}$$

where U_x is the velocity of the wavemaker in the wave progression direction with the amplitude $a = 0.01m$ and the frequency $\omega = 1.45s^{-1}$; S is the displacement of the wavemaker. Like the test in Zhou et al. (2008), the slip boundary condition is applied on the wavemaker with the tangential velocity obtained by calculating the pressure gradient by the SFDI scheme. The generated waves have small wave steepness, i.e., 0.012, and can be characterised as a linear wave for which the surface profile can be expressed by the linearized analytical solution (Eatock Taylor et al., 1994). By setting the initial particle distance $\Delta l = 0.04m$ and the time step $\Delta t = 0.02s$, the new boundary condition scheme is validated by the analytical solution by comparing wave profiles at two instants of $t = 24s$ and $t = 30s$ as shown in Fig. 4.14. It can be seen that the present study has achieved

a good agreement with the analytical solution, which demonstrates the capability of the proposed boundary scheme for treating moving boundaries.

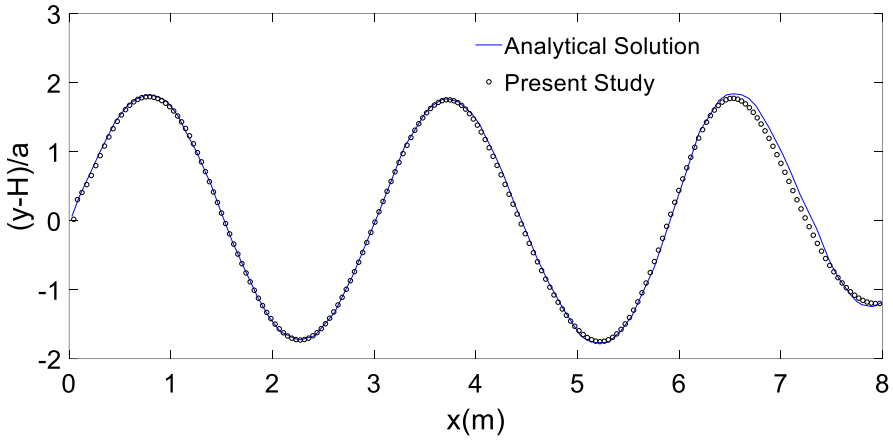

(a) $t = 24s$

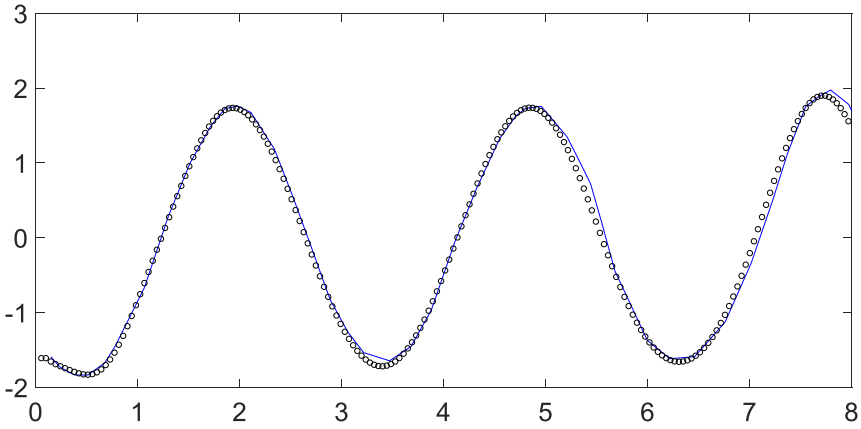

(b) $t = 30s$

Figure 4.14. Comparison with analytical solution (Eatock Taylor et al., 1994) of wave profiles at two instants (a) $t = 24s$ and (b) $t = 30s$ ($a = 0.01m$ and $\omega = 1.45s^{-1}$).

4.6 Conclusion

The present study in Chapter 4 developed a new solid boundary condition implementation scheme for rigid and impermeable walls by integrating the PPE over a semi-circular sub-domain for wall boundary particles with the Neumann pressure boundary condition imposed. In this formulation, terms involving the derivative of the unknown pressure are removed to improve accuracy. Through validating the new scheme by the patch test of solving Poisson's equation, the new scheme achieves a second-order particle distance convergent rate for a range of disorderliness of particle distributions. Higher accuracy is also demonstrated by comparing the results with those of the previous scheme, which directly discretizes the pressure wall boundary condition, especially for particles with relatively high randomness through patch test validations. Apart from the reduction of mean error, the number of particles having large errors is also reduced, thus enhancing the stability of the simulation. In the lid-driven cavity cases, the velocity fields simulated by the model with the new boundary scheme has achieved good agreement with those by the well-established numerical method across a wide range of Reynolds number. The maximum velocities developed in the lid-driven cavity flow which appear near the wall boundary are better captured by the new boundary scheme. In the simulation of flow over a cylinder, the new boundary scheme is applied to the curved surface of the cylinder. The convergent results to various particle numbers show the capacity of the new scheme to deal with non-flat geometries. The development of symmetrical vortex and its length at low Reynolds number and asymmetrical vortex at high Reynolds number are all well captured compared with measurements. The capability of the new boundary approach is also validated for the moving boundary by generating

monochromic waves using a piston wavemaker as the wave surface profiles well agree with the analytical solutions.

Chapter 5: Development of a two-phase model based on incompressible SPH method for simulating suspended sediment motion

5.1 Introduction

Sediment motion in natural water bodies involves a wide range of phenomena like sediment transport, erosion, deposition, suspension, etc. Since the last century, numerous laboratory experiments and theoretical studies have been conducted to explore such complex physical processes (Nakasuji et al., 1990; McNamee, 2000; Bühler & Papantoniou, 2001; Picouet et al., 2001; Dohmen-Janssen & Hanes, 2002; Noguchi & Nezu, 2009; Turowski et al., 2010). This is, however, not an easy task; pure experimental or theoretical studies are not sufficient for comprehensively understanding the mechanics of sediment motion under various flow conditions. As an alternative, numerical modelling has been developed as an effective tool and is widely applied in multiple sciences and engineering applications (Finn et al., 2016; Fonty et al., 2019). Over the past decades, multiphase flow problems have been extensively studied based on the mesh-based Eulerian approaches (Dong & Zhang, 2002; Chang & Hsieh, 2003; Jha & Bombardelli, 2009; Chen et al., 2011; Shi & Yu, 2015; Lee & Huang, 2018). However, tracking the interface or free water surface with deformation or fragmentation remains challenging (Fu & Jin, 2016; Shi et al., 2019). For example, Yeganeh-Bakhtiary et al. (2009) assume the top boundary is fixed with a negligible variation of the free surface, which prevents the vertical velocity and free surface from being effectively modelled.

In the present study, SPH, as a typical meshless Lagrangian method, is extended to study suspended sediment problems under the influence of free surface. Initially developed by Lucy (1977) and Gingold & Monaghan (1977), SPH shows great capabilities in dealing with free surface flows (Gotoh & Khayyer, 2018), and it has already been widely applied in various single-phase flow problems (Liu & Liu, 2010; Zhang et al., 2017; Shadloo et al., 2016). More recently, the SPH method has been of particular interest for modelling sediment-laden flows (Shi et al., 2017; Wang et al., 2017; Shi et al., 2019). For many existing two-phase SPH models, the fluid-sediment mixture is treated as two immiscible phases and represented by two sets of SPH particles (Ulrich et al., 2013; Fourtakas & Rogers, 2016; Zubeldia et al., 2018). It is noticeable that the SPH particles representing the sediment phase in these models consist of the water-soil mixture rather than sediment only, and variables of the mixture are solved rather than the individual phase. Shi et al. (2019) pointed out that the interphase forces and intergranular stresses in these models cannot be addressed directly. Furthermore, the sediment concentration is controlled by the kernel-averaged volumetric approximation in these models, which is too crude for simulating suspended sediment motion. Instead of treating the fluid-sediment mixture as two immiscible fluids, a two-phase SPH model in Shi et al. (2017) and Shi et al. (2019) is developed to simulate sediment-laden flows, in which treating the two phases as two miscible fluids based on a general formulation.

It is worth to mention that all models mentioned above (e.g., Ulrich et al., 2013; Fourtakas & Rogers, 2016; Zubeldia et al., 2018; Shi et al., 2017; Shi et al., 2019) are based on the weakly compressible SPH (WCSPH) method where the pressure field is explicitly solved through the Equation of State

(EoS). Only a few attempts (Ran et al., 2015; Pahar & Dhar, 2017) have been made through the incompressible SPH (ISPH) formulations to solve two-phase problems, with some questionable assumptions. Specifically, Ran et al. (2015) proposed a two-phase model based on the ISPH scheme for simulating movable bed dam-break flows, but the sediment bed is treated as an erodible solid wall. In Pahar & Dhar (2017), the variation of sediment concentration is simply omitted by assuming that the solid concentration is equal to a constant for each SPH particle. Such oversimplified SPH models lack generalizability and cannot be employed for simulating suspended sediment motion problems.

The present study in Chapter 5 aims to develop a two-phase model based on the ISPH scheme with a general formulation. The two phases of sediment-laden flow are considered to be miscible, and each phase is described by a single set of governing equations. Furthermore, the computational domain is discretized by a single set of SPH particles to avoid variable smoothing length scales and non-conservation momentum problems (Laibe & Price, 2014). The SPH particles move with the water velocity and carry local properties of both phases by employing the volume fraction representation, which is detailed in Monaghan & Kocharyan (1995), Monaghan (1997) and Kwon & Monaghan (2015). The intergranular stresses and interphase forces are addressed directly in momentum equations. The Large-eddy simulation (LES) and sub-particle scale models are employed to represent the turbulent effect, and the turbulent viscosities are determined by the Smagorinsky model. Additionally, the hindered settling effect is also considered concerning to the drag force. The classic two-step projection approach is used for solving the pressure with certain modifications to fit the two-phase scenario. In this work, the new model has

been validated by the analytical solution of two idealized problems of still water containing both neutrally buoyant and naturally settling sand. Application to the sand dumping problem is also investigated.

In the rest of Chapter 5, the governing equations and corresponding two-phase formulations are described in Section 5.2. Boundary conditions and discretized equations are presented in Sections 5.3 and 5.4, respectively. Code implementations of the ISPH model are given in Section 5.5. Validation for idealized cases and application of the proposed model to the sand dumping problem are discussed in Sections 5.6 and 5.7, respectively. Finally, conclusions are summarized in Section 5.8.

5.2 Formulation of the two-phase ISPH model

5.2.1 Governing equations

Governing equations for two-phase flows

In this new two-phase ISPH model, the fluid and sediment phases are described as two miscible continua within the domain of interest. The fluid-sediment mixture is discretized into a single set of SPH particles governed by the conservation laws for mass and momentum. Each SPH particle carries the properties of different phases by introducing the corresponding volume fraction of sediment and fluid. Following the two-phase form

governing equations originally derived by Drew (1983), the continuity equations in Eulerian form can be written as

$$\frac{\partial \alpha_f \rho_f}{\partial t} + \frac{\partial \alpha_f \rho_f u_{f,j}}{\partial x_j} = 0 \tag{5.1}$$

$$\frac{\partial \alpha_s \rho_s}{\partial t} + \frac{\partial \alpha_s \rho_s u_{s,j}}{\partial x_j} = 0 \tag{5.2}$$

where, α is the volume fraction in which $\alpha_f + \alpha_s = 1$; ρ is the density; u is the velocity component; t is the time; x is the coordinate; the subscripts of f and s represent the fluid phase and the sediment phase, respectively; following the summation convention, the indices i or j represent the coordinate directions.

The momentum equations for the two phases in Eulerian form can be written as

$$\frac{\partial \alpha_f \rho_f u_{f,i}}{\partial t} + \frac{\partial \alpha_f \rho_f u_{f,i} u_{f,j}}{\partial x_j} = -\alpha_f \frac{\partial p}{\partial x_i} + \frac{\partial \alpha_f \rho_f T_{f,ij}}{\partial x_j} + \alpha_f \rho_f g_i - F_i \tag{5.3}$$

$$\frac{\partial \alpha_s \rho_s u_{s,i}}{\partial t} + \frac{\partial \alpha_s \rho_s u_{s,i} u_{s,j}}{\partial x_j} = -\alpha_s \frac{\partial p}{\partial x_i} + \frac{\partial \alpha_s \rho_s T_{s,ij}}{\partial x_j} + \alpha_s \rho_s g_i + F_i \tag{5.4}$$

where p is the pressure; g is the acceleration of gravity (i.e., $g = 9.8 m/s^2$); another two terms involving stresses and interphase forces will be discussed in the following context.

In Eqs. (5.3) and (5.4), the stress tensor term represents the effect of viscous and turbulent stresses and can be expressed as

$$T_k = \frac{(\tau_k^0 + \tau_k^t)}{\alpha_k \rho_k} = (v_k^0 + v_k^t)\left(\frac{\partial u_{k,i}}{\partial x_j} + \frac{\partial u_{k,j}}{\partial x_i}\right) \tag{5.5}$$

where τ^0 represents the viscous stress and τ^t represents the sub-particle stress; v^0 and v^t is the kinematic viscosity and eddy viscosity, respectively; the index $k = f, s$.

The viscous stress tensor τ_k^0 can be determined by

$$\tau_{k,ij}^0 = \alpha_k \rho_k v_k^0 \left(\frac{\partial u_{k,i}}{\partial x_j} + \frac{\partial u_{k,j}}{\partial x_i}\right) \tag{5.6}$$

According to Ahilan & Sleath (1987), the relationship between v_f^0 and v_s^0 can be expressed as

$$v_s^0 = 1.2 \frac{\rho_f}{\rho_s} \left[\left(\frac{\alpha_{sm}}{\alpha_s}\right)^{\frac{1}{3}} - 1\right]^{-2} v_f^0 \tag{5.7}$$

where v_f^0 is set to be the kinematic viscosity of water (i.e., $v_f^0 = 1 \times 10^{-6} m^2/s$); α_{sm} is the maximum volume fraction of sediment, equal to 0.606, referring to Lin & Wang (2006).

It is believed that the presence of turbulence should be considered in most sediment-laden flow problems (Shi et al., 2017; Luo et al., 2021). However, the usage of the turbulence model should be problem-dependent (Sriram & Ma, 2021). In general, two turbulence modelling approaches are widely used in meshless methods (Luo et al., 2021). One is the $k - \varepsilon$ approach, which models the Reynolds stress in the Reynold-Averaged Navier-Stokes (RANS) equations; another one is the sub-particle scale (SPS) model, which resolves the fluid motions to a prescribed scale based on the large eddy simulation (LES) method. Both approaches have been used in various coastal engineering applications, but Luo et al. (2021) figured out that precise reproduction of turbulence is a distinct significant challenge. In this study, large eddy simulation (LES) along with a sub-particle model is introduced to deal with the turbulent effect, referring to its successful applications in SPH modelling of turbulent water flows (Dalrymple & Rogers, 2006; Mayrhofer et al., 2015, Shi et al., 2017; Shi et al., 2019).

The general implementation of the SPS model in SPH was proposed by Gotoh et al. (2001), and the sub-particle stress based on the Boussinesq hypothesis, which stipulates the turbulent stress is related to the mean velocity gradients in a similar way as that of the viscous stress, has been widely used and one of the commonly used forms is

$$\tau_{k,ij}^{t} = \alpha_k \rho_k v_k^t \left(\frac{\partial u_{k,i}}{\partial x_j} + \frac{\partial u_{k,j}}{\partial x_i} \right) \tag{5.8}$$

The widely used Smagorinsky (1963) model is employed here to determine the eddy viscosities v_k^t; additionally, a modification is adopted here considering the existence of sediment particles (Chen et al., 2011; Shi et al., 2017).

$$v_k^t = (C_k \Delta)^2 |\boldsymbol{S_k}| \left(1 - \frac{\alpha_s}{\alpha_{sm}}\right)^n \tag{5.9}$$

where C_k is Smagorinsky constant taken to be 0.10 according to a similar application of sand dumping case conducted by Shi et al. (2017); Δ is the initial particle distance; $|\boldsymbol{S_k}|$ is the local strain rate, while $\left|S_{k,ij}\right| = \sqrt{2S_{k,ij}S_{k,ij}}$ and its elements can be calculated as shown below:

$$S_{k,ij} = \frac{1}{2}\left(\frac{\partial u_{k,i}}{\partial x_j} + \frac{\partial u_{k,j}}{\partial x_i} \right) \tag{5.10}$$

The term linked with the interphase forces (e.g., drag, lift, or added mass forces) aims to maintain force balance between different phases. According to Nguyen et al. (2012), only the drag force caused by the relative motion between the sediment and fluid phases needs to be considered for describing the sand dumping case in still water included in the present study. It can be expressed as

$$F_i = \gamma \alpha_s \left(u_{f,i} - u_{s,i}\right) \tag{5.11}$$

and the coefficient γ is estimated based on the formula initially proposed by Gidaspow (1944) and given by

$$\gamma = \begin{cases} \frac{3}{4} C_D \frac{\rho_f \left|\boldsymbol{u_f} - \boldsymbol{u_s}\right|}{d_s} \alpha_f^{-1.65} & \alpha_s \leq 0.2 \\ 150 \frac{\alpha_s \rho_f v_f^0}{\alpha_f d_s^2} + 1.75 \frac{\rho_f \left|\boldsymbol{u_f} - \boldsymbol{u_s}\right|}{d_s} & \alpha_s > 0.2 \end{cases} \tag{5.12}$$

where $|\boldsymbol{u}|$ is the norm of the velocity vector.

C_D is a coefficient determined by the particle Reynolds number $Re_s = \alpha_f \left|\boldsymbol{u_f} - \boldsymbol{u_s}\right| d_s / v_f^0$ and given by

$$C_D = \begin{cases} \frac{24}{Re_s}\left(1.0 + 0.15 Re_s^{0.687}\right) & Re_s < 1000 \\ 0.44 & Re_s \geq 1000 \end{cases} \tag{5.13}$$

Governing equations in the Lagrangian form

It is noticeable that the governing equations for two-phase flows are discretized into a single set of SPH particles in the present study. Thus, the SPH particles are set to be moving with the velocity of the water phase, and the substantial derivative associated with each SPH particle can be expressed as:

$$\frac{d\varphi}{dt} = \frac{\partial \varphi}{\partial t} + u_{f,j}\frac{\partial \varphi}{\partial x_j} \tag{5.14}$$

where the notion of φ represents the physical quantities (i.e., the velocity of the fluid or sediment phase) carried by the SPH particles.

The Lagrangian form of governing equations is described in the following context, and the continuity and momentum equations for the fluid phase are rewritten in Lagrangian form as the substantial derivative Eq. (5.14) is introduced, it gives:

$$\frac{d\alpha_f}{dt} = -\alpha_f \frac{\partial u_{f,j}}{\partial x_j} \tag{5.15}$$

$$\frac{du_{f,i}}{dt} = -\frac{1}{\rho_f}\frac{\partial p}{\partial x_i} + \frac{1}{\alpha_f \rho_f}\frac{\partial \alpha_f \rho_f T_{f,ij}}{\partial x_j} + g_i - \frac{F_i}{\alpha_f \rho_f} \tag{5.16}$$

Note that the fluid and sediment phases are considered to be incompressible. Manipulating Eqs. (5.2) and (5.14), it is easy to derive the continuity equation of the sediment phase as

$$\frac{d\alpha_s}{dt} = -\alpha_s \frac{\partial u_{f,j}}{\partial x_j} - \frac{\partial\left[\alpha_s\left(u_{s,j} - u_{f,j}\right)\right]}{\partial x_j} \tag{5.17}$$

Since the velocities differ between phases, the mass and momentum fluxes exist among SPH particles. Accordingly, these two terms on the right side of Eq. (5.17) represent the volume change of each SPH particle and the effect of inter-particle sediment mass flux, respectively.

Transforming Eq. (5.4) to the Lagrangian form of momentum equation of the sediment phase by introducing Eq. (5.14) yields

$$\frac{du_{s,i}}{dt} = -\left(u_{s,j} - u_{f,j}\right)\frac{\partial u_{s,i}}{\partial x_j} - \frac{1}{\rho_s}\frac{\partial p}{\partial x_i} + \frac{1}{\alpha_s \rho_s}\frac{\partial \alpha_s \rho_s T_{s,ij}}{\partial x_j} + g_i + \frac{F_i}{\alpha_s \rho_s} \tag{5.18}$$

where the first term on the right side of Eq. (5.18) represents the inter-particle momentum flux.

The complete derivations from the Eulerian form governing equations to the Lagrangian form are given in Appendix B.

5.2.2 Pressure solution algorithm

In the present study, the pressure is determined implicitly by solving a Pressure Poisson Equation (PPE) rather than an equation of state, which makes it distinctive from the weakly compressible SPH (WCSPH) method. This algorithm for pressure solution was first proposed by Koshizuka and Oka (1996) and further developed by Shao & Lo (2003), also known as the two-step prediction-correction procedure. It is expected to achieve an improved pressure field and velocities with the ISPH method (Lee et al., 2008; Xu et al., 2009). In this work, variables of the fluid and sediment phases are solved separately following the classic single-phase prediction-correction procedure.

Solution for the fluid phase

In the first prediction step, intermediate velocities and positions of the fluid phase are evaluated without considering the pressure term, shown as

$$\boldsymbol{u}_f^* = \boldsymbol{u}_f^n + \left(\frac{1}{\alpha_f^n \rho_f}\nabla \cdot \left(\alpha_f^n \rho_f \boldsymbol{T}_f\right) + \boldsymbol{g} - \frac{\boldsymbol{F}}{\alpha_f^n \rho_f}\right)\Delta t \tag{5.19}$$

$$\boldsymbol{r}^* = \boldsymbol{r}^n + \boldsymbol{u}_f^* \Delta t \tag{5.20}$$

where $\boldsymbol{r}^*$ is the position vector of a SPH particle; Δt is the time step; the superscript n indicates the *n*-step time at $t = t^n$; and the superscript $*$ represents the intermediate step between t^n and $t^{n+1} = t^n + \Delta t$.

On this basis, the velocities of the fluid phase at t^{n+1} can be expressed as

$$\boldsymbol{u}_f^{n+1} = \boldsymbol{u}_f^* - \frac{\Delta t}{\rho_f}\nabla p^{n+1} \tag{5.21}$$

By taking the divergence for both sides of Eq. (5.19), the pressure Poisson equation (PPE) is obtained as below:

$$\left(\nabla \cdot \frac{\Delta t}{\rho_f}\nabla p^{n+1}\right) = \nabla \cdot \boldsymbol{u}_f^* - \nabla \cdot \boldsymbol{u_f}^{\boldsymbol{n+1}} \tag{5.22}$$

where $\nabla \cdot \boldsymbol{u_f}^*$ can be explicitly solved; and *(n+1)*-step divergence of velocity $\nabla \cdot \boldsymbol{u_f}^{\boldsymbol{n+1}}$ should satisfy the continuity equation, i.e., Eq. (5.13), which gives

$$\nabla \cdot \boldsymbol{u_f}^{\boldsymbol{n+1}} = -\frac{\left(a_f^n - a_f^{n-1}\right)}{a_f^n \Delta t} \tag{5.23}$$

Next, the pressure of the fluid particle can be solved as

$$\frac{\Delta t}{\rho_f}\nabla^2 p^{n+1} = \nabla \cdot \boldsymbol{u_f}^* + \frac{\left(a_f^n - a_f^{n-1}\right)}{a_f^n \Delta t} \tag{5.24}$$

Then, the corrected velocities and positions of the fluid phase are updated as the pressure field is implicitly solved

$$\boldsymbol{u}_f^{n+1} = \boldsymbol{u}_f^* - \frac{\Delta t}{\rho_f}\nabla p^{n+1} \tag{5.25}$$

$$\boldsymbol{r}^{n+1} = \boldsymbol{r}^n + \boldsymbol{u}_f^{n+1}\Delta t \tag{5.26}$$

Solution for the sediment phase

Despite considering the change of position for the sediment phase as they are moving with the fluid velocity, the velocity of the sediment phase can be explicitly obtained as

$$\boldsymbol{u}_s^{n+1} = \boldsymbol{u}_s^n + \left[-\frac{1}{\rho_s}\nabla p + \frac{1}{\alpha_s^n \rho_s}\nabla\cdot(\alpha_s^n \rho_s \boldsymbol{T}_s) + \boldsymbol{g} + \frac{\boldsymbol{F}}{\alpha_s^n \rho_s} - \left(\boldsymbol{u}_s^n - \boldsymbol{u}_f^n\right)\cdot\nabla\boldsymbol{u}_s^n\right]\Delta t \tag{5.27}$$

Finally, updating of volume fraction according to Eq. (5.15) is given by

$$\alpha_s^{n+1} = \alpha_s^n + \left[-\alpha_s^n \nabla\cdot\boldsymbol{u}_f^n - \nabla\cdot\alpha_s^n\left(\boldsymbol{u}_s^n - \boldsymbol{u}_f^n\right)\right]\Delta t \tag{5.28}$$

and

$$\alpha_f^{n+1} = 1 - \alpha_s^{n+1} \tag{5.29}$$

5.3 Boundary conditions

5.3.1 Solid walls

In this work, the solid wall boundaries are represented by a single layer of SPH particles fixed along the boundary lines. The impermeable wall boundary condition is imposed on those boundary particles. The direct discretization of impermeable wall boundary conditions involving the normal pressure gradient has been successfully applied in MLPG/SPH simulations (Ma, 2005 a, b; Ma & Zhou, 2009; Ran et al., 2015; Pahar & Dhar, 2017). Here, the boundary treatment scheme proposed by Ma & Zhou (2009) is employed, and the boundary condition is given below.

On the impermeable boundaries, the velocity satisfies

$$\boldsymbol{n} \cdot \boldsymbol{u_f} = \boldsymbol{n} \cdot \boldsymbol{U} \tag{5.30}$$

where $\boldsymbol{n}$ is the unit normal vector of the wall boundaries and $\boldsymbol{U}$ is the velocity of wall boundaries.

By substituting Eq. (5.30) to Eq. (5.19), the pressure Neumann boundary condition is to be satisfied as

$$\boldsymbol{n} \cdot \nabla p = \frac{\rho_f}{\Delta t} \boldsymbol{n} \cdot \left(\boldsymbol{u_f^*} - \boldsymbol{U} \right) \tag{5.31}$$

where $\boldsymbol{u}_f^*$ is explicitly calculated by Eq. (5.21) and $\boldsymbol{u}_f^{n+1}$ is replaced by $\boldsymbol{U}$. If the wall boundary particles are fixed, $\boldsymbol{n} \cdot \boldsymbol{U} = 0$.

In addition, mass transfer is ignored between the inner particles and boundary particles since the scope of the current study is limited to suspended load motion. The primary purpose of imposing such a boundary scheme is to prevent inner particles from penetrating the solid walls. Thus, the solid boundary particles are set to be pure fluid particles.

5.3.2 Free surfaces

In ISPH, the Dirichlet pressure condition (i.e., the zero pressure) is typically imposed to the free surface particles (Shao & Lo, 2003). However, some misjudgements can happen concerning the identification of free surface particles as the free surface can deform violently. Therefore, various numerical techniques have been developed when modelling cases with the free surface. Specifically, the free surface particles are identified by evaluating the particle number density in Lo & Shao (2002), the divergence of a particle position in Lee et al. (2008), the particle spacing based on the summation of x-coordinate or y-coordinate of relative particle positions (Khayyer et al., 2009) and the colour function (Zheng et al., 2021).

A free surface particle identification scheme developed by Ma & Zhou (2009) is employed here with some modifications to improve the robustness of present simulation cases. As shown in Fig. 5.1(a) and (b), **I** is a random

fluid particle near the free surface with an outer circle that represents a searching domain with the radius *r* is taken to be $2.5 \times \Delta l$. The searching domain is divided into four divisions in Fig. 5.1(a) and is overlapped with four rectangular columns in Fig. 5.1(b).

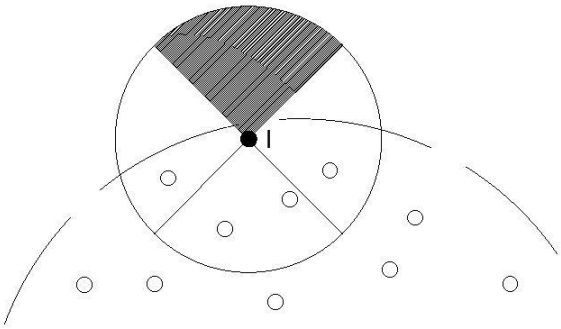

(a)

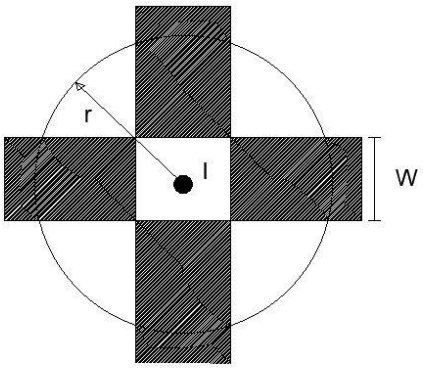

(b)

Figure 5.1(a) A random fluid particle **I** close to the free surface, i.e., the dashed line (the outer circle centred at particle **I** represents the searching domain with four 90-degree divisions and the small hollow circles are its neighbouring particles); (b) The target fluid particle **I** within the searching

domain, which is overlapped with four rectangular columns with the width equal to $0.8 \times \Delta l$ (Δl is the initial particle spacing).

The free surface particle identification scheme is based on two auxiliary functions, as shown below

$$FSNode_{quater}(\mathbf{I}) = \begin{cases} 1 & if\ N \leq 3 \\ 0 & if\ N > 3 \end{cases} \tag{5.32}$$

$$FSNode_{column}(\mathbf{I}) = \begin{cases} 1 & if\ N \leq 3 \\ 0 & if\ N > 3 \end{cases} \tag{5.33}$$

where $N = N_{east} + N_{west} + N_{north} + N_{south}$; and $N_{(east)}$, for instance, represents if there is at least one neighbouring particle existing in the east quadrant or column (i.e., the coloured region in Fig. 5.1(a) & (b)); if yes, $N_{east} = 1$, if no, $N_{east} = 0$.

If the particle **I** simultaneously satisfies the following conditions, the concerning inner fluid particle **I** can be considered as a free surface particle and imposed with the previously mentioned free surface boundary condition (i.e., the zero pressure).

$FSNode_{quater}(\mathbf{I}) = 1$

$FSNode_{column}(\mathbf{I}) = 1$

It is noticeable that the vast majority of the free surface particles can be identified efficiently in the present study with very limited misjudgements, but this has no significant impact on the overall computational accuracy.

5.4 Discretized equations

The general SPH formulations are presented in Section 3.3. For the two-phase ISPH model, the volume of a particle b can be defined by

$$V_b = \left(\frac{m_f}{a_f \rho_f}\right)_b \tag{5.34}$$

Note that the m_f being the mass of fluid phase carried by each SPH particle and remains constant during the simulations.

Although the classic SPH formulations have proven successful for modelling many free-surface flow problems with large deformation, the gradient or Laplacian operator calculation might be problematic in those regions near the rigid boundaries or free surfaces. Thus, some approaches have been developed to address the challenges of calculating the second-order or higher derivatives with the SPH method (Chen et al., 1999; Bonet & Kulasegaram, 2000; Chaniotis et al., 2002; Zhang & Batra, 2004; Liu & Liu, 2006; Schwaiger, 2008). In this work, an implicit corrected SPH formulation (Schwaiger, 2008) is employed to address the difficulties in

calculating the first and second-order derivatives of field values. An essential characteristic of this technique is introducing a simple correction term that incrementally improves gradient or Laplacian operator calculation (Schwaiger, 2008). Schwaiger (2008) also conducted a series of tests to demonstrate the reduced relative errors in approximating the Laplacian calculations on a square patch.

The corrected form of the first and second derivatives of φ is given by:

$$\nabla\varphi_a = \sum_b V_b(\varphi_b - \varphi_a)\mathbf{L}\cdot\nabla W_{ab} \tag{5.35}$$

And

$$\nabla^2\varphi_a = \frac{2tr(\boldsymbol{\Gamma}^{-1})}{n}\left\{\sum_b V_b(\varphi_b - \varphi_a)\frac{\boldsymbol{r_{ab}}\cdot\nabla W_{ab}}{|r_{ab}|^2} - \nabla\varphi_a\cdot\left(\sum_b V_b\,\nabla W_{ab}\right)\right\} \tag{5.36}$$

where $n = 2$ in the 2D cases;

and the discretized form of the correction term $\mathbf{L}$ and $\boldsymbol{\Gamma}$ can be defined by

$$\mathbf{L} = \begin{pmatrix} \sum_b V_b\Delta x\frac{\partial W_{ab}}{\partial x_i} & \sum_b V_b\Delta x\frac{\partial W_{ab}}{\partial x_j} \\ \sum_b V_b\Delta y\frac{\partial W_{ab}}{\partial x_i} & \sum_b V_b\Delta y\frac{\partial W_{ab}}{\partial x_j} \end{pmatrix}^{-1} \tag{5.37}$$

and

$$\boldsymbol{\Gamma} = \begin{pmatrix} \sum_b V_b \frac{\boldsymbol{r}_{ab} \cdot \nabla W_{ab}}{|r_{ab}|^2} \Delta x \Delta x & \sum_b V_b \frac{\boldsymbol{r}_{ab} \cdot \nabla W_{ab}}{|r_{ab}|^2} \Delta x \Delta y \\ \sum_b V_b \frac{\boldsymbol{r}_{ab} \cdot \nabla W_{ab}}{|r_{ab}|^2} \Delta x \Delta y & \sum_b V_b \frac{\boldsymbol{r}_{ab} \cdot \nabla W_{ab}}{|r_{ab}|^2} \Delta y \Delta y \end{pmatrix} \tag{5.38}$$

as $\Delta x = x_b - x_a$; $\Delta y = y_b - y_a$; $\boldsymbol{r}_{ab} = (\Delta x, \Delta y)$ and $|r_{ab}| = \sqrt{(\Delta x)^2 + (\Delta y)^2}$.

According to Eq. (5.37), the divergence of the velocity at point a can be written as

$$\left(\frac{\partial u_{k,j}}{\partial x_j}\right)_a = \sum_b V_b \left[\left(u_{k,j}\right)_b - \left(u_{k,j}\right)_a\right] (\mathbf{L})_j \cdot (\nabla W_{ab})_j \tag{5.39}$$

Similarly, the gradient of pressure at point a can be written as

$$\left(\frac{\partial p}{\partial x_i}\right)_a = \sum_b V_b [(p)_b - (p)_a] (\mathbf{L})_i \cdot \nabla W_{ab} \tag{5.40}$$

The discretized equation for the interparticle mass flux term in Eq. (5.17) is given by

$$\left\{-\frac{\partial\left[\alpha_s\left(u_{s,j}-u_{f,j}\right)\right]}{\partial x_j}\right\}_a =$$
$$-\left[\left(u_{s,j}\right)_a-\left(u_{f,j}\right)_a\right]\sum_b V_b[(\alpha_s)_b-(\alpha_s)_a](\mathbf{L})_j\cdot(\nabla W_{ab})_j \tag{5.41}$$

And the discretized equation for the inter-particle momentum flux term in Eq. (5.18) is given by

$$\left\{-\left(u_{s,j}-u_{f,j}\right)\frac{\partial u_{s,i}}{\partial x_j}\right\}_a =$$
$$-\left[\left(u_{s,j}\right)_a-\left(u_{f,j}\right)_a\right]\sum_b V_b\left[\left(u_{s,i}\right)_b-\left(u_{s,i}\right)_a\right](\mathbf{L})_j\cdot(\nabla W_{ab})_j \tag{5.42}$$

A preferable symmetric form proposed by Ren et al. (2014) is applied to discretize the viscous term, and it yields

$$\left(\frac{\partial T_{k,ij}}{\partial x_j}+T_{k,ij}\frac{\partial\ln(\alpha_k)}{\partial x_j}\right)_a =$$
$$\sum_b V_b\left[\left(T_{k,ij}\right)_a+\left(T_{k,ij}\right)_b\right]\left[1+\frac{1}{2}\ln\frac{(\alpha_k)_b}{(\alpha_k)_a}\right](\nabla w_{ab})_j \tag{5.43}$$

It is noted that the term $T_{k,ij}\frac{\partial\alpha_k}{\partial x_j}$ is replaced by $T_{k,ij}\frac{\partial\ln(\alpha_k)}{\partial x_j}$ as α_s may vanish in $\ln\left[\frac{(\alpha_k)_b}{(\alpha_k)_a}\right]$ due to possible sediment concentration discontinuity (Shi et al., 2017).

According to Eq. (5.36), the Laplacian operator of pressure in PPE (i.e., Eq. (5.22)) is discretized as

$$(\nabla^2 p)_a = \frac{2tr(\boldsymbol{\Gamma}^{-1})}{n}\left\{\sum_b V_b(p_b - p_a)\frac{\boldsymbol{r_{ab}}\cdot\nabla w_{ab}}{|r_{ab}|^2} - (\nabla p)_a \cdot \left(\sum_b V_b \nabla w_{ab}\right)\right\} \tag{5.44}$$

Finally, the discrete form of governing equations for two-phase flow problems is tabulated below:

$$\frac{d(\alpha_f)_a}{dt} = -(\alpha_f)_a \sum_b V_b \left[(u_{f,j})_b - (u_{f,j})_a\right](\mathbf{L})_j \cdot (\nabla W_{ab})_j \tag{5.45}$$

$$\begin{aligned}\frac{d(u_{f,i})_a}{dt} = &-\frac{1}{\rho_f}\sum_b V_b(p_b - p_a)(\mathbf{L})_i \cdot \nabla W_{ab} \\ &+ \sum_b V_b\left[(T_{f,ij})_a + (T_{f,ij})_b\right]\left[1 + \frac{1}{2}\ln\frac{(\alpha_f)_b}{(\alpha_f)_a}\right] \times (\nabla W_{ab})_j \\ &+ g_i - \frac{F_i}{(\alpha_f)_a \rho_f}\end{aligned} \tag{5.46}$$

$$\frac{d(u_{s,i})_a}{dt} = -\left[(u_{s,j})_a - (u_{f,j})_a\right]\sum_b V_b\left[(u_{s,i})_b - (u_{s,i})_a\right](\mathbf{L})_j \cdot (\nabla W_{ab})_j$$
$$-\frac{1}{\rho_s}\sum_b V_b(p_b - p_a)(\mathbf{L})_i \cdot \nabla W_{ab}$$
$$+\sum_b V_b\left[(T_{s,ij})_a + (T_{s,ij})_b\right]\left[1 + \frac{1}{2}\ln\frac{(\alpha_s)_b}{(\alpha_s)_a}\right] \times (\nabla W_{ab})_j$$
$$+g_i + \frac{F_i}{(\alpha_s)_a\rho_s} \tag{5.47}$$

$$\frac{d(\alpha_s)_a}{dt} = -\left[(u_{s,j})_a - (u_{f,j})_a\right]\sum_b V_b[(\alpha_s)_b - (\alpha_s)_a](\mathbf{L})_j \cdot (\nabla W_{ab})_j$$
$$-(\alpha_s)_a\sum_b V_b\left[(u_{f,j})_b - (u_{f,j})_a\right](\mathbf{L})_j \cdot (\nabla W_{ab})_j \tag{5.48}$$

5.5 Code implementations

The proposed ISPH model is implemented based on the Visual Studio 2015 platform and programmed with Fortran.

A 2-dimensional two-phase ISPH code is developed in this thesis, and it incorporates basic conservation equations for various fluid-sediment motions in a water tank system. The simplified structure of the two-phase ISPH code is shown in Fig. 5.2. The basis of the ISPH code is consist of the initialization part, main algorithm subroutines, and output, respectively. Specifically, the initial geometry is set by generating inner/boundary

particles with pre-defined physical quantities. Following the two-step prediction-correction procedure, the nearest neighbouring particle search (NNPS) scheme is conducted for all particles at each time step. The viscosity and drag force for each phase are calculated explicitly first. Then the intermediate velocity and position for the fluid phase are computed at the intermediate time step. After that, the matrix of the PPE equation is assembled, and the fluid pressure can be solved through a solver. The next step fluid velocity and position of each particle is then corrected. Finally, the corresponding velocity of the sediment phase and volume of fraction can also be updated as the pressure field is obtained by solving PPE. The iterative calculation is performed within the time loop until the terminal condition is researched. Once the time loop stops, the stored data will be exported as txt files.

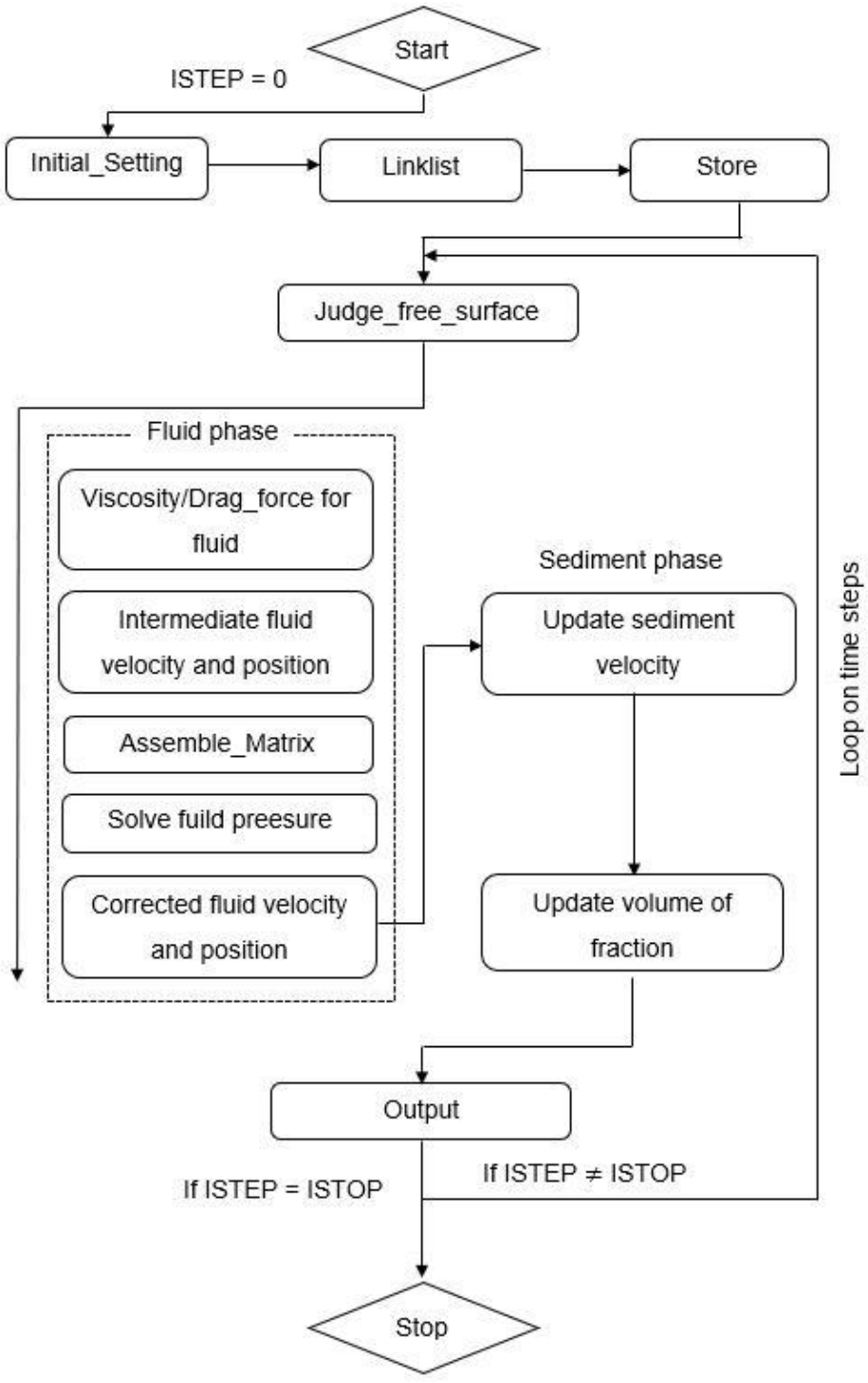

Figure 5.2. The structure of the two-phase ISPH code.

5.6 Validation by idealized problems

This section uses two idealized cases, namely still water with neutrally buoyant sediment and naturally settling sediment, to validate the proposed ISPH model. Numerical results on the static pressure distribution in still water with neutrally buoyant sediment and evolution of sediment concentration with naturally settling sediment are compared with analytical solutions (Shi et al., 2017).

5.6.1 Still water with neutrally buoyant sediment

In order to verify the solution of the pressure field by solving the PPE equation, the proposed ISPH model is applied to the problem of still water with neutrally buoyant sediment. In this section, two test cases, namely Case 1a and Case 1b, are conducted in a two-dimension square tank with the length of sides being $L = 1m$. In Case 1a, evenly distributed particles with the initial distribution of sediment concentration $\alpha_s = 0.1$ is considered; and in Case 1b, the initial distribution of sediment concentration becomes linear along the x_2 axis (vertical direction) and set to be $\alpha_s = 0.5(1 - x_2/L)$. The initial particle spacing is set to be $0.005m$, and the density of both phases is equal to the fluid density $\rho_f = \rho_s = 1000kg/m^3$. The initial particle distribution in the two test cases is shown in Fig. 5.3. The time step Δt is $0.001s$, and the total simulating time is taken as $1.5s$.

In the simulations, the sediment phase will remain suspended, and sediment concentration distribution will keep unchanged. As can be seen from Fig. 5.4, the computed pressure distribution of Case 1a and Case 1b at $t = 1.5s$ has achieved a good agreement with the hydrostatic law in fluid mechanics. Moreover, the particles are uniformly distributed within the entire domain, which further demonstrates the fact that the pressure field is solved precisely without unphysical disorders, which are reported in Shi et al. (2017) with irregular particle distribution and rise of free surface particles.

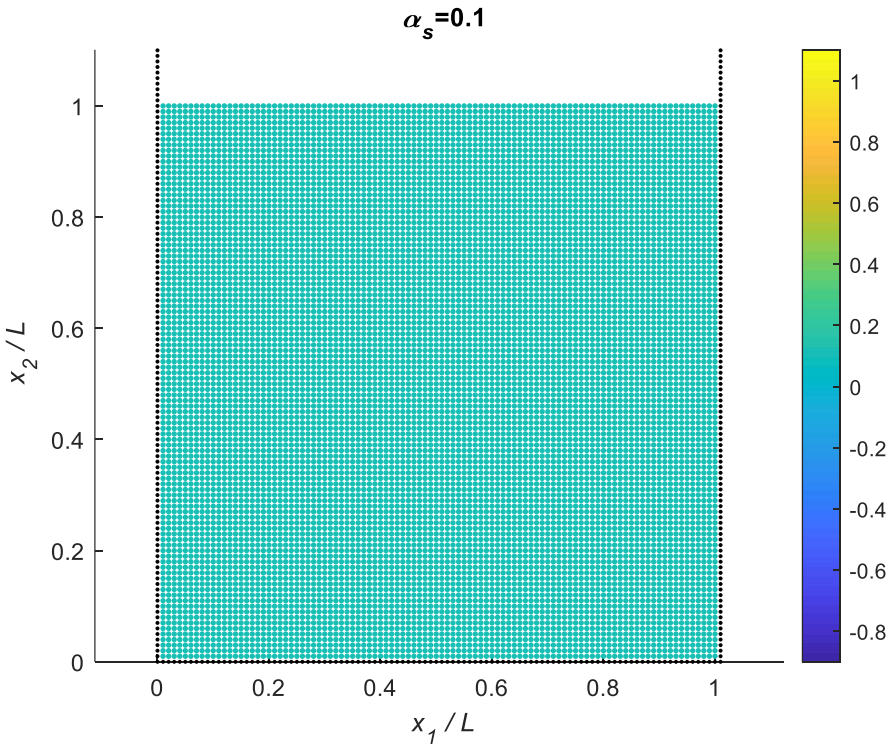

(a)

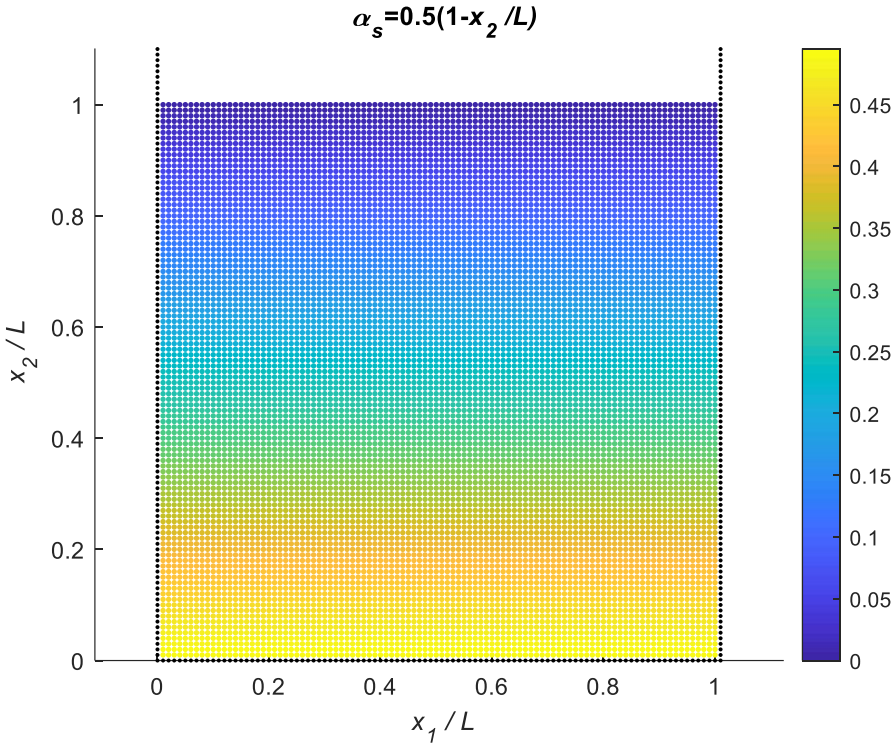

(b)

Figure 5.3. Initial particle distribution and sediment concentration distribution of the test cases (a) Case 1a; (b) Case 1b in still water.

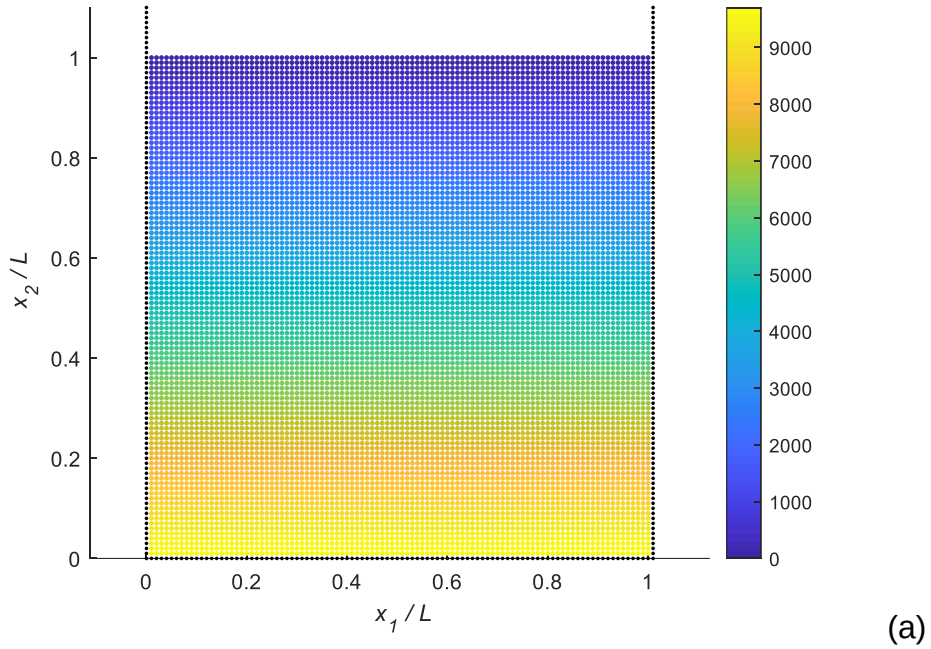

(a)

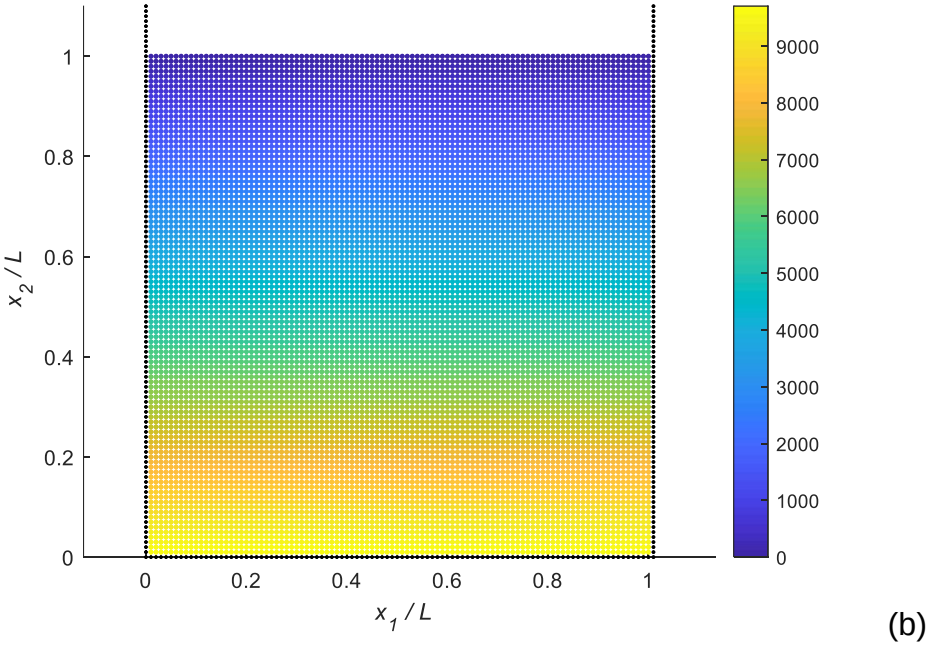

(b)

Figure 5.4. Computed pressure distribution at $t = 1.5s$ of test cases (a) Case 1a; (b) Case 1b.

5.6.2 Still water with naturally settling sediment

Since particles remain suspended for the mixture of fluid and neutrally buoyant sediment, the proposed model will be further verified by the case of still water with naturally settling sediment. The computational domain is defined in a 2-dimensional tank with the length $L = 0.4m$ and depth $H = 0.5m$.

As the sediment concentration in the x_1 direction is uniform, the sediment concentration along the x_2 direction can be expressed as

$$\frac{\partial \alpha_s}{\partial t} - \omega_s (1 - \alpha_s)^{1.65} \frac{\partial \alpha_s}{\partial x_2} = 0 \tag{5.49}$$

where ω_s is the settling velocity of an individual sediment grain; the correction factor $(1 - \alpha_s)^{1.65}$ represents the hindered settling effect (Richardson & Zaki, 1954).

According to Eq. (5.49), the analytical solution can be obtained as

$$\begin{cases} \varphi = x_2 + \omega_s [1 - f(\varphi)]^{1.65} t \\ \alpha_s(t, x_2) = f(\varphi) \end{cases} \tag{5.50}$$

where φ is the coordinate position on x_2 direction and $f(\varphi)$ is the initial sediment concentration at $t = 0s$, which can be defined by

$$\begin{cases} \alpha_s = \dfrac{\alpha_{s0}}{2}\left[1+\cos 2\pi\left(\dfrac{x_2-0.1}{0.4}-0.5\right)\right] & x_2 \geq 0.1 \\ 0 & x_2 < 0.1 \end{cases} \tag{5.51}$$

with $\alpha_{s0} = 0.001$.

In this case, the density is taken as $\rho_f = 1000kg/m^3$ and $\rho_s = 2650kg/m^3$, respectively. The diameter of the sediment is set to be $d_s = 0.15mm$, and yielding a settling velocity of $\omega_s = 1.59cm/s$. The initial particle spacing is $0.01m$, and further investigated with a convergent test for different particle spacing. The time step Δt is $0.001s$. Fig. 5.5 shows the particle distribution and corresponding sediment concentration at $t = 0s$ and $t = 5s$, respectively. The computed pressure field is presented in Fig. 5.6(a) and satisfied with the hydrostatic law as expected. The numerical results of computed sediment concentration at $t = 0s$ and $t = 5s$, as shown in Fig. 5.6(b), are compared with the analytical solution of Eq. (5.50) and achieved a good agreement. In addition, a convergent test with respect to different particle spacing for $\Delta = 5mm, 10mm, 20mm$, $50mm$ and the analytical solution at $t = 5s$ is conducted. As can be seen in Fig.5.7, the numerical error can be minimized by employing finer particle resolution and $\Delta = 10mm$ is good enough in the current simulations.

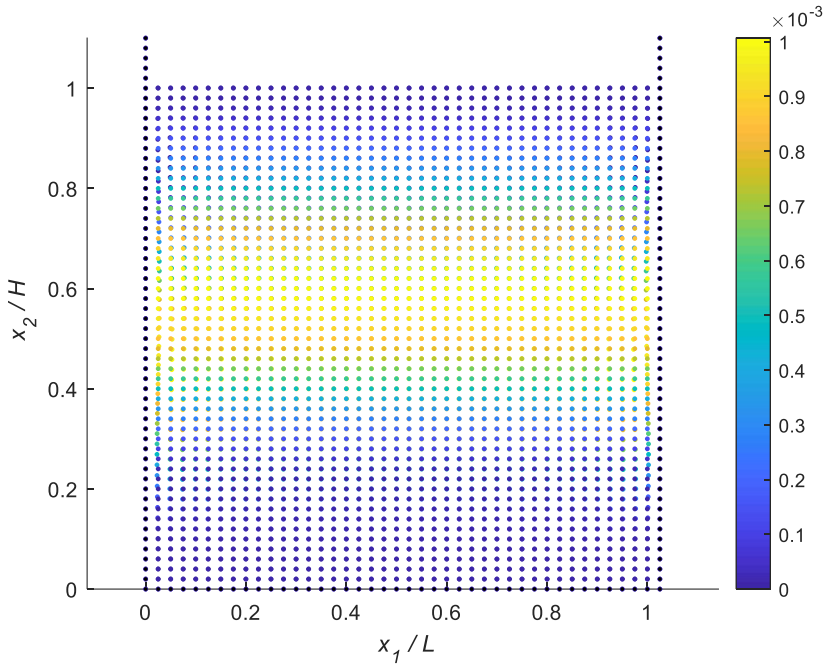

(a)

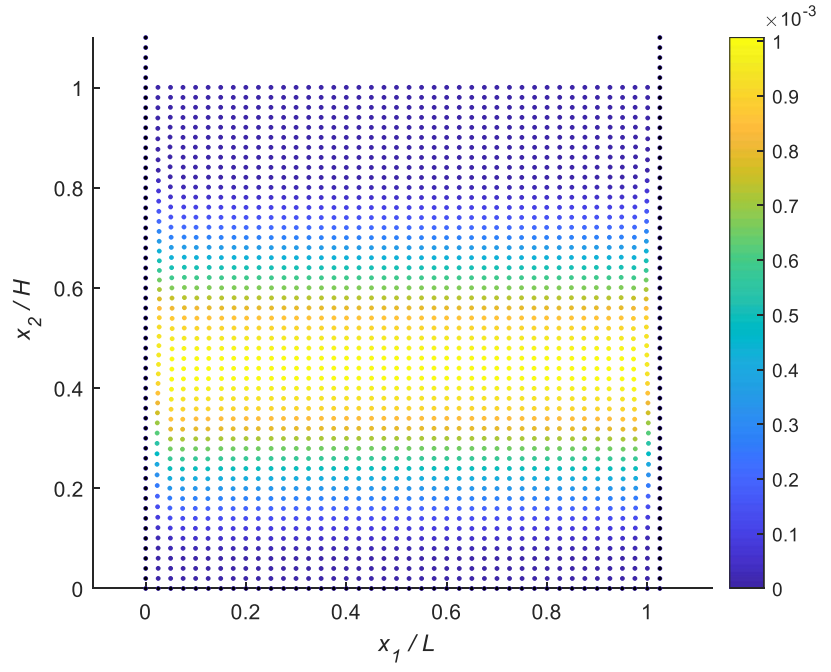

(b)

Figure 5.5. The particle distribution and sediment concentration at (a) $t = 0s$ and (b) $t = 5s$.

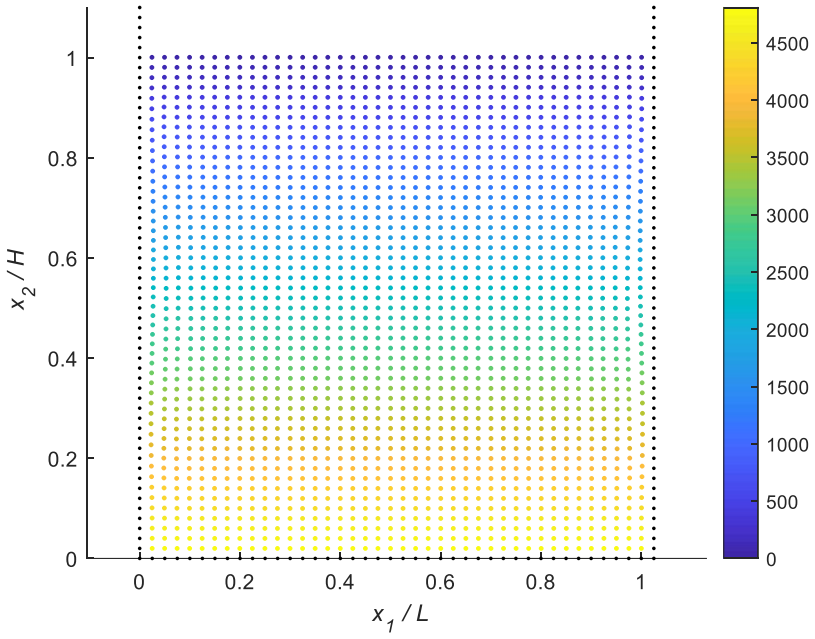

(a)

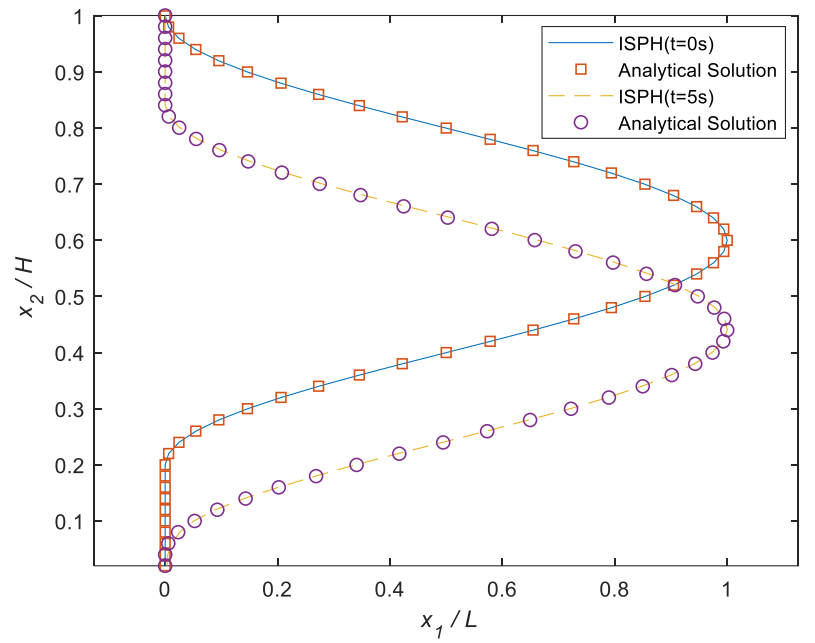

(b)

Figure 5.6. Computed (a) pressure distribution at $t = 5s$; (b) evolution of sediment concentration compared with the analytical solution at $t = 0s$ and $t = 5s$.

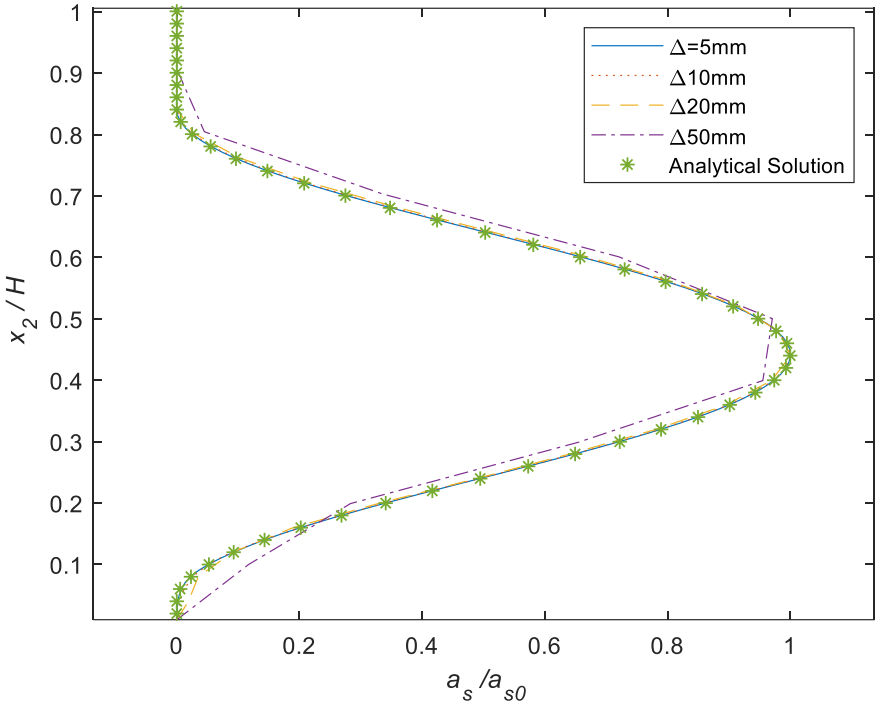

Figure 5.7. Convergent test using the different particle spacing and the analytical solution at $t = 5s$.

5.7 Application to sand dumping

The significance of understanding the settling process of sand has been extensively discussed in the field of estuarine and coastal engineering (Nauyen et al., 2012; Shakibaeinia & Jin, 2012). Therefore, the proposed two-phase ISPH model will be extended to the more practical problem, i.e., sand dumping.

In this section, the proposed two-phase ISPH model is applied to a sand block with $\alpha_{s0} = 0.606$ initially released from the free surface to a $1m \times 1m$ square water tank. The sketch of the computational domain can be seen in Fig. 5.8; H_0 and W_0 is the initial size of the sand block; H and L is the depth and width of the water tank, respectively; Z is the settling distance between the initial sand block position and evolutionary front position of the sand cloud; W is the width of the sand cloud, according to Bühler & Papantoniou (2001), it is defined as the particles with the sediment concentration α_s equal to 5% of the maximum value at the considered instant. The initial particle distribution is shown in Fig. 5.9. The computational domain is represented by 10000 inner particles, including 100 free surface particles with regularly distributed particle spacing $\Delta = 10mm$. The time step is fixed and set to be $\Delta t = 0.001s$.

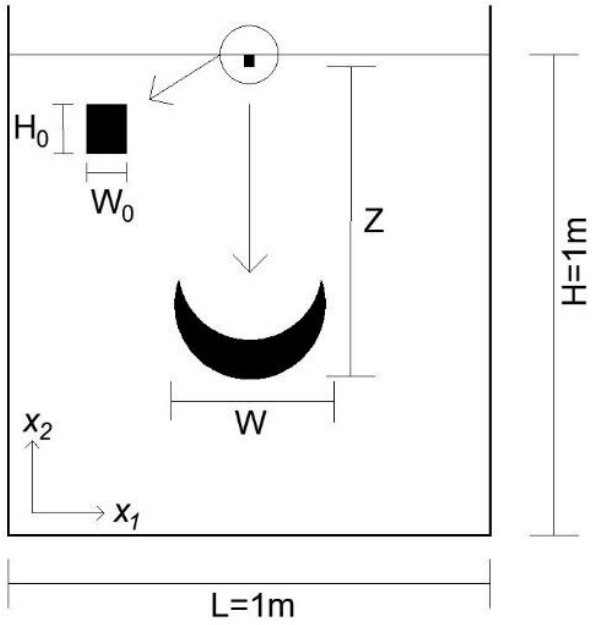

Figure 5.8. Configuration of a water tank with a sand block dumping from the free surface.

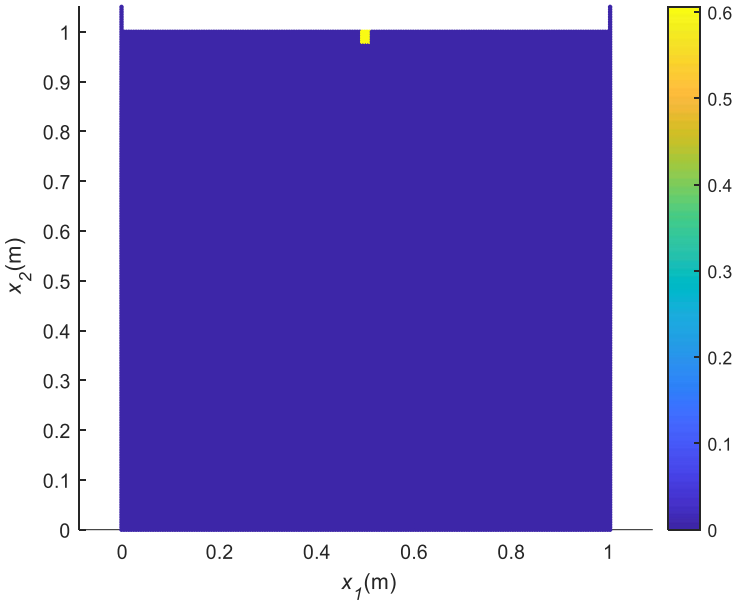

Figure 5.9. Initial particle distribution and sediment concentration.

Table 1 shows the different conditions considered in the sand dumping case, where q_0 is the initial area of the sand block defined as $q_0 = H_0 \times W_0$; the initial density of the sand block $\rho_o = \rho_f(1-\alpha_{s0}) + \rho_s\alpha_{s0} = 2000kg/m^3$ with α_{s0} being the initial sediment concentration; d_s is the sand diameter; the characteristic velocity, $u_0 = \sqrt{(\rho_o - \rho_f)g\sqrt{q_0}/\rho_f}$ and $L_0 = \sqrt{q_0}$.

Table 1 Simulation conditions for test cases

Case	H_0(cm)	W_0(cm)	q_0(cm^2)	d_s(mm)	ω_s(cm/s)	u_0(cm/s)	L_0(cm)
1	2.5	2	5	0.8	12.60	46.81	2.24
2	2.5	2	5	5	49.52	46.81	2.24
3	2.5	4	10	1.3	19.61	55.67	3.16
4	2.5	4	10	5	49.52	55.67	3.16

5.7.1 Motion of sand cloud

The experimental data in Nakasuji et al. (1990) is used for validating the proposed model by comparing it with the computed frontal velocity ω_c and width of the sand cloud W.

Fig. 5.10 shows that the sand cloud accelerates to a constant settling velocity after initial release from the free surface in both Case 1 and Case 2. Despite some wiggles in Fig. 5.10(a), the computed results have achieved a good agreement for both cases in general. According to Shi et al. (2017), the underestimated frontal velocity at the early stage of settling might be caused by the turbulent model, which cannot accurately describe the turbulent effect of fine sand cloud. The proposed model is also validated by comparing the width of the sand cloud with experimental data. Even though minor fluctuations exist, both cases (i.e., Case 3 and 4) can correctly reproduce the satisfactory results In Fig. 5.11. Considering the definition of computed cloud width, the accuracy could be improved by adjusting the measuring method of the cloud width.

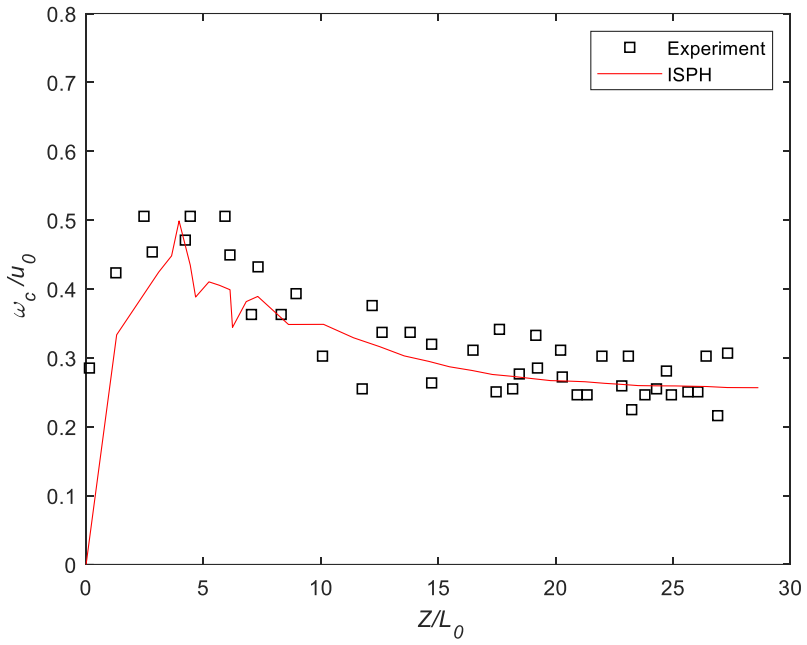

(a)

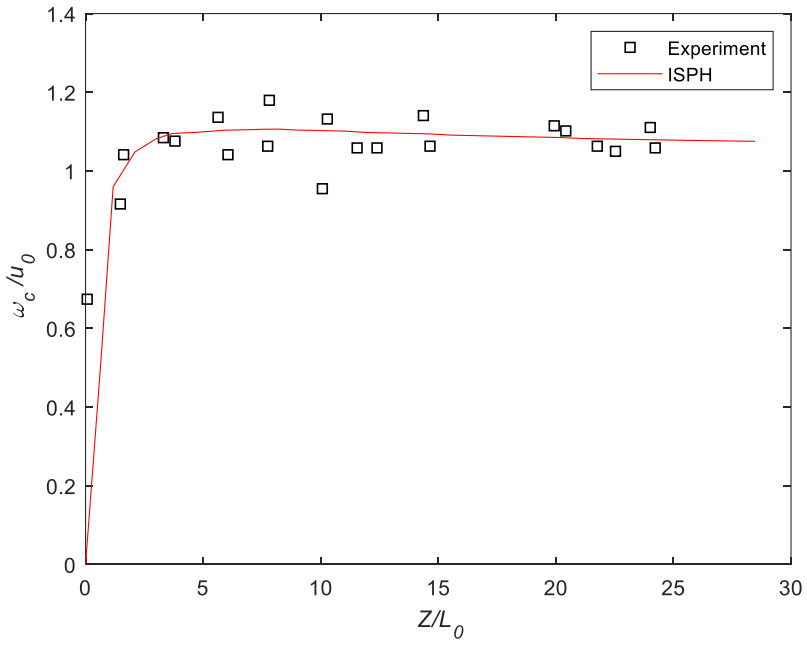

(b)

Figure 5.10 Comparison of the computed frontal velocity ω_c with experimental results of Nakasuji et al. (1990) under conditions of (a) Case 1 and (b) Case 2.

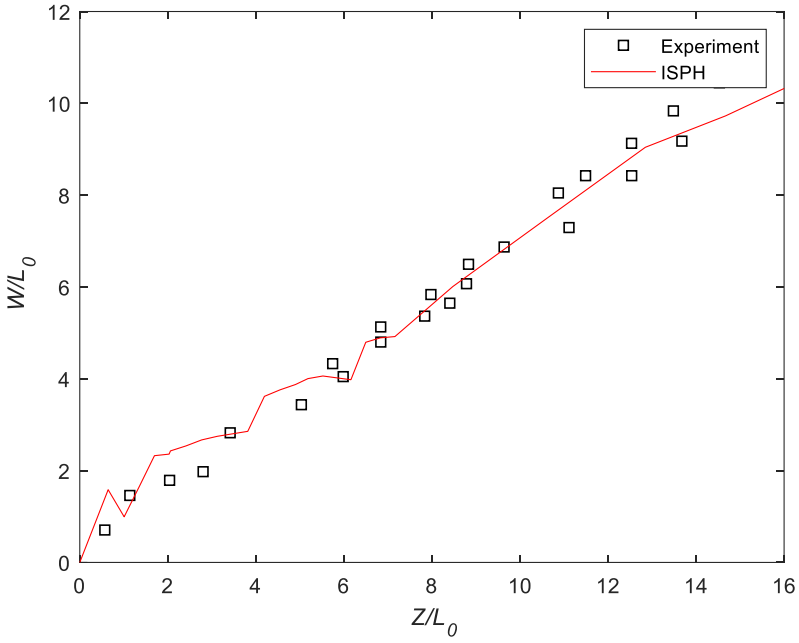

(a)

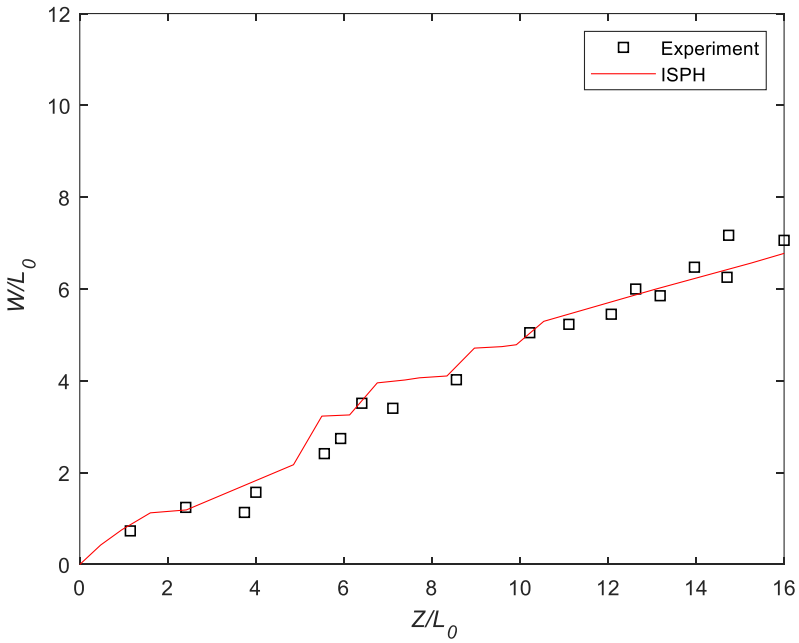

(b)

Figure 5.11. Comparison of the computed cloud width with experimental results of Nakasuji et al. (1990). (a) Case 3; (b) Case 4.

5.7.2 Computed sediment concentration

To supplement the verification of the proposed ISPH model, the computed sediment concentration is performed in Case 1 and Case 2. In Case 1, the computed sediment concentration exhibits two peaks at different instants, as shown in Fig 5.12(a) and Fig. 5.12(b). This double-peak phenomenon is in good agreement with the observed results of Li (1997) and Shi et al. (2017). In Fig. 5.13(a) and Fig. 5.13(b), the double-peak phenomenon disappears in Case 2, which can be explained by the minimized effect of vortices (Li, 1997).

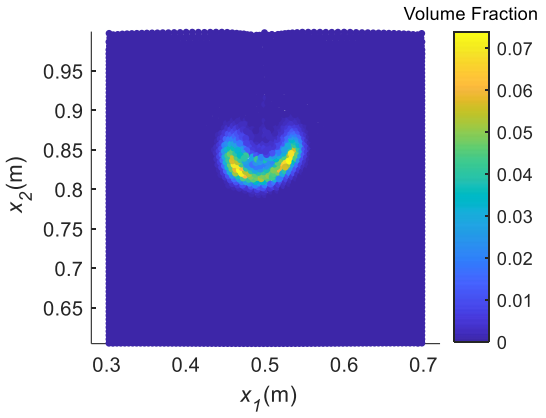

(a)

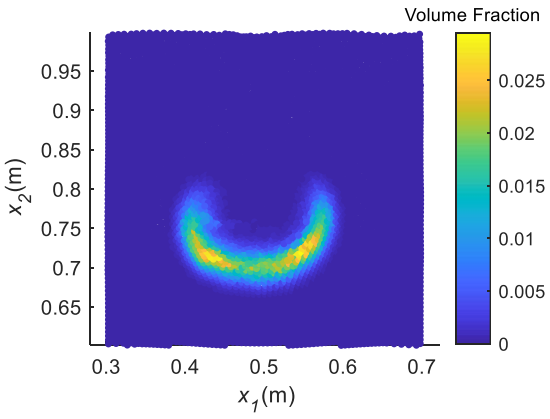

(b)

Figure 5.12. Computed sediment concentration for Case 1 at (a) $t = 1s$ and (b) $t = 2s$.

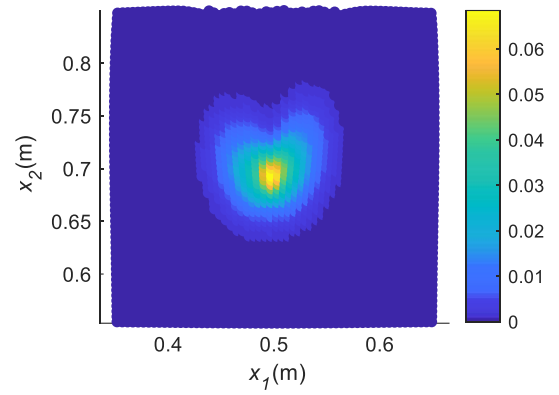

(a)

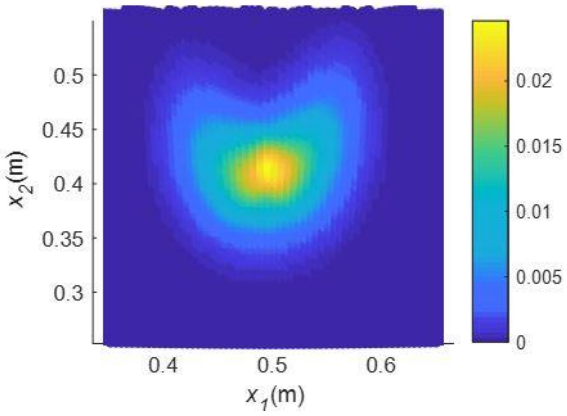

(b)

Figure 5.13. Computed sediment concentration for Case 2 at (a) $t = 1s$ and (b) $t = 2s$.

5.7.3 Computed fields of pressure and vortices

In this section, the computed fields of pressure and vortices in Case 2 are performed to verify the motion of the sand cloud. The computed pressure field at $t = 1s$ is shown in Fig. 5.14. It demonstrates that the pressure field is continuous within the computational domain and generally agrees with the hydrostatic law.

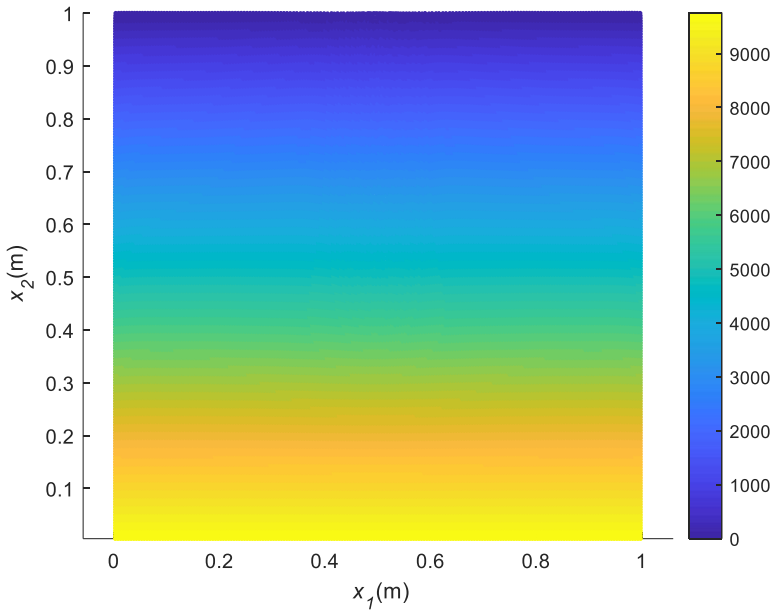

Figure 5.14. Computed pressure field at $t = 1s$ for Case 2.

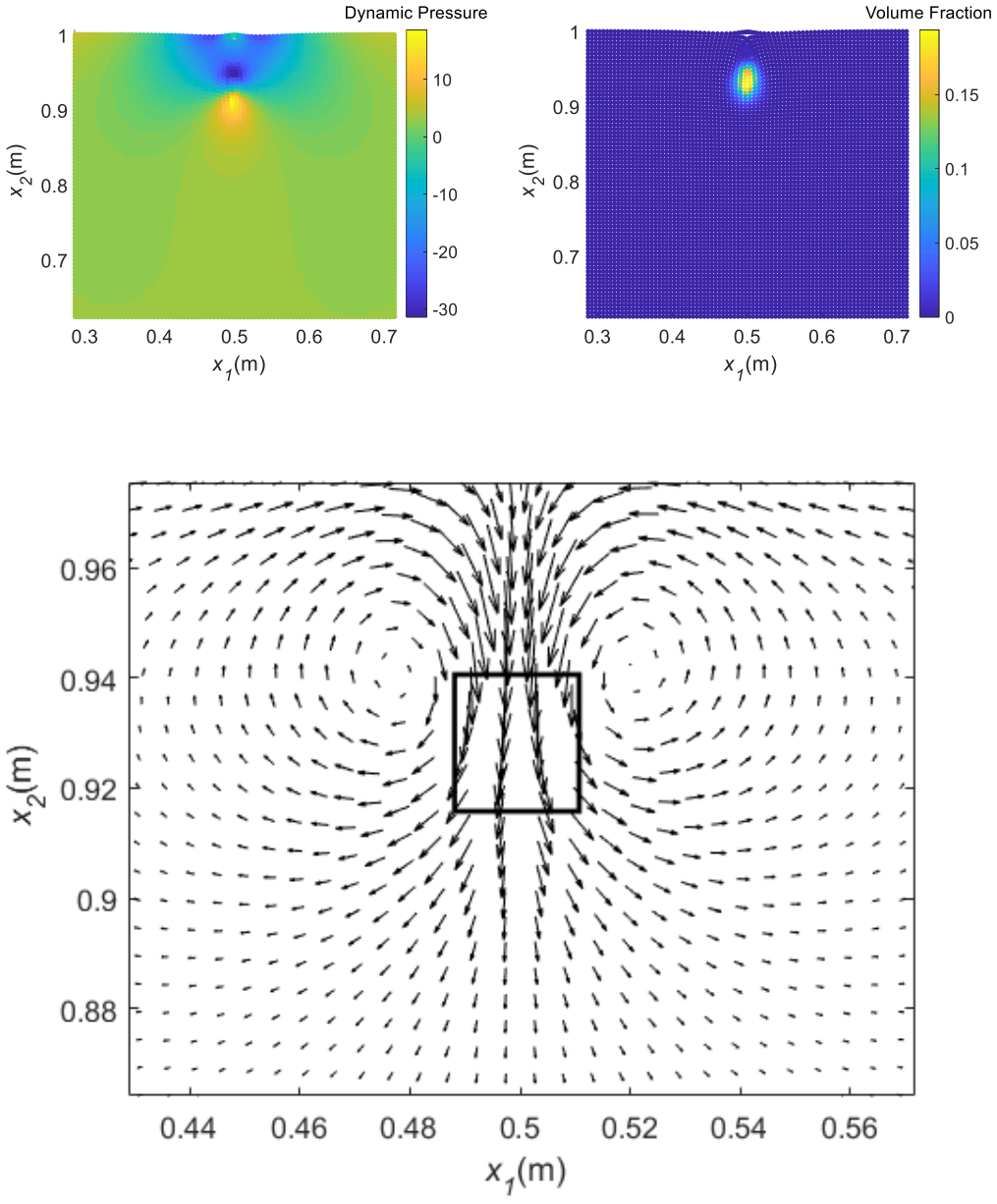

(a) Computed fields of dynamic pressure, the volume fraction of sediment and vortices (the solid line box indicates the position of sand cloud) at $t = 0.25s$ for Case 2.

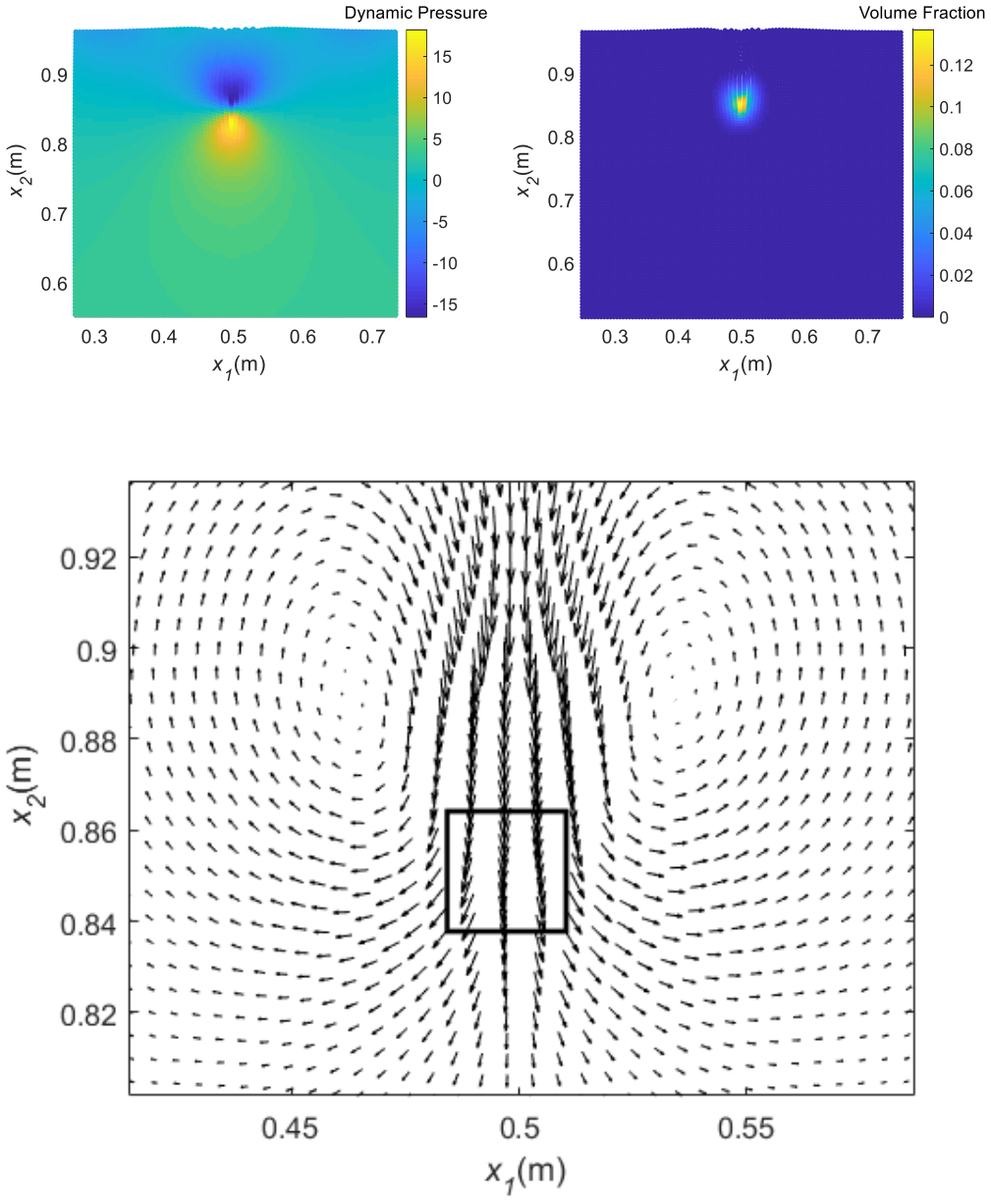

(b) Computed fields of dynamic pressure, the volume fraction of sediment and vortices (the solid line box indicates the position of sand cloud) at $t = 0.5s$ for Case 2.

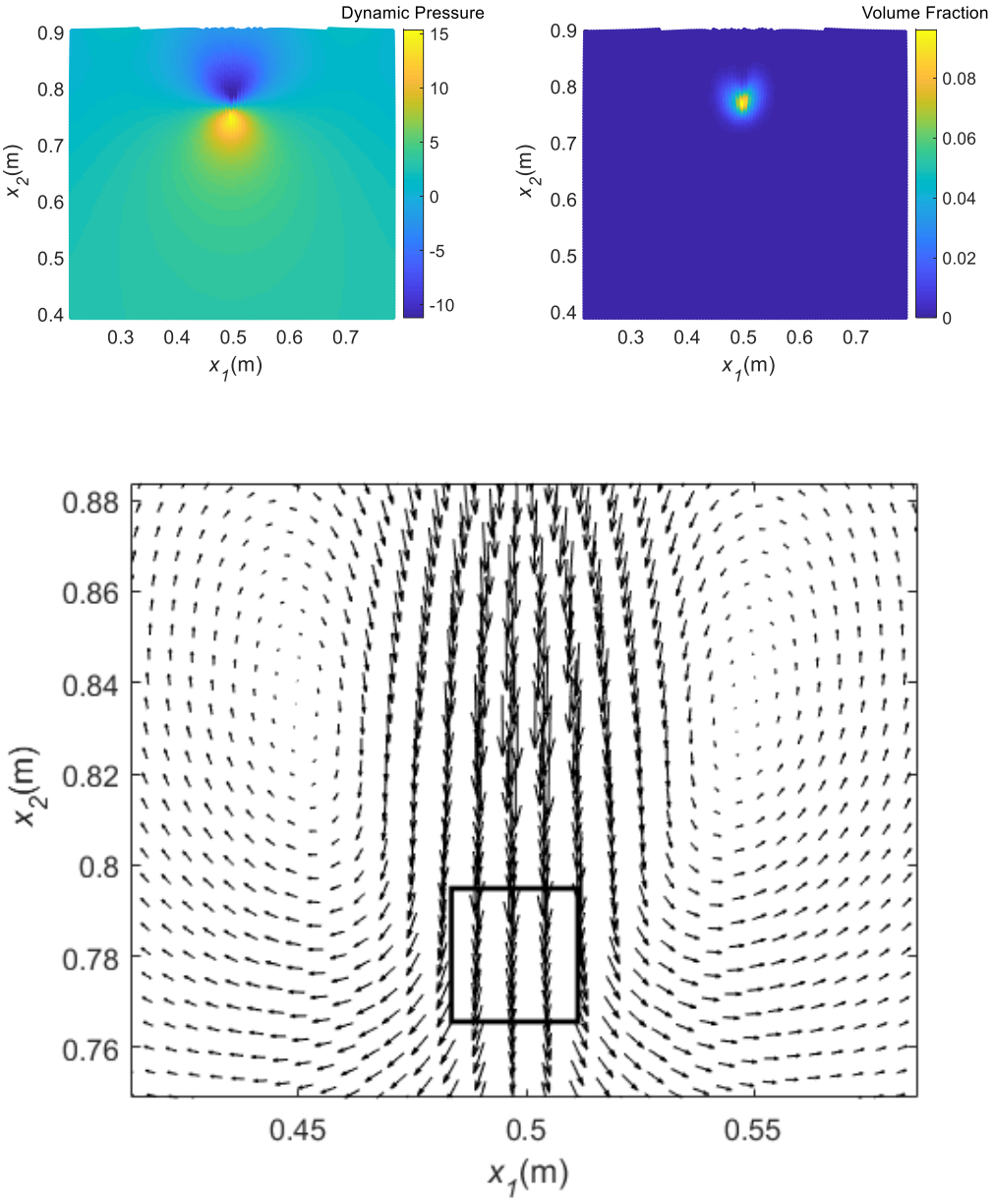

(c) Computed fields of dynamic pressure, the volume fraction of sediment and vortices (the solid line box indicates the position of sand cloud) at $t = 0.75s$ for Case 2.

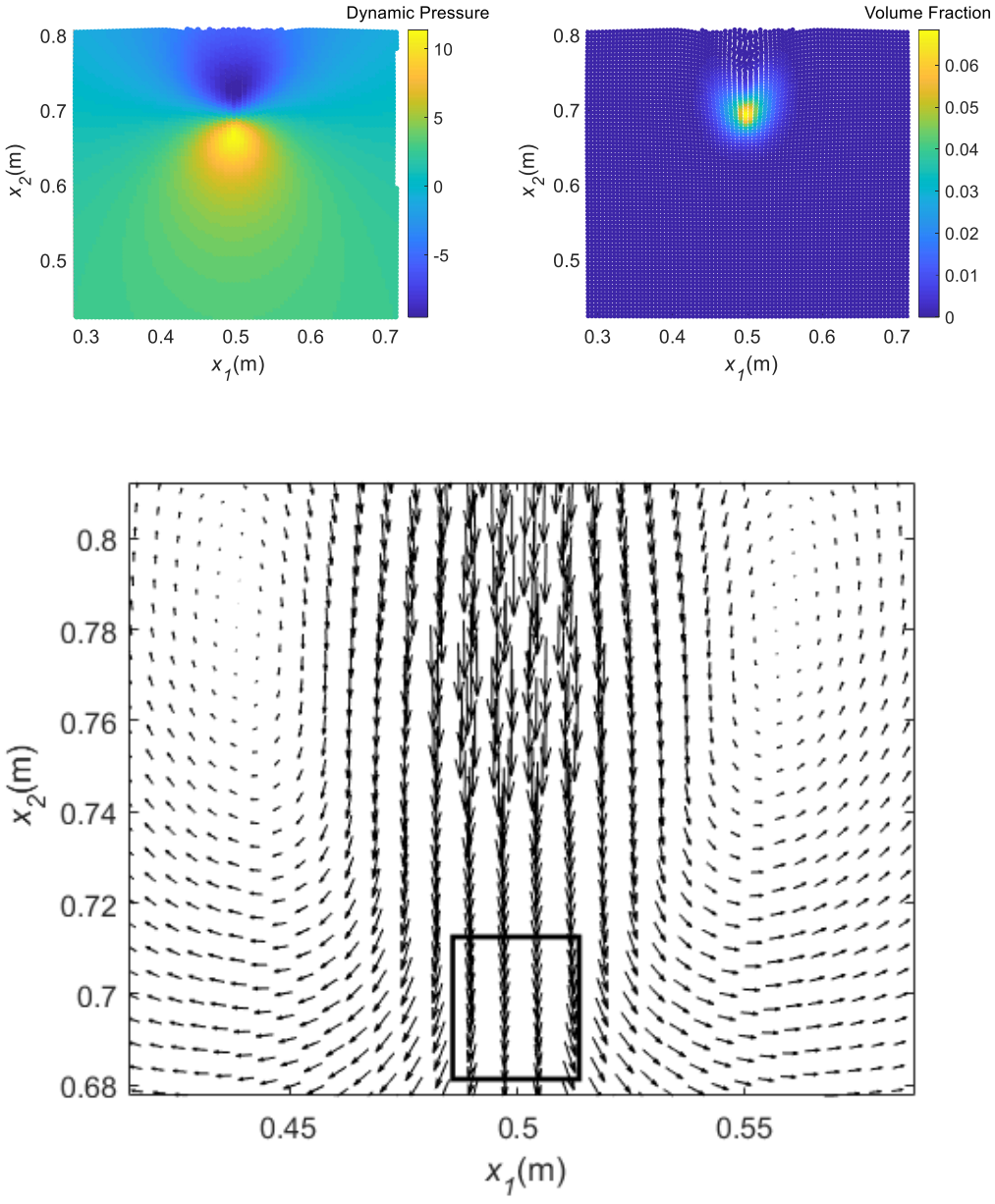

(d) Computed fields of dynamic pressure, the volume fraction of sediment and vortices (the solid line box indicates the position of sand cloud) at $t = 1s$ for Case 2.

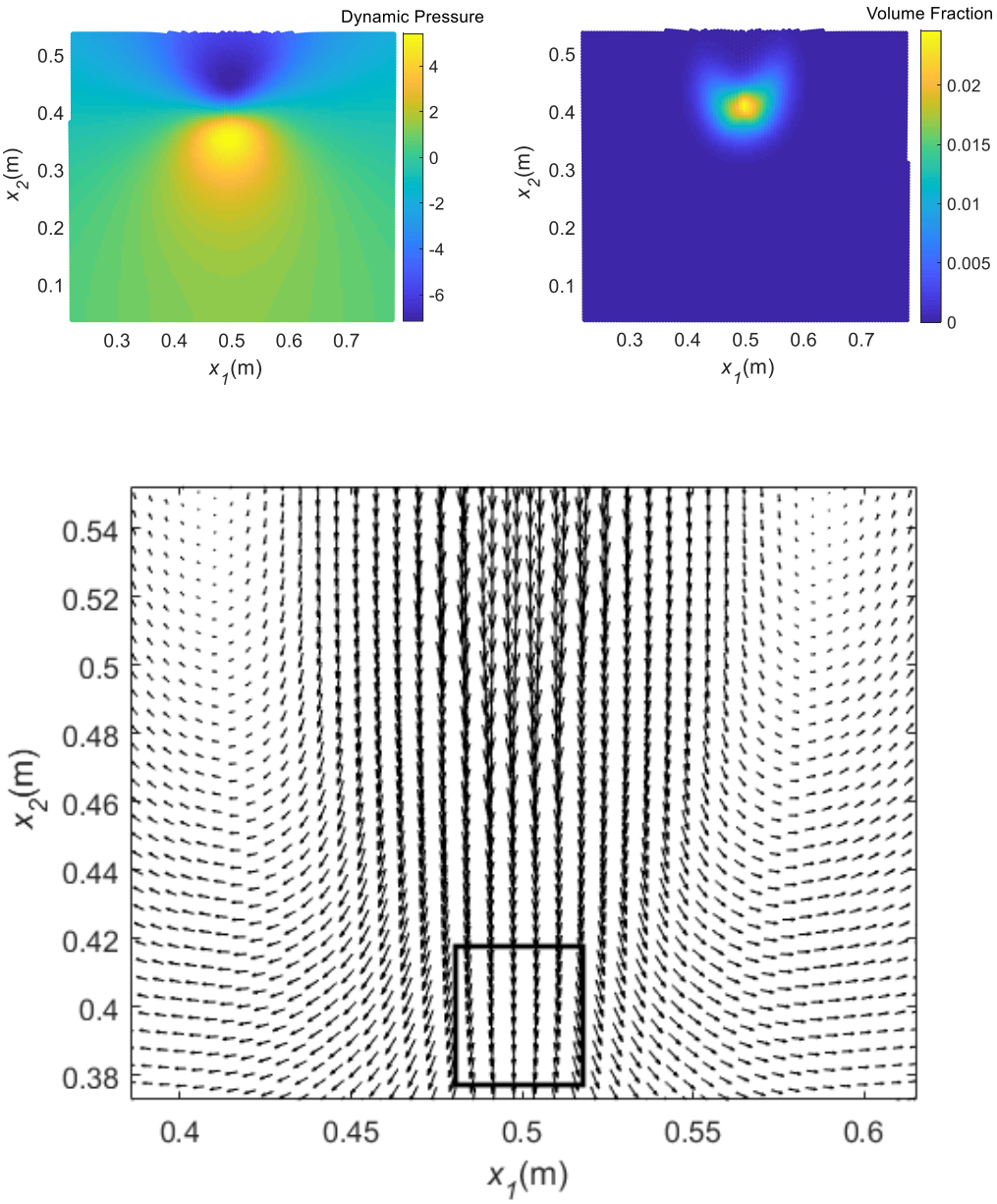

(e) Computed fields of dynamic pressure, the volume fraction of sediment and vortices (the solid line box indicates the position of sand cloud) at $t = 2s$ for Case 2.

Figure 5.15. Computed fields of dynamic pressure, the volume fraction of sediment and vortices at different instants (a) $t = 0.25s$, (b) $t = 0.5s$, (c) $t = 0.75s$ (d) $t = 1s$, (e) $t = 2s$ for Case 2.

Figs. 5.15(a) to 5.15(e) show the computed dynamic pressure, sediment concentration, and vortex field at different instants from $t = 0.25s$ to $t = 2s$ for Case 2. It is clear that there exists a high-pressure zone below the front of the sand cloud, which drives the sediment to spread out during the process of settling. In Fig. 5.15(a), the position of sand cloud is located between two symmetrical vortices, and the pair of vertices can directly affect its motion. In Figs. 5.15(b) to 5.15(e), it is clear that the sand cloud is moving away from the vortices. Since the sand cloud is less affected by vortices in Case 2, it explains why the double-peak phenomenon appears in Case 1 but disappears in Case 2, as noted in Section 5.7.2. In brief, the sediment in Case 2 can move away from the vortex centre before the vortex can directly affect the movement of the sand cloud.

5.8 Conclusion

The present study proposes a two-phase model based on the incompressible SPH method for simulating sediment motion problems. The fluid and sediment phases are treated as two miscible fluids, and the computational domain is discretized into a single set of SPH particles. Each SPH particle moves with the fluid velocity and carries the local properties of both phases. The drag force is formulated with consideration of the hindered effect. In addition, large eddy simulation (LES) is employed to represent the turbulent effect, and the eddy viscosities are defined by the Smagorinsky model. The classic two-step prediction-correction procedure is used to solve the pressure Poisson equation under the incompressible conditions for fluid and sediment phases. The pressure Neumann boundary condition is imposed on the rigid solid walls, as the zero pressure boundary

condition on the free water surface. In the implementation, the Fortran code package based on the Visual Studio platform is newly developed.

The two-phase model is verified by the analytical solutions for two idealized problems of still water with neutrally buoyant sediment and naturally settling sediment in a two-dimensional water tank. The numerical results have clearly agreed with the analytical solutions for both problems. The convergent test for a range of initial particle spacing is also conducted. In the sand dumping case, the proposed model is validated by comparing the motion of sand clouds (i.e., the frontal velocity and width) with experimental results. It is shown that the numerical results are in good agreement with experimental data. The model is then applied to explore the evolution of sand concentration. In the fine sediment case (i.e., Case 1), the double-peak phenomenon appears because of the effect of vortices. However, in Case 2 with coarse sediment, the impact of vortices is weakened. This is because the sand cloud moves away from the vortex centre before it is fully developed. In summary, the newly developed two-phase model based on incompressible SPH method is proven to be effective for the numerical study of sand dumping problems.

Chapter 6: Conclusions and future work

In this thesis, two numerical improvements have been proposed and incorporated into code implementations. Specifically, an improved boundary scheme based on the MLPG_R method is developed to impose rigid and impermeable boundary conditions. A two-phase model based on the incompressible SPH method is proposed for simulating sediment motion problems. This thesis starts with a brief introduction of the background of developing meshless methods. Then, the literature review chapter presents some recent developments of meshless methods (i.e., MLPG and SPH specifically), boundary treatment methods and multiphase flow modelling. Next, the fundamental modelling principles and formulations of the MLPG_R and SPH methods are described in the methodology chapter. The conclusion and discussion of the newly developed numerical improvements are shown below.

6.1 The improved boundary scheme

For simulating flow-structure interaction problems, this work develops an improved boundary scheme for rigid and impermeable walls by integrating the PPE for wall boundary particles with the Neumann pressure boundary condition imposed. This numerical improvement based on the MLPG_R method removes the calculation of derivatives of the unknown pressure. Accordingly, improved computational accuracy is reported through validation of patch tests and comparison with other numerical results (i.e., the direct discretization of the pressure Neumann boundary condition). The current boundary scheme shows a good capacity to deal with randomly

distributed particles. Apart from the reduction of mean error, the number of particles having large errors is also reduced, thus enhancing the stability of the simulation. In the classic lid-driven cavity cases, the velocity fields simulated by the model with the new boundary scheme has achieved good agreement with those by the well-established numerical method across a wide range of Reynolds number. In the simulation of flow over a cylinder, the new boundary scheme is applied to the curved surface of the cylinder. The convergent results to various particle numbers show the capacity of the new scheme to deal with non-flat geometries. Moreover, the development of symmetrical vortex and its length at low Reynolds number and asymmetrical vortex at high Reynolds number are all well captured compared with measurements. The capability of the new boundary approach is also validated for the moving boundary by generating monochromic waves using a piston wavemaker as the wave surface profiles well agree with the analytical solutions.

6.2 The two-phase ISPH model

A two-phase ISPH model is proposed in the present study for simulating sediment motion problems. The formulation of this two-phase model treats the fluid and sediment phases as two miscible fluids. The computational domain is discretized into a single set of SPH particles that move with the water velocity. Turbulent and hindered settling effects are also considered. The pressure field is solved by employing the two-step prediction-correction procedure. This two-phase model is firstly verified by two idealized problems, and the numerical results have clearly agreed with the analytical solutions. A convergent test for a range of initial particle spacing is also

conducted. In the sand dumping simulations, the proposed model demonstrates that the numerical results are in good agreement with experimental data regarding the motion of sand cloud (i.e., frontal velocity and width). The model is also applied to explore the evolution of sand concentration, and it is shown that the existence of vortices can cause the double-peak distribution of the sediment concentration. Furthermore, the double-peak distribution phenomenon disappears as the settling velocity is large enough to move away from the vortex centre. Overall, the developed two-phase model based on incompressible SPH method is proven to be effective for the numerical study of sand dumping problems.

6.3 Future work

This research has explored a number of potential avenues for future research:

- The current boundary treatment schemes in MLPG are mainly applied to the flat boundary. With this regard, imposing boundary conditions on more complex geometries is important in practical engineering applications.

- In order to accurately calculate the second or higher order of derivatives, an improved interpolation scheme is required for particles near the boundaries with a truncated support domain. This also plays a significant role in terms of computational stability.

- In this work, the assumption of a semi-circular domain at the boundary particles works well. However, this sub-domain may reduce to a quarter-circle near the intersection of free surface and rigid boundaries. It is questionable if such a truncated domain can provide a robust solution in corners or 3-dimensional cases.

- A common issue in meshless methods applied to incompressible fluid flow simulations is the uneven distribution of particles. Although some numerical techniques such as the swift position method have been proposed, a robust solution is still needed to handle the regularization of the particles during the time loop.

- For multiphase simulation, the proposed two-phase SPH model needs to be verified with further practical scenarios with various density ratios considering the hindered settling effect.

- The discussion on the time step and corresponding conditions is unclear for multiphase flow simulations. More tests are required to explore the restrictions of the maximum time step for improving computational effectiveness.

- The present model has not considered the scenario when settling materials approaches and distributes on the bottom. This might be oversimplified concerning adaptability.

- Regarding the fluid-sediment interphase forces, only the drag forces are considered, and it is unclear if other forces should be included.

- In this thesis, the improved boundary scheme and two-phase model are both applied to 2-dimensional simulations. In future work, it is worth exploring their extension to 3-dimensional cases.

- The codes developed in this work are highly customized. With this respect, the universal open-source codes could be helpful for improving and understanding the present numerical schemes.

- The possibility of extending the improved boundary scheme based on MLPG to ISPH is worth exploring. Besides, the two-phase ISPH model also has the potential to be implemented based on the MLPG formulations.

- As the governing equations and numerical procedure of ISPH and MLPG_R remain the same, it is worth exploring the application of the MLPG_R method to the multiphase problems.

References

Agarwal, S., Sriram, V., Yan, S., & Murali, K. (2021). Improvements in MLPG formulation for 3D wave interaction with fixed structures. *Computers & Fluids*, *218*, 104826.

Anderson, J. D., & Wendt, J. (1995). *Computational fluid dynamics* (Vol. 206, p. 332). New York: McGraw-Hill.

Atluri, S. N., Kim, H. G., & Cho, J. Y. (1999). A critical assessment of the truly meshless local Petrov-Galerkin (MLPG), and local boundary integral equation (LBIE) methods. *Computational mechanics*, *24*(5), 348-372.

Atluri, S. N., & Shen, S. (2002). *The meshless method*. Encino, CA: Tech Science Press.

Atluri, S. N., & Zhu, T. (1998). A new meshless local Petrov-Galerkin (MLPG) approach in computational mechanics. *Computational mechanics*, *22*(2), 117-127.

Balachandar, S., & Eaton, J. K. (2010). Turbulent dispersed multiphase flow. *Annual Review of Fluid Mechanics*, *42*, 111–133.

Basic, J., Degiuli, N., & Ban, D. (2018). A class of renormalised meshless Laplacians for boundary value problems. *Journal of Computational Physics*, *354*, 269-287.

Beall, M. W., Walsh, J., & Shephard, M. S. (2004). A comparison of techniques for geometry access related to mesh generation. *Engineering with Computers*, *20*(3), 210-221.

Belytschko, T., Lu, Y. Y. & Gu, L. (1994). Element-free Galerkin methods. *International journal for numerical methods in engineering*, *37*(2), 229-256.

Bhatti, M. M., Marin, M., Zeeshan, A., & Abdelsalam, S. I. (2020). Recent trends in computational fluid dynamics. *Frontiers in Physics*, 453.

Bierbrauer, F., Bollada, P. C., & Phillips, T. N. (2009). A consistent reflected image particle approach to the treatment of boundary conditions in smoothed particle hydrodynamics. *Computer Methods in Applied Mechanics and Engineering*, *198*(41-44), 3400-3410.

Blottner, F. G. (1964). Nonequilibrium laminar boundary-layer flow of ionized air. *Aiaa Journal*, *2*(11), 1921-1927.

Boddula, S., & Eldho, T. I. (2017). A moving least squares based meshless local petrov-galerkin method for the simulation of contaminant transport in porous media. *Engineering Analysis with Boundary Elements*, *78*, 8-19.

Bonet, J., & Kulasegaram, S. (2000). Correction and stabilization of smooth particle hydrodynamics methods with applications in metal forming simulations. *International journal for numerical methods in engineering*, *47*(6), 1189-1214.

Bonet, J., & Kulasegaram, S. (2002). A simplified approach to enhance the performance of smooth particle hydrodynamics methods. *Applied Mathematics and Computation*, *126*(2-3), 133-155.

Bouré, J. A. (1987). Two-phase flow models: The closure issue. *Multiphase science and technology*, *3*(1-4).

Brennen, C. E. (2014). Introduction to Multiphase Flow. *Fundamentals of Multiphase Flow*, 1–29.

Bühler, J., & Papantoniou, D. A. (2001). On the motion of suspension thermals and particle swarms*. Journal of Hydraulic Research, 39*(6), 643–653.

Chaniotis, A. K., Poulikakos, D., & Koumoutsakos, P. (2002). Remeshed smoothed particle hydrodynamics for the simulation of viscous and heat conducting flows. *Journal of Computational Physics*, *182*(1), 67-90.

Chapman, D. R. (1979). Computational aerodynamics development and outlook. *AIAA journal*, *17*(12), 1293-1313.

Chen, F. (2020). Meshfree simulation of multiphase flows with SPH family methods. *arXiv preprint arXiv:2010.12189*.

Chen, J. K., Beraun, J. E., & Carney, T. C. (1999). A corrective smoothed particle method for boundary value problems in heat conduction. *International Journal for Numerical Methods in Engineering*, *46*(2), 231-252.

Chen, J. S., Pan, C., Wu, C. T., & Liu, W. K. (1996). Reproducing kernel particle methods for large deformation analysis of non-linear structures. *Computer methods in applied mechanics and engineering*, *139*(1-4), 195-227.

Chen, L. F., Zang, J., Hillis, A. J., Morgan, G. C., & Plummer, A. R. (2014). Numerical investigation of wave–structure interaction using OpenFOAM. *Ocean Engineering*, *88*, 91-109.

Chen, X., Li, Y., Niu, X., Chen, D., & Yu, X. (2011). A two-phase approach to wave-induced sediment transport under sheet flow conditions. *Coastal Engineering*, 58(11), 1072–1088.

Chen, X., & Wang, J. (2014). A comparison of two-fluid model, dense discrete particle model and CFD-DEM method for modeling impinging gas-solid flows. *Powder Technology*, *254*, 94–102.

Chien, N., & Wan, Z. (1999, June). Mechanics of sediment transport. American Society of Civil Engineers.

Chorin, A. J. (1968). Numerical solution of the Navier-Stokes equations. *Mathematics of computation*, *22*(104), 745-762.

Colagrossi, A., Antuono, M., & Le Touzé, D. (2009). Theoretical considerations on the free-surface role in the smoothed-particle-hydrodynamics model. *Physical Review E - Statistical, Nonlinear, and Soft Matter Physics*, *79*(5), 1–13.

Cummins, S.J., & Rudman, M., (1999). An SPH projection method. *Journal of computational physics*, *152*(2), pp.584-607.

Dalrymple, R. A., & Rogers, B. D. (2006). Numerical modeling of water waves with the SPH method. *Coastal Engineering*, *53*(2–3), 141–147.

Davidson-Arnott, R., Bauer, B., & Houser, C. (2019). *Introduction to coastal processes and geomorphology*. Cambridge university press.

De Jong, J. F., Dang, T. Y. N., van Sint Annaland, M., & Kuipers, J. A. M. (2012). Comparison of a discrete particle model and a two-fluid model to experiments of a fluidized bed with flat membranes. *Powder technology*, *230*, 93-105.

De Moura, C. A., & Kubrusly, C. S. (2013). The courant–friedrichs–lewy (cfl) condition. *AMC*, *10*(12).

Deen, N. G., Annaland, M. V. S., Van der Hoef, M. A., & Kuipers, J. A. M. (2007). Review of discrete particle modeling of fluidized beds. *Chemical engineering science*, *62*(1-2), 28-44.

Delhaye, J. M. (1978). Instantaneous space-averaged equations. *In Von Karman Inst. for Fluid Dyn. Two-Phase Flows in Nucl. Reactors*, *1*.

Delnoij, E., Lammers, F. A., Kuipers, J. A. M., & van Swaaij, W. P. M. (1997). Dynamic simulation of dispersed gas-liquid two-phase flow using a discrete bubble model. *Chemical engineering science*, *52*(9), 1429-1458.

Dibajnia, M., & Watanabe, A. (1998). Transport rate under irregular sheet flow conditions. *Coastal Engineering*, *35*(3), 167-183.

Dilts, G. A. (1999). Moving-least-squares-particle hydrodynamics—I. Consistency and stability. *International Journal for Numerical Methods in Engineering*, *44*(8), 1115-1155.

Divya, R., Sriram, V., & Murali, K. (2020). Wave-vegetation interaction using Improved Meshless Local Petrov Galerkin method. *Applied Ocean Research*, *101*, 102116.

Drake, T. G., & Calantoni, J. (2001). Discrete particle model for sheet flow sediment transport in the nearshore. *Journal of Geophysical Research: Oceans*, *106*(C9), 19859-19868.

Dohmen-Janssen, C. M., & Hanes, D. M. (2002). Sheet flow dynamics under monochro-maticmatic nonbreaking waves. *Journal of Geophysical Research, 107*(C10), 1–21.

Dong, P., & Zhang, K. (1999). Two-phase flow modelling of sediment motions in oscillatory sheet flow. *Coastal Engineering*, *36*(2), 87–109.

Dong, P., & Zhang, K. (2002). Intense near-bed sediment motions in waves and currents. *Coastal Engineering*, *45*(2), 75-87.

Drew, D. A. (1983). Mathematical modeling of two-phase flow. *Annual review of fluid mechanics*, *15*(1), 261-291.

Drew, D. A., & Segel, L. A. (1971). Averaged equations for two-phase flows. *Studies in Applied Mathematics*, *50*(3), 205-231.

Dronkers, J. (2005). *Dynamics of coastal systems* (Vol. 25). World Scientific.

Dyer, K. R. (1995). Sediment transport processes in estuaries. In *Developments in Sedimentology* (Vol. 53, pp. 423-449). Elsevier.

Eatock Taylor, R., Wang, B. T., & Wu, G. X. (1994). On the transient analysis of the wavemaker. In *9th International Workshop on Water Waves and Floating Bodies, Kuju, Oita, Japan*.

Einstein, H. A. (1950). *The bed-load function for sediment transportation in open channel flows* (No. 1026). US Government Printing Office.

Fang, J., Owens, R. G., Tacher, L., & Parriaux, A. (2006). A numerical study of the SPH method for simulating transient viscoelastic free surface flows. *Journal of non-newtonian fluid mechanics*, *139*(1-2), 68-84.

Fay, J. A., & Riddell, F. R. (1958). Theory of stagnation point heat transfer in dissociated air. *Journal of the Aerospace Sciences*, *25*(2), 73-85.

Ferrand, M., Laurence, D. R., Rogers, B. D., Violeau, D., & Kassiotis, C. (2013). Unified semi-analytical wall boundary conditions for inviscid, laminar or turbulent flows in the meshless SPH method. *International Journal for Numerical Methods in Fluids*, *71*(4), 446-472.

Finn, J. R., Li, M., & Apte, S. V. (2016). Particle based modelling and simulation of natural sand dynamics in the wave bottom boundary layer. *Journal of Fluid Mechanics, 796*, 340–385.

Fonty, T., Ferrand, M., Leroy, A., Joly, A., & Violeau, D. (2019). Mixture model for two-phase flows with high density ratios: A conservative and realizable SPH formulation. *International Journal of Multiphase Flow*, *111*, 158–174.

Fourtakas, G., Dominguez, J. M., Vacondio, R., & Rogers, B. D. (2019). Local uniform stencil (LUST) boundary condition for arbitrary 3-D

boundaries in parallel smoothed particle hydrodynamics (SPH) models. *Computers & Fluids*, *190*, 346-361.

Fourtakas, G., & Rogers, B. D. (2016). Modelling multi-phase liquid-sediment scour and resuspension induced by rapid flows using Smoothed Particle Hydrodynamics (SPH) accelerated with a Graphics Processing Unit (GPU). *Advances in Water Resources*, *92*, 186–199.

Fraga Filho, C. A. D., Schuina, L. L., & Porto, B. S. (2020). An investigation into neighbouring search techniques in meshfree particle methods: an evaluation of the neighbour lists and the direct search. *Archives of Computational Methods in Engineering*, *27*(4), 1093-1107.

Ghia, U. K. N. G., Ghia, K. N., & Shin, C. T. (1982). High-Re solutions for incompressible flow using the Navier-Stokes equations and a multigrid method. *Journal of computational physics*, *48*(3), 387-411.

Gidaspow, D. (1994). *Multiphase flow and fluidization: continuum and kinetic theory descriptions*. Academic press.

Gingold, R. A., & Monaghan, J. J. (1977). Smoothed particle hydrodynamics: theory and application to non-spherical stars. *Monthly notices of the royal astronomical society*, *181*(3), 375-389.

Godino, D. M., Corzo, S. F., & Ramajo, D. E. (2020). Two-phase modeling of water-air flow of dispersed and segregated flows. *Annals of Nuclear Energy*, *149*, 107766.

Gómez-Gesteira, M., & Dalrymple, R. A. (2004). Using a three-dimensional smoothed particle hydrodynamics method for wave impact on a tall structure. *Journal of waterway, port, coastal, and ocean engineering*, *130*(2), 63-69.

Gómez-Gesteira, M., Rogers, B. D., Violeau, D., Grassa, J. M., & Crespo, A. J. (2010). Foreword: SPH for free-surface flows. *Journal of Hydraulic Research*, *48*(sup1), 3-5.

Gong, K., Liu, H., & Wang, B. L. (2009). Water entry of a wedge based on SPH model with an improved boundary treatment. *Journal of Hydrodynamics*, *21*(6), 750-757.

Gosman, A. D. (1999). Developments in CFD for industrial and environmental applications in wind engineering. *Journal of Wind Engineering and Industrial Aerodynamics*, *81*(1-3), 21-39.

Gotoh, H. (2001). Sub-particle-scale turbulence model for the MPS method-Lagrangian flow model for hydraulic engineering. *Computational Fluid Dynamics Jour*, *9*(4), 339-347.

Gotoh, H., & Khayyer, A. (2018). On the state-of-the-art of particle methods for coastal and ocean engineering. *Coastal Engineering Journal*, *60*(1), 79-103.

Hall, J. G., Eschenroeder, A. Q., & Marrone, P. V. (1962). Blunt-nose inviscid airflows with coupled nonequilibrium processes. *Journal of the Aerospace Sciences*, *29*(9), 1038-1051.

Harlow, F. H., & Welch, J. E. (1965). Numerical calculation of time-dependent viscous incompressible flow of fluid with free surface. *The physics of fluids*, *8*(12), 2182-2189.

Hibi, S. & Yabushita, K. (2004). A study on reduction of unusual pressure fluctuation of MPS method. *J Kansai Soc NA Jpn*, *241*, 125-131.

Hibiki, T., Lee, T. H., Lee, J. Y., & Ishii, M. (2006). Interfacial area concentration in boiling bubbly flow systems. *Chemical Engineering Science*, *61*(24), 7979-7990.

Higuera, P., Lara, J. L., & Losada, I. J. (2013). Realistic wave generation and active wave absorption for Navier–Stokes models: Application to OpenFOAM®. *Coastal Engineering*, *71*, 102-118.

Hirt, C. W., & Nichols, B. D. (1981). Volume of fluid (VOF) method for the dynamics of free boundaries. *Journal of computational physics*, *39*(1), 201-225.

Hockney, R. W., & Eastwood, J. W. (1988). *Computer simulation using particles*. crc Press.

Hoomans, B. P. B., Kuipers, J. A. M., Briels, W. J., & van Swaaij, W. P. M. (1996). Discrete particle simulation of bubble and slug formation in a two-dimensional gas-fluidised bed: a hard-sphere approach. *Chemical Engineering Science*, *51*(1), 99-118.

Hosseini, S. M., & Feng, J. J. (2011). Pressure boundary conditions for computing incompressible flows with SPH. *Journal of Computational physics, 230*(19), 7473-7487.

Ishii, M., & Hibiki, T. (2010). *Thermo-fluid dynamics of two-phase flow*. Springer Science & Business Media.

Ishii, M., & Mishima, K. (1984). Two-fluid model and hydrodynamic constitutive relations. *Nuclear Engineering and design*, *82*(2-3), 107-126.

James, S. C., Jones, C. A., Grace, M. D., & Roberts, J. D. (2010). Advances in sediment transport modelling. *Journal of Hydraulic Research*, *48*(6), 754–763.

Jha, S. K., & Bombardelli, F. A. (2009). Two-phase modeling of turbulence in dilute sediment-laden, open-channel flows. *Environmental fluid mechanics*, *9*(2), 237-266.

Ji, C., Munjiza, A., Avital, E., Ma, J., & Williams, J. J. R. (2013). Direct numerical simulation of sediment entrainment in turbulent channel flow. *Physics of Fluids*, *25*(5), 056601.

Khayyer, A., Gotoh, H., & Shao, S. (2009). Enhanced predictions of wave impact pressure by improved incompressible SPH methods. *Applied Ocean Research*, *31*(2), 111-131.

Khalitov, D. A., & Longmire, E. K. (2002). Simultaneous two-phase PIV by two-parameter phase discrimination. *Experiments in fluids*, *32*(2), 252-268.

Kiger, K. T., & Pan, C. (2000). PIV technique for the simultaneous measurement of dilute two-phase flows. *J. Fluids Eng.*, *122*(4), 811-818.

Koh, C. G., Gao, M., & Luo, C. (2012). A new particle method for simulation of incompressible free surface flow problems. *International journal for numerical methods in engineering*, *89*(12), 1582-1604.

Kopal, Z. (1947). *Tables of supersonic flow around cones* (No. 1). Mass. Inst. of Technology.

Koshizuka, S., & Oka, Y. (1996). Moving-particle semi-implicit method for fragmentation of incompressible fluid. *Nuclear science and engineering*, *123*(3), 421-434.

Kwon, J., & Monaghan, J. J. (2015). Sedimentation in homogeneous and inhomogeneous fluids using SPH. *International Journal of Multiphase Flow*, *72*, 155-164.

Lacaze, L., Phillips, J. C., & Kerswell, R. R. (2008). Planar collapse of a granular column: Experiments and discrete element simulations. *Physics of Fluids, 20*(6), 063302.

Laibe, G., & Price, D. J. (2014). Dusty gas with one fluid in smoothed particle hydrodynamics. *Monthly Notices of the Royal Astronomical Society*, *440*(3), 2147-2163.

Lancaster, P., & Salkauskas, K. (1981). Surfaces generated by moving least squares methods. *Mathematics of computation*, *37*(155), 141-158.

Lee, E. S., Moulinec, C., Xu, R., Violeau, D., Laurence, D., & Stansby, P. (2008). Comparisons of weakly compressible and truly incompressible algorithms for the SPH mesh free particle method. *Journal of computational Physics*, *227*(18), 8417-8436.

Leroy, A., Violeau, D., Ferrand, M., & Kassiotis, C. (2014). Unified semi-analytical wall boundary conditions applied to 2-D incompressible SPH. *Journal of Computational Physics, 261*, 106-129.

Li, C. W. (1997). Convection of particle thermals. *Journal of Hydraulic Research*, *35*(3), 363-376.

Li, J., Wen, L., Ge, W., Cui, H., & Ren, J. (1998). Dissipative structure in concurrent-up gas–solid flow. *Chemical Engineering Science*, *53*(19), 3367-3379.

Lin, H., & Atluri, S. N. (2000). Meshless local Petrov-Galerkin(MLPG) method for convection diffusion problems. *CMES(Computer Modelling in Engineering & Sciences)*, *1*(2), 45-60.

Lin, P., & Wang, D. (2006). Numerical modelling of 3D stratified free surface flows: A case study of sediment dumping. *International journal for numerical methods in fluids*, *50*(12), 1425-1444.

Lind, S. J., Rogers, B. D., & Stansby, P. K. (2020). Review of smoothed particle hydrodynamics: Towards converged Lagrangian flow modelling:

Smoothed Particle Hydrodynamics review. *Proceedings of the Royal Society A: Mathematical, Physical and Engineering Sciences*, *476*(2241).

Lind, S. J., Xu, R., Stansby, P. K., & Rogers, B. D. (2012). Incompressible smoothed particle hydrodynamics for free-surface flows: A generalised diffusion-based algorithm for stability and validations for impulsive flows and propagating waves. *Journal of Computational Physics*, *231*(4), 1499-1523.

Liu, D., & Zhu, F. (1988). Discussion on the basic equations for gas-particle flows in various models. *Frontiers of Fluid Mechanics*, 762-767. Pergamon.

Liu, G. R. (2002). *Mesh free methods: moving beyond the finite element method*. CRC press.

Liu, G. R., & Liu, M. B. (2003). *Smoothed particle hydrodynamics: a meshfree particle method*. World scientific.

Liu, M. B., & Liu, G. R. (2006). Restoring particle consistency in smoothed particle hydrodynamics. *Applied numerical mathematics*, *56*(1), 19-36.

Liu, M. B., & Liu, G. (2010). Smoothed particle hydrodynamics (SPH): an overview and recent developments. *Archives of computational methods in engineering*, *17*(1), 25-76.

Liu, M. B., Liu, G. R., & Lam, K. Y. (2003). A one-dimensional meshfree particle formulation for simulating shock waves. *Shock Waves*, *13*(3), 201-211.

Liu, M. B., Xie, W. P., & Liu, G. R. (2005). Modeling incompressible flows using a finite particle method. *Applied mathematical modelling*, *29*(12), 1252-1270.

Liu, M., Shao, J., & Chang, J. (2012). On the treatment of solid boundary in smoothed particle hydrodynamics. *Science China Technological Sciences*, *55*(1), 244-254.

Liu, W. K., Jun, S., & Zhang, Y. F. (1995). Reproducing kernel particle methods. *International journal for numerical methods in fluids*, *20*(8-9), 1081-1106.

Liu, X., Xu, H., Shao, S., & Lin, P. (2013). An improved incompressible SPH model for simulation of wave–structure interaction. *Computers & Fluids*, *71*, 113-123.

Liu, X., Lin, P., & Shao, S. (2014). An ISPH simulation of coupled structure interaction with free surface flows. *Journal of Fluids and Structures*, *48*, 46-61.

Lo, E. Y. M., & Shao, S. (2002). Simulation of near-shore solitary wave mechanics by an incompressible SPH method. *Applied Ocean Research*, *24*(5), 275–286.

Lucy, L. B. (1977). A numerical approach to the testing of the fission hypothesis. *The astronomical journal*, *82*, 1013-1024.

Luo, M., Khayyer, A., & Lin, P. (2021). Particle methods in ocean and coastal engineering. *Applied Ocean Research*, *114*, 102734.

Lyu, H. G., Sun, P. N., Huang, X. T., Zhong, S. Y., Peng, Y. X., Jiang, T., & Ji, C. N. (2022). A Review of SPH Techniques for Hydrodynamic Simulations of Ocean Energy Devices. *Energies*, *15*(2), 502.

Ma, Q. W. (2005a). Meshless local Petrov–Galerkin method for two-dimensional nonlinear water wave problems. *Journal of Computational Physics*, *205*(2), 611-625.

Ma, Q. W. (2005b). MLPG method based on Rankine source solution for simulating nonlinear water waves. *CMES: Computer Modelling in Engineering &Sciences*, *9*(2), 193-209.

Ma, Q. W. (2008). A new meshless interpolation scheme for MLPG_R method. *CMES - Computer Modeling in Engineering and Sciences*, *23*(2), 75–89.

Ma, Q. W., & Yan, S. (2006). Quasi ALE finite element method for nonlinear water waves. *Journal of computational physics*, *212*(1), 52-72.

Ma, Q., & Zhou, J. (2009). MLPG_R method for numerical simulation of 2D breaking waves. *CMES: Computer Modeling in Engineering & Sciences*, *43*(3), 277-304.

Ma, Q. W., Zhou, Y., & Yan, S. (2016). A review on approaches to solving Poisson's equation in projection-based meshless methods for modelling strongly nonlinear water waves. *Journal of Ocean Engineering and Marine Energy*, *2*(3), 279–299.

Ma, Z. H., Qian, L., Martinez-Ferrer, P. J., Causon, D. M., Mingham, C. G., & Bai, W. (2018). An overset mesh based multiphase flow solver for water entry problems. *Computers & Fluids*, *172*, 689-705.

McNamee, M. R. (2000). *An experimental study of axisymmetric turbulent puffs: their motion, dilution, and sedimentation* (Doctoral dissertation, Arizona State University).

Marrone, S., Bouscasse, B., Colagrossi, A., & Antuono, M. (2012). Study of ship wave breaking patterns using 3D parallel SPH simulations. *Computers & Fluids*, *69*, 54-66.

Mayrhofer, A., Ferrand, M., Kassiotis, C., Violeau, D., & Morel, F. X. (2015). Unified semi-analytical wall boundary conditions in SPH: analytical extension to 3-D. *Numerical Algorithms*, *68*(1), 15-34.

Meringolo, D. D., Colagrossi, A., Marrone, S., & Aristodemo, F. (2017). On the filtering of acoustic components in weakly-compressible SPH simulations. *Journal of Fluids and Structures*, *70*, 1-23.

Michalcová, V., & Kotrasová, K. (2020). The numerical diffusion effect on the cfd simulation accuracy of velocity and temperature field for the application of sustainable architecture methodology. *Sustainability*, *12*(23), 10173.

Monaghan, J. J. (1989). On the problem of penetration in particle methods. *Journal of Computational physics*, *82*(1), 1-15.

Monaghan, J. J. (1994). Simulating free surface flows with SPH. *Journal of computational physics*, *110*(2), 399-406.

Monaghan, J. J. (1997). Implicit SPH drag and dusty gas dynamics. *Journal of Computational Physics*, *138*(2), 801-820.

Monaghan, J. J., & Kajtar, J. B. (2009). SPH particle boundary forces for arbitrary boundaries. *Computer physics communications*, *180*(10), 1811-1820.

Monaghan, J. J., & Kocharyan, A. (1995). SPH simulation of multi-phase flow. *Computer Physics Communications*, *87*(1–2), 225–235.

Monaghan, J. J., & Lattanzio, J. C. (1985). A refined particle method for astrophysical problems. *Astronomy and astrophysics*, *149*, 135-143.

Monaghan, J. J., & Mériaux, C. A. (2018). An SPH study of driven turbulence near a free surface in a tank under gravity. *European Journal of Mechanics-B/Fluids*, *68*, 201-210.

Morikawa, D., Asai, M., Idris, N. A., Imoto, Y., & Isshiki, M. (2019). Improvements in highly viscous fluid simulation using a fully implicit SPH method. *Computational Particle Mechanics*, *6*(4), 529–544.

Morris, J. P. (1996). Analysis of smoothed particle hydrodynamics with applications. Australia: Monash University.

Morris, J. P., Fox, P. J., & Zhu, Y. (1997). Modeling low Reynolds number incompressible flows using SPH. *Journal of computational physics*, *136*(1), 214-226.

Nakasuji, K., Tamai, M. & Murota, A. (1990). Dynamic behaviour of sand clouds in water. In: Proceedings of the International conference on Physics: Modeling of Transport and Dispersion, Massachusetts Institute of Technology. Boston, United States

Nayroles, B., Touzot, G., & Villon, P. (1992). Generalizing the finite element method: diffuse approximation and diffuse elements. *Computational mechanics*, *10*(5), 307-318.

Neuman, S. P., & Witherspoon, P. A. (1970). Finite element method of analyzing steady seepage with a free surface. *Water Resources Research*, *6*(3), 889-897.

Nguyen, D. H., Levy, F., Van Bang, D. P., Guillou, S., Nguyen, K. D., & Chauchat, J. (2012). Simulation of dredged sediment releases into homogeneous water using a two-phase model. *Advances in Water Resources*, *48*, 102-112.

Noguchi, K., & Nezu, I. (2009). Particle–turbulence interaction and local particle concentration in sediment-laden open-channel flows. *Journal of Hydro-Environment Research, 3*(2), 54–68.

Oñate, E., Idelsohn, S., Zienkiewicz, O. C., & Taylor, R. (1996). A finite point method in computational mechanics. Applications to convective transport and fluid flow. *International journal for numerical methods in engineering*, *39*(22), 3839-3866.

O'Donoghue, T., & Ribberink, J. S. (2010). Measurements of sheet flow transport in acceleration-skewed oscillatory flow and comparison with practical formulations. *Coastal engineering*, *57*(3), 331-342.

Ouyang, J., & Li, J. (1999). Discrete simulations of heterogeneous structure and dynamic behavior in gas–solid fluidization. *Chemical Engineering Science*, *54*(22), 5427-5440.

Peng, Y. F., Shiau, Y. H., & Hwang, R. R. (2003). Transition in a 2-D lid-driven cavity flow. *Computers & Fluids*, *32*(3), 337-352.

Picouet, C., Hingray, B., & Olivry, J. C. (2001). Empirical and conceptual modelling of the suspended sediment dynamics in a large tropical African river: the Upper Niger river basin. *Journal of Hydrology*, *250*(1-4), 19-39.

Powell, R. L. (2008). Experimental techniques for multiphase flows. *Physics of Fluids*, *20*(4). https://doi.org/10.1063/1.2911023

Prosperetti, A., & Tryggvason, G. (2007). Introduction: A computational approach to multiphase flow. *Computational Methods for Multiphase Flow*, 1–18.

Qiang, H. F., Han, Y. W., Wang, K. P., & Gao, W. R. (2011). Numerical simulation of water filling process based on new method of penalty function SPH. *Engineering Mechanics*, *1*.

Quan, S., Lou, J., & Schmidt, D. P. (2009). Modeling merging and breakup in the moving mesh interface tracking method for multiphase flow simulations. *Journal of Computational Physics*, *228*(7), 2660-2675.

Rabczuk, T., Belytschko, T., & Xiao, S. (2004). Stable particle methods based on Lagrangian kernels. *Computer methods in applied mechanics and engineering*, *193*(12-14), 1035-1063.

Ran, Q., Tong, J., Shao, S., Fu, X., & Xu, Y. (2015). Incompressible SPH scour model for movable bed dam break flows. *Advances in Water Resources*, *82*, 39-50.

Ren, B. O., Li, C., Yan, X., Lin, M. C., Bonet, J., & Hu, S. M. (2014). Multiple-fluid SPH simulation using a mixture model. *ACM Transactions on Graphics*, *33*(5).

Richardson, J.F., & Zaki, W.N. (1954). *Trans. Inst. Chem. Eng. 32*, 35–53.

Rijas, A. S., Sriram, V., & Yan, S. (2019). Variable spaced particle in mesh-free method to handle wave-floating body interactions. *International Journal for Numerical Methods in Fluids*, *91*(6), 263-286.

Rogers, B. D., & Dalrymple, R. A. (2008). SPH modeling of tsunami waves. In *Advanced numerical models for simulating tsunami waves and runup* (pp. 75-100).

Rondon, L., Pouliquen, O., & Aussillous, P. (2011). Granular collapse in a fluid: Role of the initial volume fraction. *Physics of Fluids*, 23(7).

Schmeeckle, M. W., & Nelson, J. M. (2003). Direct numerical simulation of bedload transport using a local, dynamic boundary condition. *Sedimentology*, *50*(2), 279-301.

Schwaiger, H. F. (2008). An implicit corrected SPH formulation for thermal diffusion with linear free surface boundary conditions. *International journal for numerical methods in engineering*, *75*(6), 647-671.

Sellountos, E. J., & Polyzos, D. (2003). A MLPG (LBIE) method for solving frequency domain elastic problems. *Computer Modeling in Engineering and Sciences*, *4*(6), 619-636.

Shadloo, M. S., & Yildiz, M. (2011). Numerical modeling of Kelvin–Helmholtz instability using smoothed particle hydrodynamics. *International Journal for Numerical Methods in Engineering*, *87*(10), 988-1006.

Shadloo, M. S., Oger, G., & Le Touzé, D. (2016). Smoothed particle hydrodynamics method for fluid flows, towards industrial applications: Motivations, current state, and challenges. *Computers & Fluids*, *136*, 11-34.

Shakibaeinia, A., & Jin, Y. C. (2012). Lagrangian multiphase modeling of sand discharge into still water. *Advances in Water Resources*, *48*, 55-67.

Shao, S., & Lo, E. Y. (2003). Incompressible SPH method for simulating Newtonian and non-Newtonian flows with a free surface. *Advances in water resources*, *26*(7), 787-800.

Shi, H., & Yu, X. (2015). An effective Euler–Lagrange model for suspended sediment transport by open channel flows. *International Journal of Sediment Research*, *30*(4), 361-370.

Shi, H., Yu, X., & Dalrymple, R. A. (2017). Development of a two-phase SPH model for sediment laden flows. *Computer Physics Communications*, *221*, 259–272.

Shi, H., Si, P., Dong, P., & Yu, X. (2019). A two-phase SPH model for massive sediment motion in free surface flows. *Advances in Water Resources*, *129*(May), 80–98.

Sriram, V., & Ma, Q. W. (2010, June). Simulation of 2D breaking waves by using improved MLPG_R method. In *The Twentieth International Offshore and Polar Engineering Conference*. OnePetro.

Sriram, V., & Ma, Q. W. (2021). Review on the local weak form-based meshless method (MLPG): Developments and Applications in Ocean Engineering. *Applied Ocean Research*, *116*(July).

Stewart, H. B. (1979). Stability of two-phase flow calculation using two-fluid models. *Journal of Computational Physics*, *33*(2), 259-270.

Suchde, P. (2021). A meshfree Lagrangian method for flow on manifolds. *International Journal for Numerical Methods in Fluids*, *93*(6), 1871-1894.

Sun, P. N., Colagrossi, A., Marrone, S., & Zhang, A. M. (2017). The δplus-SPH model: Simple procedures for a further improvement of the SPH scheme. *Computer Methods in Applied Mechanics and Engineering*, *315*, 25-49.

Taha, T. R. (2005). An Introduction to Parallel Computational Fluid Dynamics. In *IEEE Concurrency* (Vol. 6, Issue 4).

Tran, T. T., & Kim, D. H. (2016). Fully coupled aero-hydrodynamic analysis of a semi-submersible FOWT using a dynamic fluid body interaction approach. *Renewable energy*, *92*, 244-261.

Tsuji, Y., Kawaguchi, T., & Tanaka, T. (1993). Discrete particle simulation of two-dimensional fluidized bed. *Powder technology*, *77*(1), 79-87.

Turowski, J. M., Rickenmann, D., & Dadson, S. J. (2010). The partitioning of the total sediment load of a river into suspended load and bedload: a review of empirical data. *Sedimentology*, *57*(4), 1126-1146.

Ulrich, C., Leonardi, M., & Rung, T. (2013). Multi-physics SPH simulation of complex marine-engineering hydrodynamic problems. *Ocean Engineering*, *64*, 109–121.

Vanoni, V. A. (1946). Transportation of suspended sediment by water. *Transactions of the American Society of Civil Engineers*, *111*(1), 67-102.

Vacondio, R., Altomare, C., De Leffe, M., Hu, X., Le Touzé, D., Lind, S., Marongiu, J. C., Marrone, S., Rogers, B. D., & Souto-Iglesias, A. (2021). Grand challenges for Smoothed Particle Hydrodynamics numerical schemes. *Computational Particle Mechanics*, *8*(3), 575–588.

Valizadeh, A., & Monaghan, J. J. (2015). A study of solid wall models for weakly compressible SPH. *Journal of Computational Physics, 300*, 5-19.

Van Rijn, L. C. (1984). Sediment transport, part I: bed load transport. *Journal of hydraulic engineering*, *110*(10), 1431-1456.

Vanoni, V. A. (1975). River dynamics. In *Advances in applied mechanics* (Vol. 15, pp. 1-87). Elsevier.

Violeau, D., & Rogers, B. D. (2016). Smoothed particle hydrodynamics (SPH) for free-surface flows: past, present and future. *Journal of Hydraulic Research*, *54*(1), 1-26.

Waddell, E. (1973). *Dynamics of Swash and Implication to Beach Response*. LOUISIANA STATE UNIV BATON ROUGE COASTAL STUDIES INST.

Wang, C., Wang, Y., Peng, C., & Meng, X. (2017). Two-fluid smoothed particle hydrodynamics simulation of submerged granular column collapse. *Mechanics Research Communications*, *79*, 15–23.

Wang, L., Khayyer, A., Gotoh, H., Jiang, Q., & Zhang, C. (2019). Enhancement of pressure calculation in projection-based particle methods by incorporation of background mesh scheme. *Applied Ocean Research*, *86*, 320-339.

Wang, Z. Bin, Chen, R., Wang, H., Liao, Q., Zhu, X., & Li, S. Z. (2016). An overview of smoothed particle hydrodynamics for simulating multiphase flow. *Applied Mathematical Modelling*, *40*(23–24), 9625–9655.

Xie, Z., & Stoesser, T. (2020). A three-dimensional Cartesian cut-cell/volume-of-fluid method for two-phase flows with moving bodies. *Journal of Computational Physics*, *416*, 109536.

Xiong, Q., Deng, L., Wang, W., & Ge, W. (2011). SPH method for two-fluid modeling of particle-fluid fluidization. *Chemical Engineering Science*, *66*(9), 1859–1865.

Xu, R., Stansby, P., & Laurence, D. (2009). Accuracy and stability in incompressible SPH (ISPH) based on the projection method and a new approach. *Journal of computational Physics*, *228*(18), 6703-6725.

Yadigaroglu, G., & Hetsroni, G. (2018). Nature of Multiphase Flows and Basic Concepts. In *Introduction to Multiphase Flow*.

Yan, S., & Ma, Q. W. (2010). QALE-FEM for modelling 3D overturning waves. *International Journal for Numerical Methods in Fluids*, *63*(6), 743-768.

Yan, S., Ma, Q. W., & Wang, J. (2020). Quadric SFDI for Laplacian Discretisation in Lagrangian Meshless Methods. *Journal of Marine Science and Application*, *19*(3), 362-380.

Yeganeh-Bakhtiary, A., Shabani, B., Gotoh, H., & Wang, S. S. Y. (2009). A three-dimensional Distinct Element model for bed-load transport. *Journal of Hydraulic Research*, *47*(2), 203–212.

Yeoh, G. H., & Tu, J. (2019). Introduction. *Computational Techniques for Multiphase Flows*, 1–18.

You, Y., Khayyer, A., Zheng, X., Gotoh, H., & Ma, Q. (2021). Enhancement of δ-SPH for ocean engineering applications through incorporation of a background mesh scheme. *Applied Ocean Research*, *110*, 102508.

Zhang, G. M., & Batra, R. (2004). Modified smoothed particle hydrodynamics method and its application to transient problems. *Computational mechanics*, *34*(2), 137-146.

Zhang, S., Morita, K., Fukuda, K., & Shirakawa, N. (2006). An improved MPS method for numerical simulations of convective heat transfer problems. *International journal for numerical methods in fluids*, *51*(1), 31-47.

Zheng, B. X., Sun, L., & Yu, P. (2021). A novel interface method for two-dimensional multiphase SPH: Interface detection and surface tension formulation. *Journal of Computational Physics*, *431*, 110119.

Zheng, X., Ma, Q. W., & Duan, W. Y. (2014). Incompressible SPH method based on Rankine source solution for violent water wave simulation. *Journal of Computational Physics*, *276*, 291-314.

Zienkiewicz, O. C., Taylor, R. L., Taylor, R. L., & Taylor, R. L. (2000). *The finite element method: solid mechanics* (Vol. 2). Butterworth-heinemann.

Zhou, Y., & Dong, P. (2018). A new implementation method of sharp interface boundary conditions for particle methods in simulating wave interaction with submerged porous structure. *Computers & Fluids*, *177*, 87-100.

Zhou, J. T., & Ma, Q. W. (2010). MLPG method based on rankine source solution for modelling 3D breaking waves. *Computer Modeling in Engineering and Sciences (CMES)*, *56*(2), 179.

Zhou, J. T., Ma, Q. W., & Yan, S. (2008). Numerical implementation of solid boundary conditions in meshless methods. *Proceedings of the International Offshore and Polar Engineering Conference*, *8*, 16–23.

Zhou, Y., Ma, Q. W., & Yan, S. (2017). MLPG_R method for modelling 2D flows of two immiscible fluids. *International Journal for Numerical Methods in Fluids*, *84*(7), 385-408.

Zubeldia, E. H., Fourtakas, G., Rogers, B. D., & Farias, M. M. (2018). Multi-phase SPH model for simulation of erosion and scouring by means of the shields and Drucker–Prager criteria. *Advances in Water Resources*, *117*(December 2017), 98–114.

Appendix A. MLPG_R formulation for wall particles

This appendix aims to provide a detailed formulation of the proposed boundary scheme for wall particles.

The PPE equation for solving the pressure of wall particles at the new time level is given by

$$\nabla^2 p^{n+1} = \frac{\rho}{\Delta t} \nabla \cdot \boldsymbol{u}^* \tag{1}$$

In order to find the solution for the pressure by solving Eq. (1), the MLPG_R method will be employed. A semicircle domain is specified as below for the two-dimensional case at each boundary particle on the rigid walls.

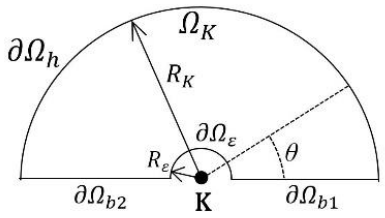

$$(S = \partial\Omega_K = \partial\Omega_h \cup \partial\Omega_{b1+b2} \cup \partial\Omega_\varepsilon)$$

Where $\partial\Omega_K$ is the boundary of the semicircle integration domain and $\partial\Omega_\varepsilon$ is a small surface surrounding the centre of Ω_K with a radius of R_ε. The reason for adding $\partial\Omega_\varepsilon$ is that the test function φ becomes infinite at $r = 0$ and so the Gauss's theorem cannot be used otherwise.

Eq. (1) is integrated over this domain after multiplying by a Rankine source test function φ for the two-dimensional case.

$$\int_{\Omega_K} \left(\nabla^2 p^{n+1} - \frac{\rho}{\Delta t} \nabla \cdot \boldsymbol{u}^* \right) \varphi \, d\Omega = 0 \tag{2}$$

$$\varphi = \frac{1}{2\pi} \ln \left(\frac{r}{R_K} \right) \tag{3}$$

where Ω_K is the area of the semicircle integration domain, *r* is the distance between a concerned point and the centre of the integration domain and R_K is the radius of the integration domain.

The test function φ is made to satisfy $\nabla^2 \varphi = 0$ in Ω_K and $\varphi = 0$ on its boundary $\partial\Omega_K$ in order to obtain a better form solution for solving the second-order derivative of pressure and the gradient of intermediate velocity by applying Gauss's theorem.

In Eq. (2), the order of unknown pressure can be reduced by adding a zero term $p\nabla^2\varphi$ and applying the Green's theorem, and the gradient of intermediate velocity can also be changed by employing the Gauss's theorem as below:

$$\int_{\Omega_K} [(\nabla^2 p)\varphi - p(\nabla^2 \varphi)] \, d\Omega = \int_{\Omega_K} (\nabla^2 p)\varphi \, d\Omega - \int_{\Omega_K} (\nabla^2 \varphi) p \, d\Omega \tag{4}$$

as

$$\int_{\Omega_K} (\nabla^2 p)\varphi \, d\Omega = \int_{\Omega_K} \nabla \cdot (\nabla p)\varphi \, d\Omega = \int_{\Omega_K} [\nabla \cdot (\varphi \nabla p) - \nabla p \cdot \nabla \varphi] \, d\Omega \qquad (4a)$$

$$\int_{\Omega_K} (\nabla^2 \varphi) p \, d\Omega = \int_{\Omega_K} \nabla \cdot (\nabla \varphi) p \, d\Omega = \int_{\Omega_K} [\nabla \cdot (p \nabla \varphi) - \nabla p \cdot \nabla \varphi] \, d\Omega \qquad (4b)$$

Eq. (4a) minus (4b) gives:

$$\int_{\Omega_K} (\nabla^2 p)\varphi \, d\Omega = \int_{\Omega_K} [\nabla \cdot (\varphi \nabla p) - \nabla \cdot (p \nabla \varphi)] \, d\Omega \qquad (5)$$

Employing 2D Gauss's theorem to Eqs. (5a) and (5b) yields:

$$\int_{\Omega_K} \nabla \cdot (\varphi \nabla p) \, d\Omega = \int_{\partial\Omega_K} \boldsymbol{n} \cdot (\varphi \nabla p) dS \qquad (5a)$$

$$\int_{\Omega_K} \nabla \cdot (p \nabla \varphi) \, d\Omega = \int_{\partial\Omega_k} \boldsymbol{n} \cdot (p \nabla \varphi) \, dS \qquad (5b)$$

and the first term at the right-hand side of Eq. (4) becomes

$$\int_{\Omega_K} (\nabla^2 p)\varphi \, d\Omega = \int_{\partial\Omega_K} [\boldsymbol{n} \cdot (\varphi \nabla p) - \boldsymbol{n} \cdot (p \nabla \varphi)] \, dS \qquad (6)$$

The first term on the right-hand side of Eq. (6) can be expanded to

$$\int_{\partial\Omega_h+\partial\Omega_\varepsilon+\partial\Omega_b}[\boldsymbol{n}\cdot(\varphi\nabla p)]\,dS=\int_{\partial\Omega_h}[\boldsymbol{n}\cdot(\varphi\nabla p)]\,dS+\int_{\partial\Omega_\varepsilon}\boldsymbol{n}\cdot(\varphi\nabla p)\,dS+\int_{\partial\Omega_b}\boldsymbol{n}\cdot(\varphi\nabla p)\,dS \tag{7}$$

as it can be easily proven that

$\int_{\partial\Omega_h}[\boldsymbol{n}\cdot(\varphi\nabla p)]\,dS=0$ as φ vanishes on $\partial\Omega_h$;

$\int_{\partial\Omega_\varepsilon}\boldsymbol{n}\cdot(\varphi\nabla p)\,dS=\int_{\pi}^{0}(\boldsymbol{n}\cdot\nabla p)\frac{1}{2\pi}\ln\left(\frac{R_\varepsilon}{R_K}\right)R_\varepsilon d\theta=0$ as $\lim_{R_\varepsilon\to 0}\ \ln\left(\frac{R_\varepsilon}{R_K}\right)R_\varepsilon\to 0.$

Manipulating Eq. (7) gives:

$$\int_{\partial\Omega_K}[\boldsymbol{n}\cdot(\varphi\nabla p)]\,dS=\int_{\partial\Omega_b}\boldsymbol{n}\cdot(\varphi\nabla p)\,dS \tag{8}$$

The second term on the left-hand side of Eq. (6) can be expanded to

$$\int_{\partial\Omega_h+\partial\Omega_\varepsilon+\partial\Omega_b}[\boldsymbol{n}\cdot(p\nabla\varphi)]\,dS=\int_{\partial\Omega_h}[\boldsymbol{n}\cdot(p\nabla\varphi)]\,dS+\int_{\partial\Omega_\varepsilon}[\boldsymbol{n}\cdot(p\nabla\varphi)]\,dS+\int_{\partial\Omega_b}[\boldsymbol{n}\cdot(p\nabla\varphi)]\,dS \tag{9}$$

as

$\int_{\partial\Omega_\varepsilon}[\boldsymbol{n}\cdot(p\nabla\varphi)] = \lim_{R_\varepsilon\to 0}\int_\pi^0 \frac{p}{2\pi R_\varepsilon}\cdot R_\varepsilon\, d\theta = \frac{p}{2\pi}\int_\pi^0 1\, d\theta = \frac{p}{2\pi}\times(0-\pi) = -\frac{p}{2}$;

(assuming p is constant in the infinitesimal area Ω_ε).

$\int_{\partial\Omega_b}[\boldsymbol{n}\cdot(p\nabla\varphi)]\, dS = 0$ as $\boldsymbol{n}$ is perpendicular to the solid wall $\partial\Omega_b$.

Manipulating Eq. (9) gives:

$$\int_{\partial\Omega_K}[\boldsymbol{n}\cdot(p\nabla\varphi)]\, dS = \int_{\partial\Omega_h}[\boldsymbol{n}\cdot(p\nabla\varphi)]\, dS - \frac{p}{2} \tag{10}$$

Finally, Eq. (8) minus Eq. (10) yields:

$$\int_{\Omega_K}(\nabla^2 p)\varphi\, d\Omega = \int_{\partial\Omega_b}\boldsymbol{n}\cdot(\varphi\nabla p)\, dS - \int_{\partial\Omega_h}[\boldsymbol{n}\cdot(p\nabla\varphi)]\, dS + \frac{p}{2} \tag{11}$$

Multiplying the second term of Eq. (2) associated with the intermediate velocity gives:

$$\int_{\Omega_K}\frac{\rho}{\Delta t}\varphi(\nabla\cdot\boldsymbol{u}^*)\, d\Omega = \int_{\Omega_K}\frac{\rho}{\Delta t}\nabla\cdot(\varphi\boldsymbol{u}^*)d\Omega - \int_{\Omega_K}\frac{\rho}{\Delta t}\boldsymbol{u}^*\cdot\nabla\varphi\, d\Omega \tag{12}$$

as $\varphi(\nabla\cdot\boldsymbol{u}^*) + \boldsymbol{u}^*\cdot\nabla\varphi = \nabla\cdot(\varphi\boldsymbol{u}^*)$

Then, Gauss's theorem is also employed in the first term of Eq. (12) and further expand this term gives:

$$\int_{\partial\Omega_h+\partial\Omega_\varepsilon+\partial\Omega_b}\left[\frac{\rho}{\Delta t}\boldsymbol{n}\cdot(\varphi\boldsymbol{u}^*)dS\right]=\int_{\partial\Omega_h}\frac{\rho}{\Delta t}\boldsymbol{n}\cdot(\varphi\boldsymbol{u}^*)dS+\int_{\partial\Omega_\varepsilon}\frac{\rho}{\Delta t}\boldsymbol{n}\cdot(\varphi\boldsymbol{u}^*)dS+\int_{\partial\Omega_b}\frac{\rho}{\Delta t}\boldsymbol{n}\cdot(\varphi\boldsymbol{u}^*)dS \quad (13)$$

as

$\int_{\partial\Omega_h}\frac{\rho}{\Delta t}\boldsymbol{n}\cdot(\varphi\boldsymbol{u}^*)dS=0$ as φ vanishes on $\partial\Omega_h$;

$\int_{\partial\Omega_\varepsilon}\frac{\rho}{\Delta t}\boldsymbol{n}\cdot(\varphi\boldsymbol{u}^*)dS=0$ as $\int_{\partial\Omega_\varepsilon}\varphi dS=\lim_{R_\varepsilon\to 0}\int_\pi^0\frac{1}{2\pi}\ln\left(\frac{R_\varepsilon}{R_K}\right)R_\varepsilon\,d\theta\to 0$.

Eq. (12) becomes

$$\int_{\Omega_K}\frac{\rho}{\Delta t}\varphi(\nabla\cdot\boldsymbol{u}^*)\,d\Omega=\int_{\partial\Omega_b}\frac{\rho}{\Delta t}\boldsymbol{n}\cdot(\varphi\boldsymbol{u}^*)dS-\int_{\Omega_K}\frac{\rho}{\Delta t}\boldsymbol{u}^*\cdot\nabla\varphi\,d\Omega \quad (14)$$

Combining Eq. (11) and (14), Eq. (2) has been manipulated to Eq. (15), which remains two terms need to be integrated over the wall boundary, $\partial\Omega_b$.

$$\int_{\partial\Omega_b}\boldsymbol{n}\cdot(\varphi\nabla p)\,dS-\int_{\partial\Omega_h}[\boldsymbol{n}\cdot(p\nabla\varphi)]\,dS+\frac{p}{2}=\int_{\partial\Omega_b}\frac{\rho}{\Delta t}\boldsymbol{n}\cdot(\varphi\boldsymbol{u}^*)dS-\int_{\Omega_K}\frac{\rho}{\Delta t}\boldsymbol{u}^*\cdot\nabla\varphi\,d\Omega \quad (15)$$

Next, imposing the impermeable boundary conditions, i.e., Eqs. (16) to Eq. (17) in order to avoid the computation of second-order derivatives.

$$\boldsymbol{u} \cdot \boldsymbol{n} = \boldsymbol{U} \cdot \boldsymbol{n} \tag{16}$$

$$\boldsymbol{u}^{n+1} = \boldsymbol{u}^{*} + \left(-\frac{1}{\rho}\nabla p^{n+1}\right)\Delta t \tag{17}$$

Here, Eq. (16) and Eq. (17) are combined to formulate an alternative solid boundary condition (Zhou et al., 2008), as shown in Eq. (18).

$$\boldsymbol{n} \cdot \nabla p = \frac{\rho}{\Delta t}\boldsymbol{n} \cdot (\boldsymbol{u}^{*} - \boldsymbol{U}) \tag{18}$$

The general weak formulation for wall boundary particle is obtained as shown in Eq. (19)

$$\int_{\partial\Omega_h} [\boldsymbol{n} \cdot (p\nabla\varphi)]\, dS - \frac{p}{2} = \int_{\Omega_K} \frac{\rho}{\Delta t}\boldsymbol{u}^{*} \cdot \nabla\varphi \, d\Omega + \int_{\partial\Omega_b} \frac{\rho}{\Delta t}\boldsymbol{n} \cdot (\varphi \boldsymbol{U}) dS \tag{19}$$

If the wall boundary is fixed, as $\boldsymbol{n} \cdot \boldsymbol{U} = 0$, and so Eq. (19) can be further simplified as Eq. (20)

$$\int_{\partial\Omega_h} [\boldsymbol{n} \cdot (p\nabla\varphi)]\, dS - \frac{p}{2} = \int_{\Omega_K} \frac{\rho}{\Delta t}\boldsymbol{u}^{*} \cdot \nabla\varphi \, d\Omega \tag{20}$$

Appendix B. Governing equations for two-phase flows

The primary purpose of this appendix is to provide the detailed derivation process of two-phase governing equations from the Eulerian form to the Lagrangian form.

Continuity equations:

The continuity equations in Eulerian form is shown below:

$$\frac{\partial \alpha_f \rho_f}{\partial t} + \frac{\partial \alpha_f \rho_f u_{f,j}}{\partial x_j} = 0 \tag{1}$$

$$\frac{\partial \alpha_s \rho_s}{\partial t} + \frac{\partial \alpha_s \rho_s u_{s,j}}{\partial x_j} = 0 \tag{2}$$

where α is the volume fraction of different phases and $\alpha_f + \alpha_s = 1$; ρ is the density; u is the velocity component; t is the time; x is the coordinate; the subscripts of f and s represent the fluid phase and the sediment phase, respectively; following the summation convention, the indices i or j represent the coordinate directions for two-dimensional cases.

$$\frac{\partial \alpha_f \rho_f}{\partial t} + \frac{\partial \alpha_f \rho_f u_{f,j}}{\partial x_j} = \rho_f \frac{\partial \alpha_f}{\partial t} + u_{f,j} \frac{\partial \alpha_f}{\partial x_j} + \alpha_f \frac{\partial u_{f,j}}{\partial x_j} = 0 \tag{3}$$

as $\frac{\partial \rho_f}{\partial t} = 0$ by employing the incompressible condition.

Substituting substantial derivative $\frac{d\varphi}{dt} = \frac{\partial \varphi}{\partial t} + u_{f,j}\frac{\partial \varphi}{\partial x_j}$, Eq. (3) yields:

$$\frac{d\alpha_f}{dt} + \alpha_f \frac{\partial u_{f,j}}{\partial x_j} = 0 \tag{4}$$

Similarly,

$$\frac{\partial \alpha_s \rho_s}{\partial t} + \frac{\partial \alpha_s \rho_s u_{s,j}}{\partial x_j} = \frac{\partial \alpha_s}{\partial t} + u_{f,j}\frac{\partial \alpha_s}{\partial x_j} - u_{f,j}\frac{\partial \alpha_s}{\partial x_j} + \frac{\partial \alpha_s u_{s,j}}{\partial x_j} = 0 \tag{5}$$

By adding the zero term $u_{f,j}\frac{\partial \alpha_s}{\partial x_j} - u_{f,j}\frac{\partial \alpha_s}{\partial x_j} = 0$, thus Eq. (2) becomes:

$$\frac{d\alpha_s}{dt} - u_{f,j}\frac{\partial \alpha_s}{\partial x_j} + \frac{\partial \alpha_s u_{s,j}}{\partial x_j} = 0 \tag{6}$$

As employing the substantial derivative: $\frac{d\alpha_s}{dt} = \frac{\partial \alpha_s}{\partial t} + u_{f,j}\frac{\partial \alpha_s}{\partial x_j}$, Eq.(6) can be further manipulated as shown below:

$$\frac{d\alpha_s}{dt} - \left(\frac{\partial \alpha_s u_{f,j}}{\partial x_j} - \alpha_s \frac{\partial u_{f,j}}{\partial x_j}\right) + \frac{\partial \alpha_s u_{s,j}}{\partial x_j} = 0 \tag{7}$$

Finally, the continuity equation for the sediment phase Eq. (2) becomes:

$$\frac{d\alpha_s}{dt} = -\alpha_s \frac{\partial u_{f,j}}{\partial x_j} - \frac{\partial\left[\alpha_s\left(u_{s,j} - u_{f,j}\right)\right]}{\partial x_j} \tag{8}$$

Eqs. (4) and (8) represent the continuity equations in Lagrangian form.

Momentum equations:

The momentum equations are presented in Eulerian form as

$$\frac{\partial \alpha_f \rho_f u_{f,i}}{\partial t} + \frac{\partial \alpha_f \rho_f u_{f,i} u_{f,j}}{\partial x_j} = -\alpha_f \frac{\partial p}{\partial x_i} + \frac{\partial \alpha_f \rho_f T_{f,ij}}{\partial x_j} + \alpha_f \rho_f g_i - F_i \tag{9}$$

$$\frac{\partial \alpha_s \rho_s u_{s,i}}{\partial t} + \frac{\partial \alpha_s \rho_s u_{s,i} u_{s,j}}{\partial x_j} = -\alpha_s \frac{\partial p}{\partial x_i} + \frac{\partial \alpha_s \rho_s T_{s,ij}}{\partial x_j} + \alpha_s \rho_s g_i + F_i \tag{10}$$

where p is the pressure; g is the acceleration of gravity; T is the stress tensor, and F is the interphase force.

The left hand side of Eq. (9) can be expanded as

$$\frac{\partial \alpha_f \rho_f u_{f,i}}{\partial t} + \frac{\partial \alpha_f \rho_f u_{f,i} u_{f,j}}{\partial x_j}$$
$$= \alpha_f \rho_f \frac{\partial u_{f,i}}{\partial t} + u_{f,i} \frac{\partial \alpha_f \rho_f}{\partial t} + u_{f,i} \frac{\partial \alpha_f \rho_f u_{f,j}}{\partial x_j} + \alpha_f \rho_f u_{f,j} \frac{\partial u_{f,i}}{\partial x_j} \quad (11)$$

Substituting Eq. (1) and the substantial derivative $\frac{du_{f,i}}{dt} = \frac{\partial u_{f,i}}{\partial t} + u_{f,j} \frac{\partial u_{f,i}}{\partial x_j}$ yields:

$$\frac{\partial \alpha_f \rho_f u_{f,i}}{\partial t} + \frac{\partial \alpha_f \rho_f u_{f,i} u_{f,j}}{\partial x_j} = \alpha_f \rho_f \frac{du_{f,i}}{dt} \quad (12)$$

So, the momentum equation for the fluid phase in Lagrangian form becomes:

$$\frac{du_{f,i}}{dt} = -\frac{1}{\rho_f} \frac{\partial p}{\partial x_i} + \frac{1}{\alpha_f \rho_f} \frac{\partial \alpha_f \rho_f T_{f,ij}}{\partial x_j} + g_i - \frac{F_i}{\alpha_f \rho_f} \quad (13)$$

Similarly, the left hand side of Eq. (10) can be manipulated as

$$\frac{\partial \alpha_s \rho_s u_{s,i}}{\partial t} + \frac{\partial \alpha_s \rho_s u_{s,i} u_{s,j}}{\partial x_j}$$
$$= \alpha_s \rho_s \frac{\partial u_{s,i}}{\partial t} + u_{s,i} \frac{\partial \alpha_s \rho_s}{\partial t} + u_{s,i} \frac{\partial \alpha_s \rho_s u_{s,j}}{\partial x_j} + \alpha_s \rho_s u_{s,j} \frac{\partial u_{s,i}}{\partial x_j} \quad (14)$$

Substituting Eq. (2) and the substantial derivative $\frac{du_{s,i}}{dt} = \frac{\partial u_{s,i}}{\partial t} + u_{f,j}\frac{\partial u_{s,i}}{\partial x_j}$ yields:

$$\frac{\partial \alpha_s \rho_s u_{s,i}}{\partial t} + \frac{\partial \alpha_s \rho_s u_{s,i} u_{s,j}}{\partial x_j} = \alpha_s \rho_s \left(\frac{du_{s,i}}{dt}\right) - \alpha_s \rho_s \left(u_{f,j}\frac{\partial u_{s,i}}{\partial x_j} - u_{s,j}\frac{\partial u_{s,i}}{\partial x_j}\right) \quad (16)$$

Finally, Eq. (10) becomes:

$$\frac{du_{s,i}}{dt} = -\left(u_{s,j} - u_{f,j}\right)\frac{\partial u_{s,i}}{\partial x_j} - \frac{1}{\rho_s}\frac{\partial p}{\partial x_i} + \frac{1}{\alpha_s \rho_s}\frac{\partial \alpha_s \rho_s T_{s,ij}}{\partial x_j} + g_i + \frac{F_i}{\alpha_s \rho_s} \quad (17)$$

Finally, the governing equations in the Lagrangian form are tabulated below:

Fluid phase:

$$\frac{d\alpha_f}{dt} + \alpha_f \frac{\partial u_{f,j}}{\partial x_j} = 0$$

$$\frac{du_{f,i}}{dt} = -\frac{1}{\rho_f}\frac{\partial p}{\partial x_i} + \frac{1}{\alpha_f \rho_f}\frac{\partial \alpha_f \rho_f T_{f,ij}}{\partial x_j} + g_i - \frac{F_i}{\alpha_f \rho_f}$$

Sediment phase:

$$\frac{d\alpha_s}{dt} = -\alpha_s \frac{\partial u_{f,j}}{\partial x_j} - \frac{\partial\left[\alpha_s\left(u_{s,j} - u_{f,j}\right)\right]}{\partial x_j}$$

$$\frac{du_{s,i}}{dt} = -\left(u_{s,j} - u_{f,j}\right)\frac{\partial u_{s,i}}{\partial x_j} - \frac{1}{\rho_s}\frac{\partial p}{\partial x_i} + \frac{1}{\alpha_s \rho_s}\frac{\partial \alpha_s \rho_s T_{s,ij}}{\partial x_j} + g_i + \frac{F_i}{\alpha_s \rho_s}$$